Light Unbound Nuclear Systems beyond the Dripline

Dissertation
zur Erlangung des Doktorgrades
der Naturwissenschaften

vorgelegt beim Fachbereich Physik
der Johann Wolfgang Goethe-Universität
in Frankfurt am Main

von
Yuliya Aksyutina
aus Kharinovo (Russland)

Frankfurt am Main 2009
(D30)

vom Fachbereich Physik der
Johann Wolfgang Goethe-Universität als Dissertation angenommen.

Dekan:	Prof. Dr. D.-H. Rischke
Gutachter:	Prof. Dr. J. Stroth Dr. R. Reifarth
Datum der Disputation:	14 August 2009

Abstract

Starting from the first observation of the halo phenomenon 20 years ago, more and more neutron-rich light nuclei were observed. The study of unstable nuclear systems beyond the dripline is a relatively new branch of nuclear physics. In the present work, the results of an experiment at GSI (Darmstadt) with relativistic beams of the halo nuclei ^{8}He, ^{11}Li and ^{14}Be with energies of 240, 280 and 305 MeV/nucleon, respectively, impinging on a liquid hydrogen target are discussed. Neutron/proton knockout reactions lead to the formation of unbound systems, followed by their immediate decay. The experimental setup, consisting of the neutron detector LAND, the dipole spectrometer ALADIN and different types of tracking detectors, allows the reconstruction of the momentum vectors of all reaction products measured in coincidence. The properties of unbound nuclei are investigated by reconstructing the relative-energy spectra as well as by studying the angular correlations between the reaction products. The observed systems are ^{9}He, ^{10}He, ^{10}Li, ^{12}Li and ^{13}Li.

The isotopes ^{12}Li and ^{13}Li are observed for the first time. They are produced in the ^{1}H(^{14}Be, 2pn)^{12}Li and ^{1}H(^{14}Be, 2p)^{13}Li knockout reactions. The obtained relative-energy spectrum of ^{12}Li is described as a single virtual s-state with a scattering length of $a_s = -13.7(1.6)$ fm. The spectrum of ^{13}Li is interpreted as a resonance at an energy of $E_r = 1.47(13)$ MeV and a width of $\Gamma \approx 2$ MeV superimposed on a broad correlated background distribution.

The isotope ^{10}Li is observed after one-neutron knockout from the halo nucleus ^{11}Li. The obtained relative-energy spectrum is described by a low-lying virtual s-state with a scattering length $a_s = -22.4(4.8)$ fm and a p-wave resonance with $E_r = 0.566(14)$ MeV and $\Gamma = 0.548(30)$ MeV, in agreement with previous experiments.

The observation of the nucleus ^{8}He in coincidence with one or two neutrons, as a result of proton knockout from ^{11}Li, allows to reconstruct the relative-energy spectra for the heavy helium isotopes, ^{9}He and ^{10}He. The low-energy part of the ^{9}He spectrum is described by a virtual s-state with a scattering length $a_s = -3.16(78)$ fm. In addition, two resonance states with $l \neq 0$ at energies of 1.33(8) and 2.4 MeV are observed.

For the ^{10}He spectrum, two interpretations are possible. It can be interpreted as a superposition of a narrow resonance at 1.42(10) MeV and a broad correlated background distribution. Alternatively, the spectrum is being well described by two resonances at energies of 1.54(11) and 3.99(26) MeV.

Additionally, three-body energy and angular correlations in ^{10}He and ^{13}Li nuclei at the region of the ground state ($0 < E_{Cnn} < 3$ MeV) are studied, providing information about structure of these unbound nuclear systems.

Contents

1. Introduction

1.1 Nuclear landscape

Nuclear physics is the science of atomic nuclei, their properties, the interactions between them and their constituents. Different nuclei are basically different combinations of particles of two types: protons and neutrons. However, even now, decades after most of the basic properties of stable nuclei have been discovered, a fundamental theory of the nuclear structure is still lacking, and theoretical predictions of the limits of nuclear stability are unreliable. The task of finding these limits falls back onto the experimentalists. The vast area of interest, available for nuclear physicists nowadays, includes about 2900 different nuclei [1] and is depicted in the nuclear chart shown in Fig. 1.1. Among all varieties of

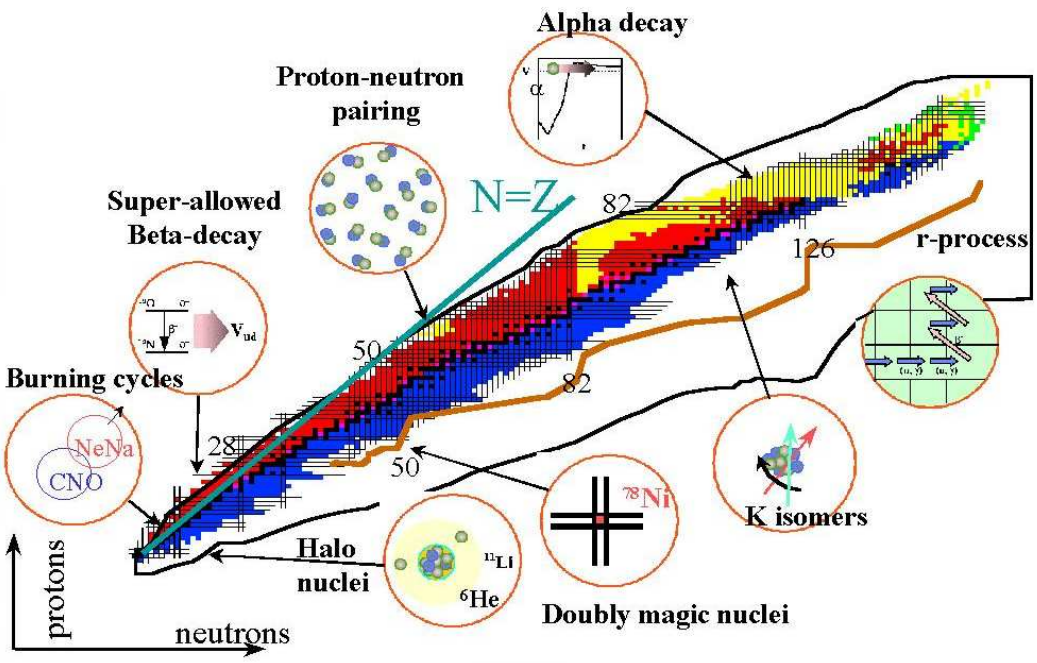

Figure 1.1: Nuclear landscape. Stable nuclei are marked as black squares, red and blue squares denote β^+- and β^--radioactive nuclei, respectively. Nuclei unstable against α-particle decay or undergo spontaneous fission are marked in yellow.

nuclei, only a limited amount exists naturally. They are marked as black squares (see Fig. 1.1) and commonly called the valley of β stability. Nuclei to the left of the valley contain excess number of protons and are unstable against β^+-decay

or electron capture. Neutron-rich nuclei, to the right of the valley, are unstable against β^--decay. The heaviest stable isotope is ^{209}Bi and all heavier nuclides decay mainly by α-particle emission or even spontaneous fission.

What happens at the limits of stability? Substantial changes in the neutron-to-proton ratio to both sides of the valley of β stability lead to a decrease of the binding energy for the last nucleon(s) until it traverses the zero value ($B_{n,p} = 0$) at the so-called driplines. The neutron and proton driplines are defined by the heaviest particle-stable nuclides within a family of isotopes and isotones, respectively. Figure 1.1 shows as well the highlights of the experimental activities along the driplines. Study of different phenomena can shed light on different aspects of nuclear interaction.

While light N = Z nuclides are mostly stable, the heavier ones lie away from the line of β stability. Disappearance of shell-model magic numbers and appearance of new magic numbers occurs close to the dripline. An example is the nucleus ^{56}Ni with 28 protons and 28 neutrons, which is not doubly magic according to the experimental observations [2]. In the case of ^{100}Sn, the deficit of neutrons with respect to the mean mass of the stable tin isotopes is about 18 and it is expected [3] to be the heaviest N = Z nucleus stable against the ground-state proton decay. This stability is related to the doubly-magic character of ^{100}Sn.

A study of neutron-proton pairing, which is especially strong in nuclei around N = Z and contributes to the binding energy, provides important information about the interaction between these two particles [4]. Evidence exists that exotic neutron-rich nuclei as well gain binding energy from an unpaired proton, which narrows the gaps between shells and provides the opportunity to bind even more neutrons. This feature results in the significant difference between the heaviest oxygen (^{24}O) and fluorine (^{31}F) isotopes [5]. However, the observation of such strange behavior is still novel and requires further investigations, since in stable nuclei the attractive pairing interaction generally enhances the stability of isotopes with even numbers of protons and neutrons.

Precise measurements [6] of the ft-values for super-allowed 0^+ to 0^+ Fermi nuclear beta decay, which takes place in nuclei in the N = Z region, provide the most accurate value for the up-down quark-mixing matrix element, V_{ud}, of the Cabibbo-Kobayashi-Maskawa matrix. This matrix should be unitary, and the experimental verification of that expectation constitutes an important test of the Standard Model.

The low-energy dipole strength located close to the particle-emission threshold is a general feature [7] in many isospin asymmetric nuclei. This mode was named Pygmy Dipole Resonance (PDR) and, in neutron-rich nuclei, has been explained as being generated by oscillations of weakly bound neutrons with respect to the isospin symmetric core [8]. Thus, in exotic nuclei with extreme neutron excess the PDR modes should be especially pronounced. The picture of collective flow as seen in experiments is a precise test of the existing models including self-consistent microscopic calculations with the collective degrees of freedom. The origin of approximately one half of the nuclides heavier than iron observed in nature is explained by the r-process. The existence of pygmy resonances have important implications on theoretical predictions of radiative neutron capture rates in the r-process nucleosynthesis, and consequently on the calculated abundance distribution in the universe. This was studied using calculations and fits to the properties for neutron-rich nuclei involved in this process [9]. The inclusion of the PDR increases r-abundances distributions for nuclei around A = 130 by about two orders of magnitude (see Fig. 6 in [9]), compared to the case in which only the GDR was taken into account.

In the mass region A = 180 high angular momentum yrast states in deformed nuclei can sometimes be populated by aligning the spins of few nucleons [10]. The states with high total spin projection on the nuclear symmetry axis, K, may be long-lived, with half-lives ranging from a few nanoseconds to several years. The K-isomer states exhibit an unusually simple shell configuration, providing a powerful probe of structure and residual interactions in nuclear many-body systems [11]. They also give information on multi-nucleon correlations in the nuclear surface.

In this thesis, special attention is paid to the light nuclei extremely enriched by neutrons and especially to the nuclei at and beyond the dripline.

1.2 Halo nuclei

The exact location of the driplines at the neutron-rich side is known only for light nuclei. Near the neutron dripline, the large neutron excess and small neutron separation energy can lead to dramatic changes in nuclear structure. One of the most interesting discoveries is the appearance of a so-called neutron halo. The proton dripline is relatively well established for most of the elements because the

Coulomb repulsion among protons has a strong destabilizing effect on nuclei with significantly fewer neutrons than protons. On the other hand, the neutron binding energy little by little approaches zero as the neutron number increases. Elusive quantum-mechanical effects such as nucleon pairing and energy-level bunching determine the stability of the heaviest isotope of each element.

First experimental evidence for the unusual properties of ^{11}Li was obtained 20 years ago by I. Tanihata and co-workers at Berkeley [12], when the interaction cross section was measured for this nucleus at relativistic energy. The root mean square (RMS) radius for its matter distribution, deduced from the cross section, turned out to be extremely large [13]. Measurements of the quadrupole deformation for ^{9}Li and ^{11}Li have shown that these nuclei have nearly the same deformation [14]. The term "neutron halo" was introduced by P.G. Hansen and B. Jonson in Ref. [15], where the large radius of ^{11}Li was connected with its small neutron binding energy which finally results in the extended and diluted distribution of neutrons around the ^{9}Li core. This was confirmed by measurements of charge radii [16–18]. Experimental data on matter and charge radii for helium and lithium isotopes are compared in Fig. 1.2. The comparison demonstrates that for heaviest isotopes the matter radii are about 0.5 fm larger then the charge radii.

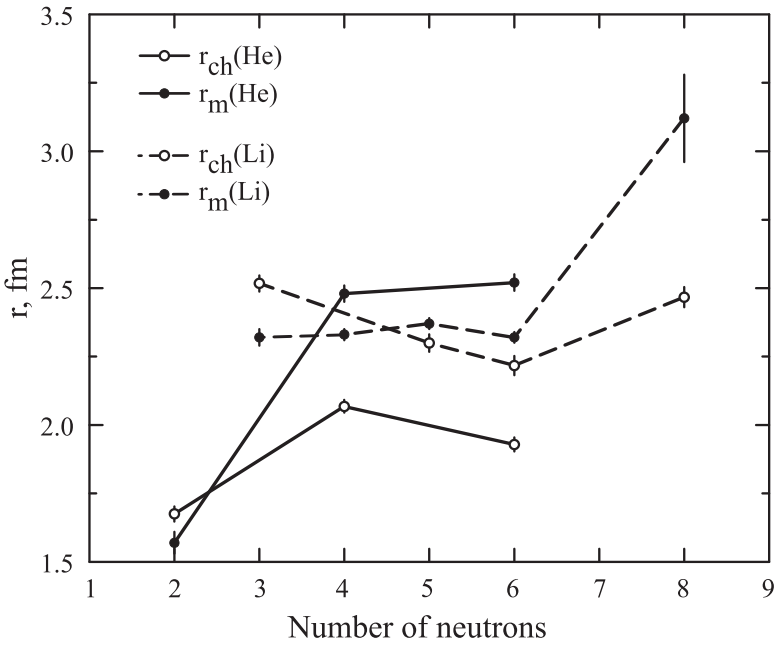

Figure 1.2: Charge (open circles) and matter (filled circles) radii of helium and lithium isotopes are shown by solid and dashed lines, respectively [13, 16–18].

Nuclei with two-neutron halo represent a group with so-called Borromean properties. The term was introduced by M. Zhukov *et al.* [19] for the bound three-body systems where any of the two-body subsystems is unbound. This is connected to the fact, that particle stability and binding energies at the neutron dripline depend on the neutron pairing, as one can see from Fig. 1.3. The helium isotopes ^{6}He and ^{8}He are particle-stable, while their "neighbors", ^{5}He and ^{7}He, are unbound.

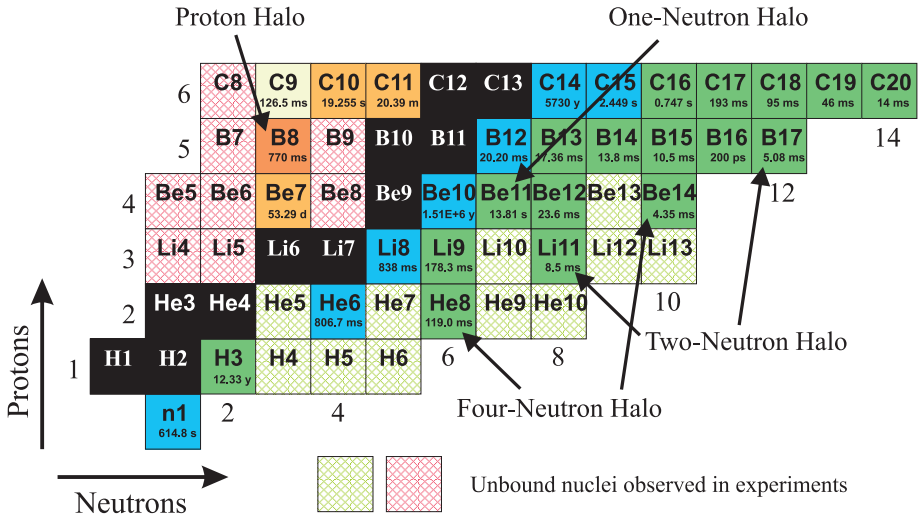

Figure 1.3: Low-Z part of nuclear chart. Stable isotopes are marked as black squares.

Since the phenomenon has been discovered, more halo nuclei have been observed: one-neutron halo nuclei, such as ^{11}Be and ^{19}C, and two-neutron halo nuclei, such as ^{6}He and ^{17}B. One of the most interesting examples is ^{8}He, which can be viewed both, as a two-neutron halo with a ^{6}He core, or as a four-neutron halo with an α-particle core. The Coulomb barrier is an obstacle for halo formation at the proton-rich side. However, even there, a halo state was observed in ^{8}B and presumably exists in ^{17}Ne [20, 21].

1.3 Nuclear systems beyond the dripline

Currently, the neutron dripline is experimentally accessible up to element Mg [22]. However, even the dripline is not a limit for researchers. By knocking out nucleons, or even heavier constituents from the halo nucleus, it is possible to produce configurations which are particle unstable, but still can be observed as resonances.

For Borromean nuclei with a neutron halo, the knockout of a valence neutron is a process with high probability. The remaining subsystem of the core with only one neutron is unbound. It is also possible to study proton knockout from the core. The halo nucleus already contains too many neutrons and, thus, one-proton removal leads to the formation of an even more exotic system. The investigation of such resonances is similar to the discrete-level spectroscopy of stable nuclei and plays an essential role in exploring the single-particle and collective structures of weakly bound nuclei in the dripline region. The problem of identifying states and measuring energies in unbound systems is not only a difficult exercise in nuclear spectroscopy. Experimental measurements of binding energies of nuclear states serve as a benchmark for different theoretical models.

One of the most interesting and intriguing results in the field is the observation of the heavy hydrogen isotope ^{5}H. The measurement of two protons emitted in the decay of ^{2}He from the reaction ^{1}H(^{6}He, pp)^{5}H with 36 MeV/nucleon beam of ^{6}He, resulted in a peak at an energy of 1.7(3) MeV with the width $\Gamma = 1.9(4)$ MeV above the t + n + n threshold [23]. The following experiments reported about the observation of a very narrow resonance with $\Gamma < 0.5$ MeV at an energy of $E_r = 1.8$ MeV in reactions ^{3}H(t, p)^{5}H [24], ^{3}H(t, p)^{5}H and ^{2}H(^{6}He, ^{3}He)^{5}H [25]. Several measurements failed to observe the narrow resonance in the t + n + n system [26–28]. In the most recent experiment high statistics was collected and correlations between the decay products of ^{5}H were investigated [29]. The $1/2^{+}$ ground state was observed at an energy of 1.8 MeV with a width $\Gamma \approx 1.3$ MeV. However, the situation is still unclear, and more investigations are needed.

Experiments studying exotic systems are difficult to perform and analyze. Only at high beam energies, several hundreds of MeV/nucleon, it is possible to suddenly remove one of components from a nucleus without disturbing the rest. At the same time, it is necessary to achieve energy resolution below a few hundreds of keV in order to perform spectroscopy. The interpretation of the obtained spectra is also a challenging task. Only the combination of results from several experiments, using different approaches leads to a consistent description that can be adopted with confidence.

1.4 Experimental studies along the dripline

Halo nuclei are typically short-lived and cannot be used as a target material. Therefore, experiments are performed in inverse kinematics, where a beam of exotic nuclei hits a stable target. Radioactive-beam facilities provide a direct access to experimental studies of nuclei at and beyond the dripline. All experiments with exotic nuclei can be divided into two main groups: low-energy beam (up to 20 MeV/nucleon) and high-energy beam (energy range from 100 MeV/nucleon to 1 GeV/nucleon) experiments.

Low-energy beams primarily allow the study of transfer and fusion reactions as well as reactions via the formation of compound nuclei. Reactions proceed via a compound nucleus, if a low energy projectile is absorbed by the target and the energy is redistributed between all nucleons. On a time scale of about 10^{-19} seconds, the energy happens to be concentrated in one particle, e.g. a neutron, which allows it to evaporate. Charged particles are rarely evaporated because of the Coulomb barrier. The condition for the formation of the compound nucleus is that the incident particle free path in the nuclear matter λ should be much shorter then the nuclear radius R. This condition can be fulfilled if $E \ll AS$, where E is the energy of the projectile particle, A the number of nucleons and S the neutron separation energy [30].

If, for some reasons, the energy is redistributed between several nucleons only, without involving the rest of the nucleus, the reaction occurs without formation of a compound nucleus, and this process is called direct reaction. It usually takes place if a projectile of intermediate or high energy is involved. The examples of direct reactions are inelastic scattering, when energy is transferred to the target nucleus, and transfer reactions, when nucleons are redistributed between target and projectile nuclei. The use of high-energy beams of exotic nuclei has many advantages, both from experimental and theoretical points of view. High beam energies result in short interaction times and small scattering angles, which allow the use of simplifying approximations for the description of the reaction mechanism. From the experimental side, large beam velocities lead to a strong kinematical focusing, which allows for measurements covering the full solid angle with moderately sized detectors with high efficiency.

There are basically two methods to produce beams of exotic nuclei [31]: the use of an Isotope Separator On-Line (ISOL) and In-Flight Separation (IFS).

In the former case an accelerated beam of stable nuclei bombards a target, and radioactive atoms of interest are produced through nuclear reactions. These atoms are transported, by various techniques, including thermal diffusion, to an ion source where they are ionized and extracted. The radioactive ions are then mass-separated from other ions and accelerated to energies needed for nuclear physics experiments by a second accelerator. The ISOL technique can produce high beam qualities, purities and intensities. The disadvantage is that beams with very short half-lives (less than 10 ms) are difficult to produce. Pioneered at CERN, this technique is presently very extensively used e.g. at Jyväskylä (Finland), Louvain-la-Neuve (Belgium), Orsay (France), Warsaw (Poland), Oak Ridge (USA), TRIUMF (Canada), CIAE Beijing (China).

The second method, IFS, is implemented in such facilities as FRS (GSI, Germany), A1200 (MSU, USA), BigRIPS (RIKEN, Japan) and SISSI (GANIL, France), COMBAS and ACCULINNA (JINR Dubna, Russia), RIBLL (Lanzhou, China) and SBL (Chiba, Japan). After acceleration of heavy-ion beam to high energy (40 - 2000 MeV/nucleon) it is directed to a thick production target for converting into secondary beams via nuclear fragmentation. Reaction products are separated by means of a magnetic field. An advantage of this method is that the lifetime of the studied nuclei is only limited by the flight path and the beam velocity. This allows to study nuclei with lifetimes in the microseconds region.

Halo nuclei have been studied at GSI for many years [32], using carbon and lead targets. The carbon target allows to study nuclear break-up, because of its small charge. In the case of a lead target, the electromagnetic dissociation process dominates. The use of a hydrogen target, as in this work, opens new interesting possibilities to study quasi-free scattering with beams of unstable nuclei [33].

This thesis is divided into eight chapters. A general description of the experimental setup is following this introduction. A more detailed explanation of detectors and calibration procedures is presented in chapter three. The fourth chapter is dedicated to the description of the observed quantities and their role in the analysis of the experiment. The response of the setup is shortly presented in chapter five. Neutron knockout is described in chapter six, while chapter number seven contains results for the proton knockout channels, including relative-energy spectroscopy and studies of angular and energy correlations. The thesis is concluded with a summary and outlook.

2. Experimental technique

2.1 Production of exotic nuclei

The experiment, described in this thesis, was performed at the Gesellschaft für Schwerionenforschung (GSI) in Darmstadt. A schematical view of the heavy-ion beam facility is shown in Fig. 2.1. The primary beam of ^{18}O from the ion

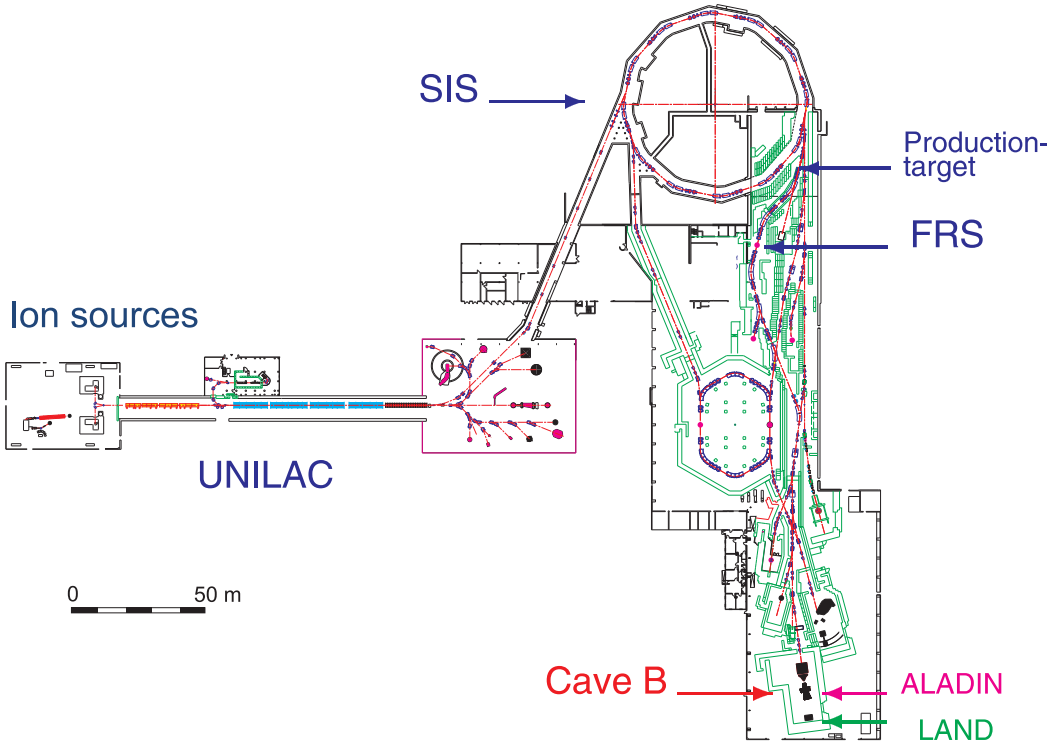

Figure 2.1: Heavy-ion beam facility at GSI (Darmstadt). The SIS can provide beams of elements from hydrogen to uranium, with energies up to 2 GeV/nucleon. After the acceleration in the SIS, the beam is directed to the thick production target. Products of nuclear fragmentation are separated by means of magnetic field in FRS and directed to Cave B.

source was preaccelerated in the UNIversal Linear Accelerator (UNILAC) and injected into the heavy-ion synchrotron (SchwerIonenSynchrotron, SIS). After the acceleration it was extracted and directed to a beryllium production target with the thickness of 4.007 g/cm^2 for converting it into secondary beams via nuclear fragmentation. Reaction products were separated by means of the $B\rho - \Delta E - B\rho$

method in the FRagment Separator (FRS), which is described in detail in Ref. [34]. The production rate of the needed isotopes was low, therefore a degrader (ΔE) was not used, and the secondary beam was left as a mixture of different nuclei with similar A/Z ratio. A particle with velocity v, mass A and charge q is passing through the magnet, if the following condition is satisfied:

$$B\rho = \frac{p}{q} \propto \beta\gamma\frac{A}{q}, \tag{2.1}$$

where $\beta = v/c$ and $\gamma = 1/\sqrt{1-\beta^2}$. The magnetic rigidity $B\rho$ was set to be 9.52 Tm during the whole experiment and different beam compositions were achieved by varying the energy of the primary beam. During the first stage of the experiment, the primary beam with an energy of 308 MeV/nucleon was used. As a result, the secondary beam contained mainly ^{8}He ($A/Z = 4$) nuclei. Increasing the primary beam energy up to 360.5 MeV/nucleon caused the selection of ^{14}Be ($A/Z = 3.5$) beam. In both cases, ^{11}Li with $A/Z = 3.6$ passed through the separator. Weak admixtures of ^{6}He and ^{3}H were also present. The energies of the ^{8}He, ^{11}Li and ^{14}Be ions were 240, 280 and 305 MeV/nucleon, respectively. The beam parameters are summarized in Table 2.1. The beam intensity was high enough to

Table 2.1: Properties of the secondary beam. There were two different settings during the experiment. First, "helium" setting, led to domination of ^{8}He ions in the beam. During the second part of the experiment, "beryllium" setting was applied, where ^{14}Be and ^{11}Li had maximum intensities.

Ion	^{8}He	^{11}Li	^{14}Be
$B\rho$		9.52 Tm	
E, MeV/nucleon	240	280	305
Intensity, s^{-1}	350	50	40

get reasonable statistics during the two weeks of experiment, and low enough to analyze the data collected on the event-by-event basis.

After separation the secondary beam was transported to the experimental hall (Cave B), where the reaction target was situated. The scheme of the experimental setup in Cave B is shown in Fig. 2.2. It allows for kinematically complete measurements of all reaction products.

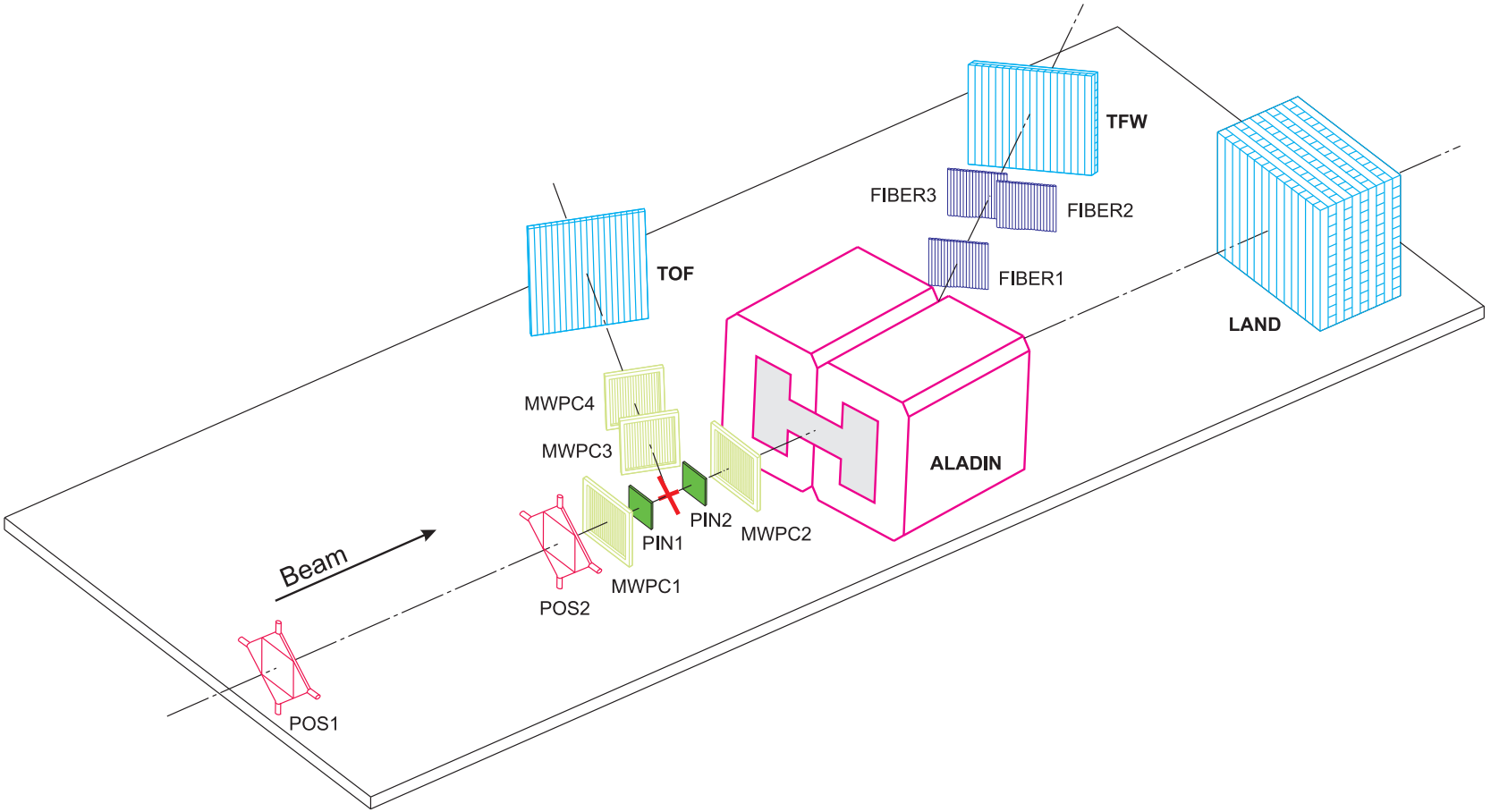

Figure 2.2: Scheme of the experimental setup. Due to strong beam focusing, it allows for kinematically complete measurements of all reaction products with detectors covering only a small fraction of the laboratory solid angle. POS – POsition Sensitive scintillator, PIN –p-i-n diode, MWPC – Multi-Wire Proportional Chamber, ALADIN – A LArge gap DIpole magNet, LAND – Large Area Neutron Detector, TFW – Time of Flight Wall, TOF – Time Of Flight wall (see text for details).

2.2 Identification of incoming particles

The position sensitive scintillator detectors POS1 and POS2 were installed at the entrance of the cave and before the target (see Fig. 2.2). As suggested by the name, POS detectors are supposed to measure the position of the passing particles. However, in the mean time detectors with better position resolution are used. Here, POS detectors are mainly used for the measurement of the incoming beam velocity. Each of them consists of a thin scintillator foil with a thickness of 300 μm, being viewed through light guides by four photomultipliers (up, down, left and right). The mean value of the time signals from these photomultipliers is taken as the time when a particle hits the detector. Just before and after the target, p-i-n silicon diodes (PIN1 and PIN2) were situated, which were used for energy-loss measurements. From the energy loss in the silicon diodes, the charges of incoming and outgoing particles are deduced. The time of flight between the two POS detectors allows for an A/Z determination, using Eq. 2.1 and taking into account that all incoming particles have the same $B\rho$. An example of a two-dimensional identification plot is shown in Fig. 2.3. This method allows for a very clean and reliable identification of the incoming particles. The ions of interest are chosen for further analysis using two-dimensional cuts.

2.3 Target and beam tracking in the target region

A liquid-hydrogen target with a thickness of 350 mg/cm^2 was used in the experiment. The liquid-hydrogen was filled into a 5 cm long, 2.8 cm diameter cylinder with 50 μm mylar windows. Measurements in a so-called empty-target mode, when the target volume was filled with gaseous hydrogen, were also performed in order to control the background from reactions occurring outside the target volume, e.g. in detector materials, separation foils, air etc.

Eventwise tracking of particles is necessary, since the size of the beam spot at the target was about 3 cm in diameter. In the present experiment, tracking is performed by means of Multi-Wire Proportional Chambers (MWPC), which are described in Ref. [35]. Relying on the fact that there were more than 11 meters distance from the last magnet to the target position such that only particles with small incoming angle can reach the target, the incoming beam was assumed to be parallel with high accuracy. Thus, only one chamber, MWPC1, was used

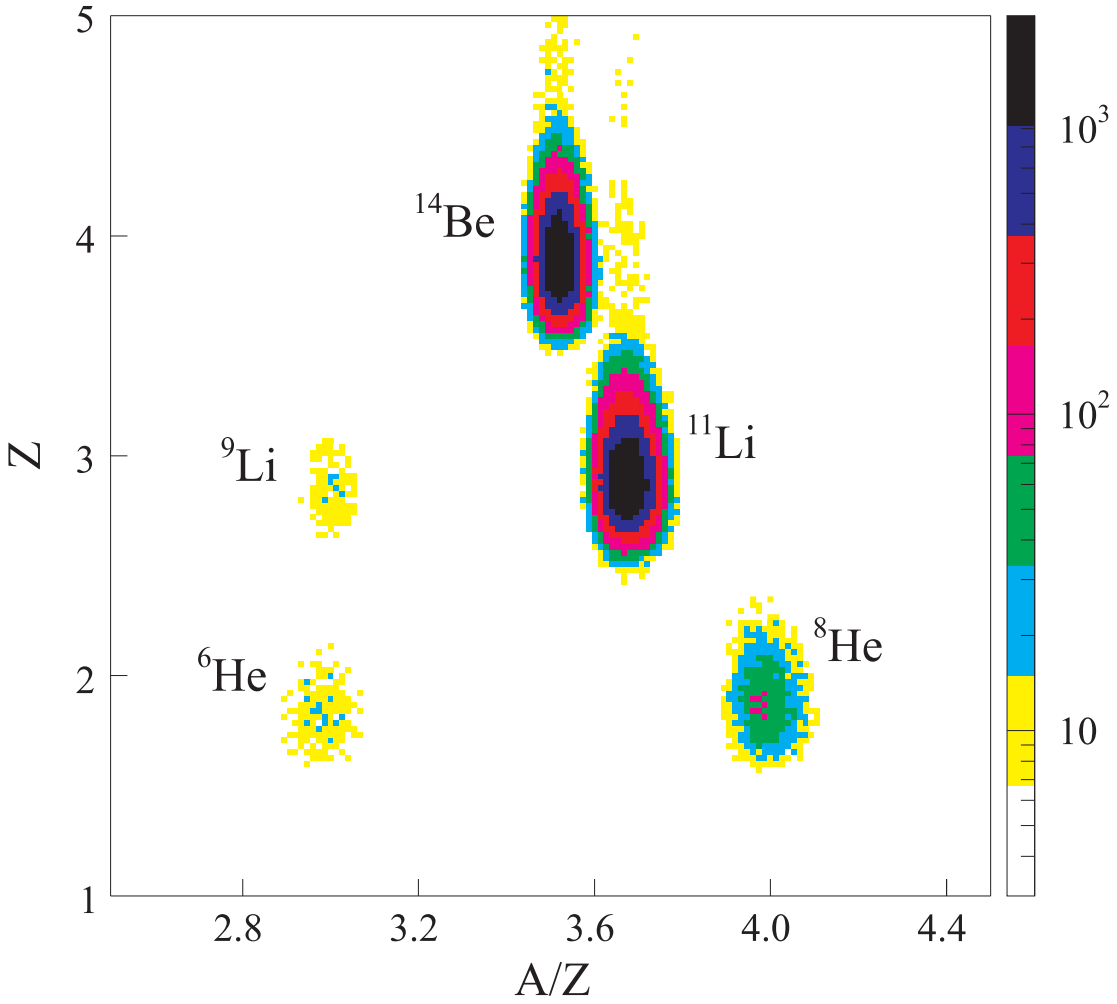

Figure 2.3: The secondary beam is an admixture of different ions, therefore each particle has to be identified. The charge of the ion was obtained from its energy loss in the PIN1 diode and the A/Z ratio was calculated using time of flight between two POS detectors for the known $B\rho$. The isotopes ^{8}He, ^{11}Li and ^{14}Be are clearly separated.

for the tracking of incoming particles, being installed 90 cm upstream of the target. Figure 2.4 shows the tracking of beam particles before and after the target. The position of the reaction vertex along the beam direction z is unknown. In the present analysis, it is fixed at the central plane of the target, marked as a gray circle. The angles θ and ϕ are defined using the MWPC2 detector, which was situated at a distance of 65.7 cm downstream of the target. The angular resolutions for different nuclei are listed in Table 2.2. The resolution is dominated by the uncertainty of the position of the reaction vertex and the uncertainty in the angle of the incoming particles.

The data analysis revealed, that the beam is broader than the target size.

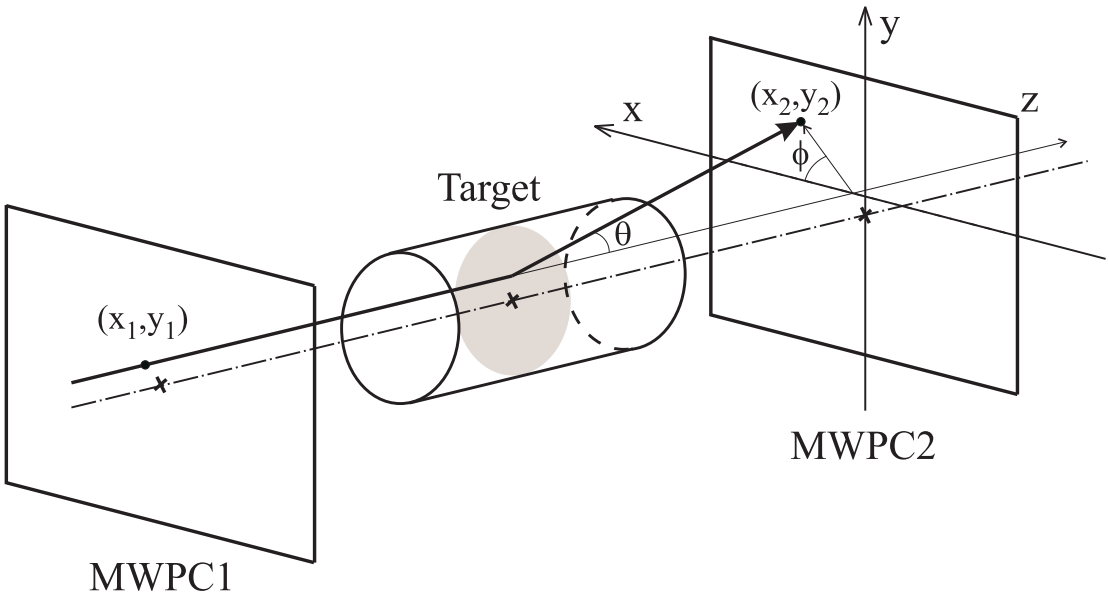

Figure 2.4: Tracking of the beam particles before and after the target. The grey area indicates the central plane of the target, where reactions are assumed to happen.

Table 2.2: Angular resolution of the experimental setup for different ions. Angular spread in the horizontal and vertical directions are denoted by σ_{θ_x} and σ_{θ_y}, respectively.

	^{8}He	^{11}Li	^{14}Be
σ_{θ_x}, mrad	4.29	3.93	4.74
σ_{θ_y}, mrad	3.83	3.8	3.8

The left panel of Fig. 2.5 shows the position distribution of the incoming beam in MWPC1 detector. In order to select particles, hitting the target, a special condition is applied. The scattering of beam particles between the two detectors MWPC1 and MWPC2 in an empty-target run has been studied. Since the target volume is empty, the angular spread of the beam can increase only if the particles hit the target frame. The investigation of the angular spread between the two chambers as a function of the position in MWPC1 revealed, that the target is shifted relative to the detector and its center corresponds to MWPC1 coordinates (-0.2 cm, 0.2 cm). Therefore, only particles, hitting MWPC1 in a circle centered at (-0.2 cm, 0.2 cm) within a radius of 1.2 cm, as shown in the right frame of Fig. 2.5, are accepted for further analysis. The radius of 1.2 cm is chosen in order to avoid edge effects.

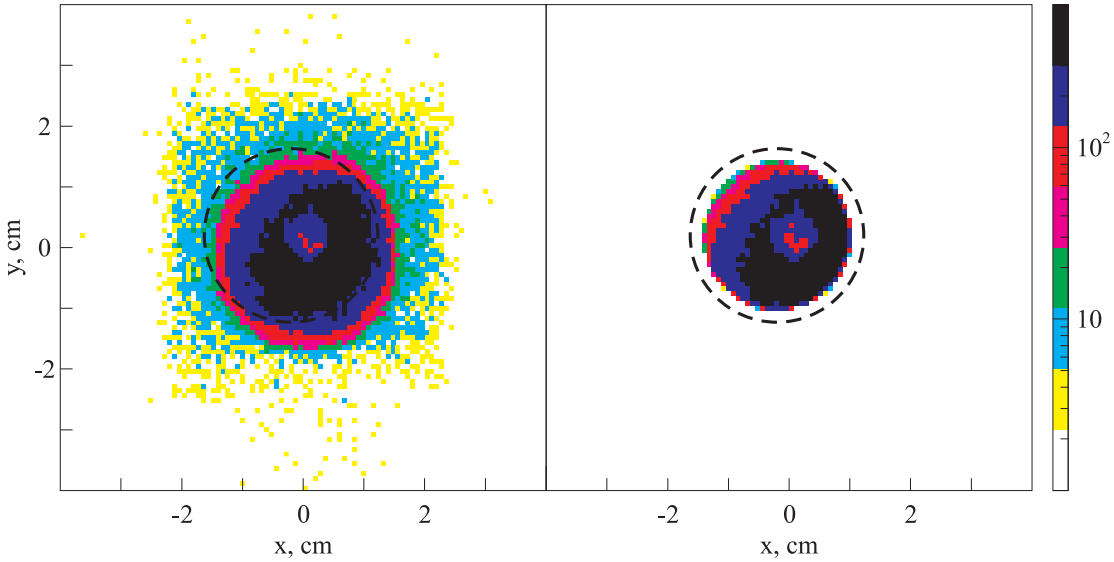

Figure 2.5: Position of the incoming beam in the MWPC1 detector before (left panel) and after (right panel) the condition for hitting the target has been applied. The target boundary is shown as dashed line.

2.4 Detection of charged reaction products

The charges of the reaction products are determined using the PIN2 detector, placed at a distance of 46 cm after the target. The velocity of the fragments is measured with a Time-of-Flight Wall (TFW), installed 754 cm after the target. This detector consists of 32 scintillator modules (paddles). The modules are arranged in two layers. The first layer is made of 18 vertically oriented paddles, and the remaining 14 paddles are placed horizontally, forming a second layer. The vertical paddles are 147 cm long, the horizontal 189 cm. All of them have a thickness of 0.5 cm and a width of 10 cm. The detector measures also the energy loss of the particles. An example of the energy-loss spectrum obtained in the TFW is shown in the left panel of Fig. 2.6.

Different isotopes are deflected to different angles by A LArge gap DIpole magNet (ALADIN), described in Ref. [36]. The TFW is used for the measurement of x and y positions of charged fragments, which in combination with the angles $\{\theta, \phi\}$, measured by MWPC2 allows to define the deflection angle θ' through the ALADIN magnet. An example of isotope separation is shown in the right panel of Fig. 2.6. The lithium isotopes, emerging from reactions with ^{14}Be ions, are clearly identified.

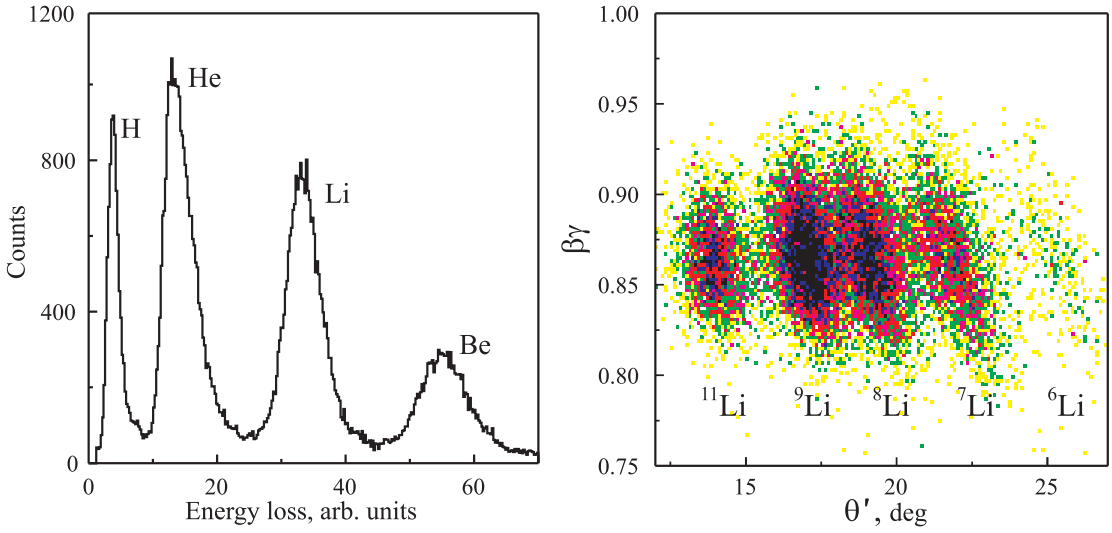

Figure 2.6: Charge of the fragments is determined by energy loss in PIN2 and TFW detectors. Example of energy-loss spectrum obtained using TFW is shown in the left panel. Different isotopes are separated by means of different deflection angles in the ALADIN magnet. The separation of lithium isotopes originating from ^{14}Be is shown in the right panel.

2.5 The Large Area Neutron Detector

Neutrons are not deflected by the magnetic field of ALADIN and continue to move straight ahead towards the Large Area Neutron Detector (LAND), situated 1124 cm after the target. A photo of LAND is shown in Fig. 2.7. The detector is subdivided into 200 paddles of 200 × 10 cm^2 area and 10 cm depth [37]. A single paddle is shown schematically in Fig. 2.8. In order to reduce the mean free path of the neutrons in the detector, passive iron converters are introduced. Thus, each paddle consists of 11 sheets of iron (the two outer ones are 2.5 mm thick, the others are 5 mm thick) and 10 sheets of 5 mm thick scintillator, mounted in an iron box which has a wall thickness of 1 mm. The detector is composed of 10 layers. Each layer consists of 20 paddles, consecutive layers are oriented perpendicular to each other, giving a position in both vertical and horizontal directions, using both the position of the paddle and the location of the hit within the paddle. The detection efficiency for neutrons with energies of 240 - 300 MeV is about 85%.

The mechanism of the neutron detection in LAND is based on hadronic showers, developing preferably in the passive iron converters. The shower may consist of several charged particles, producing light in the scintillator. It is prob-

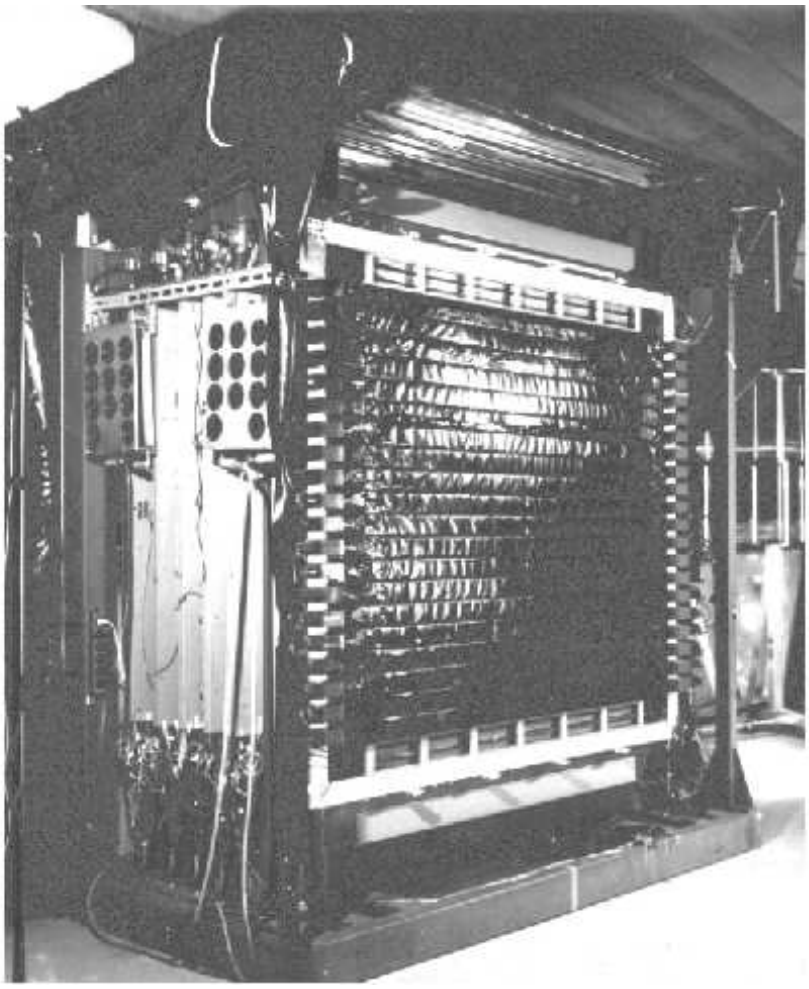

Figure 2.7: A photo of the Large Area Neutron Detector. The detector covers an area of 2×2 m^2 and allows for detection of high-energetic neutrons with an efficiency of about 85%.

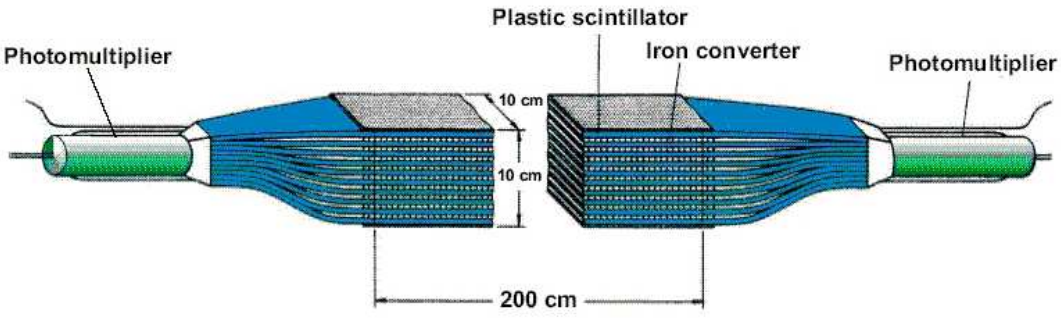

Figure 2.8: Schematic view of a LAND paddle. Each paddle has a size of $200\times10\times10$ cm^3 and consists of 10 layers of plastic scintillator and 11 layers of iron, arranged into a "sandwich" structure.

able that the visible light is produced in more than one paddle, thus, resulting in multiple hits inside the detector. Since the neutrons are scattering, this may be in non-neighboring paddles far apart. On average, 1.4 paddles fire per incident neutron with an energy of 240 - 300 MeV [37]. Thus, per event there are several hits in LAND. A special algorithm is then used to reconstruct the number of incident neutrons. The routine provides the capability to resolve several neutrons crossing LAND. All hits are sorted in time. The hit, which is the first in time, carries information about momentum of the first incident neutron. Hits, satisfying the kinematical conditions for scattering or backscattering events from the first hit, are assigned to the same neutron interaction chain, otherwise they are discarded. The remaining hits are again sorted in time and the first is subsequently considered to be the first hit of the second neutron. All first hits within the interaction chains are used to determine the momenta of the initial neutrons and are used to calculate the momentum of the second neutron. The procedure is repeated until all hits are assigned. If hits of two or more neutrons are spatially close, it can be complicated to distinguish them, if they are not well separated in time.

2.6 Detection of recoil protons

The plastic scintillator wall (TOF) consisting of 20 plastic scintillator submodules (200 cm length, 10 cm width, 1 cm thickness) was placed at the left side of the target at a distance of 392 cm. It was used for the detection of recoiling target protons. A metalized plastic foil bag filled with helium gas was installed between the target and TOF detector in order to reduce multiple scattering of the protons. Two chambers, MWPC3 and MWPC4, were installed between the target and the helium container and were used for proton tracking, in order to determine the reaction vertex. Protons can be separated from background events by a two-dimensional plot showing energy loss in the proton wall versus the time of flight between the target and the proton wall. An example is shown in Fig. 2.9. The two values reveal a λ-shaped punch-through pattern for the protons. Low-energy particles are completely stopped in the detector and deposit an energy of $\Delta E = E_p$, therefore being inversely proportional to time of flight squared. Protons, arriving the detector with an energy higher than 32.7 MeV are not stopped anymore, and their energy loss relates as $\Delta E \sim 1/E_p$. Using the ATIMA code [38] for calculation of time of flight of the particle through the matter, it is possible

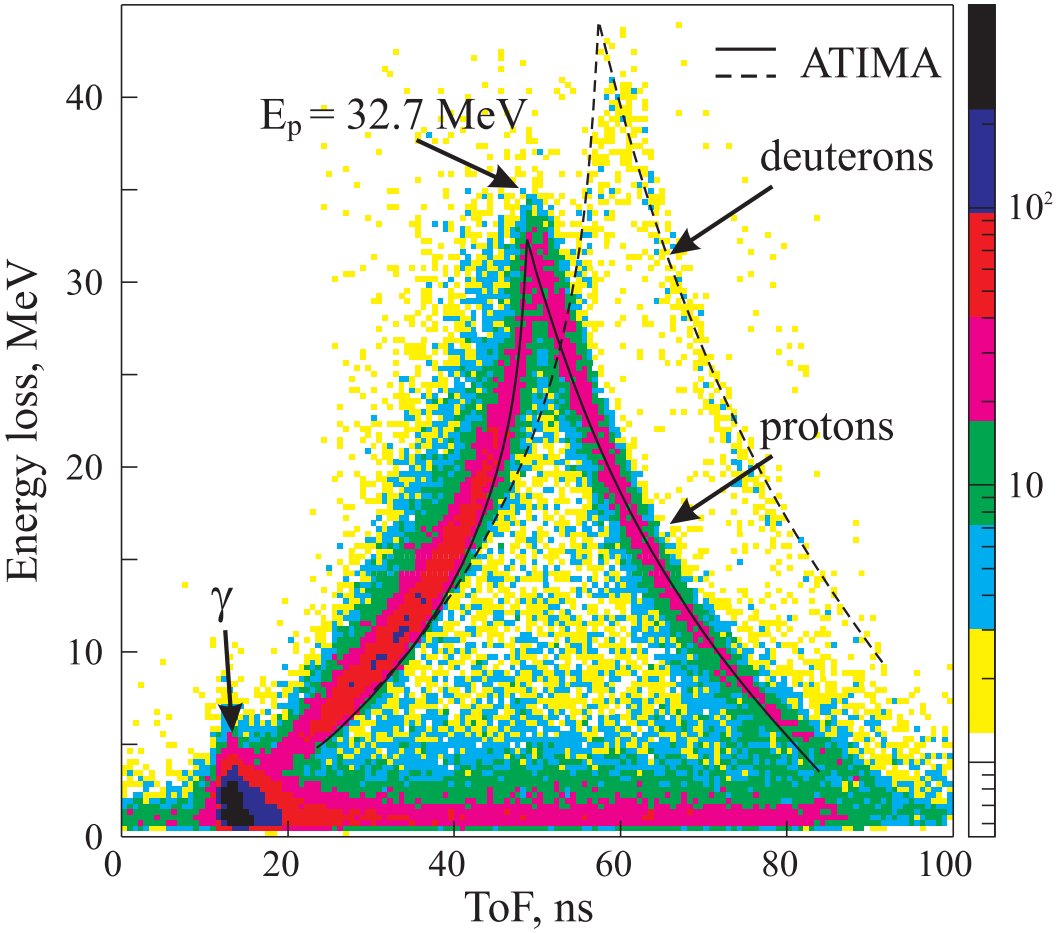

Figure 2.9: Correlations between protons time of flight and energy loss in the proton wall. Low-energy protons were completely stopped in the detector. Protons, arriving the TOF with energies of 32.7 MeV and higher, penetrate through 1 cm of plastic.

to reconstruct the initial energy of protons from energy loss and time of flight measured by the detector.

Trace amounts of deuterons and tritons are also identified. The observed amount of these isotopes is higher than one would expect stemming from the natural liquid hydrogen. Most probably they are the products of break-up reactions. This can be a subject of further investigations. One can also see a γ-peak with a long tail. Since most of the gammas are produced in the target region, they have similar trajectories and their times of flight to the detector are close and concentrated in the peak. Events in the tail are due to background.

3. Calibration of the setup

The main purpose of the detector system is to allow for the reconstruction of the four-momenta of the reaction products with high resolution. The setup includes detectors with a complex structure. For example, LAND consists of 200 independently operating paddles, as has been mentioned above. In order to achieve the desired resolution, all detectors have to be calibrated and synchronized in time. The four-momentum vectors can be reconstructed if the distance from the target to each individual detector is known, and the time of flight together with the particle hit position are measured. The calculation of four-momenta is described in Section 4.2.

3.1 Time-of-flight and position measurements

The measurement principle is the same for LAND and TFW paddles and is schematically presented in Fig. 3.1. All times are measured relative to the POS2 detector, which is used to define a common start. When a particle hits a paddle

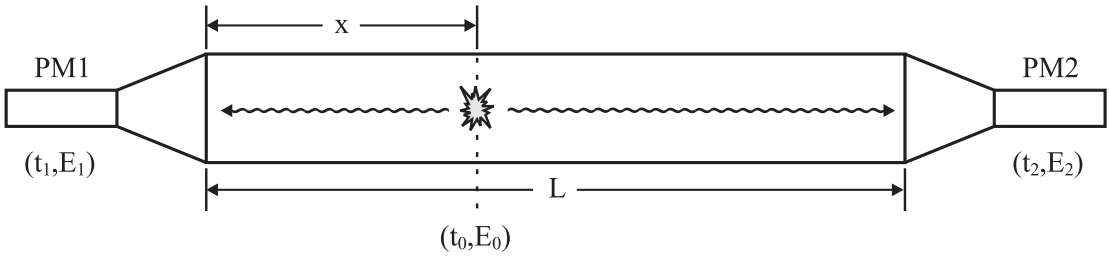

Figure 3.1: Detection principle in one paddle. Particle, hitting the module at position x and time t_0 deposits energy E_0. Times and energies, measured by the two photomultipliers are (t_1, t_2) and (E_1, E_2), respectively.

at position x along the paddle at time t_0, then the two times measured by the photomultipliers are

$$t_1 = t_0 + \frac{x}{v_{sc}} \qquad \text{and} \qquad t_2 = t_0 + \frac{L-x}{v_{sc}}, \tag{3.1}$$

where v_{sc} is the effective velocity of light in the scintillator and L the paddle length. The difference in arrival times of two signals serves for the localization of the hit position and their sum gives the time of the hit:

$$x = \frac{t_1 - t_2}{2} \cdot v_{sc} + \frac{L}{2} \qquad \text{and} \qquad t_0 = \frac{t_1 + t_2}{2} - \frac{L}{2v_{sc}}. \tag{3.2}$$

The constants L and v_{sc} can be included into the calibration parameters, leading to the following very simple relations:

$$x = \frac{t_1 - t_2}{2} \cdot v_{sc} \qquad \text{and} \qquad t_0 = \frac{t_1 + t_2}{2}. \tag{3.3}$$

This method provides an accuracy for determination of the coordinate of the hit along the paddle of $\sigma \approx 3$ cm.

Alternatively, position information can be obtained using the energy signals. Here, the measurement is based on the light attenuation in the scintillator material. If E_0 is the energy deposited by a particle, then the amplitudes of the signals measured by the two photomultipliers are

$$E_1 = E_0 \cdot e^{-\lambda \cdot x} \qquad \text{and} \qquad E_2 = E_0 \cdot e^{-\lambda \cdot (L-x)} \ , \tag{3.4}$$

where λ is the light attenuation coefficient, x the position of the flash and L the length of the paddle[1]. The quantity $\log(E_1/E_2)$ is then independent on the deposited energy E_0, and the hit position x can be obtained. On the other hand, the geometric mean, $\sqrt{E_1 \cdot E_2}$, provides the deposited energy independently on the hit position. Using this method one can determine the position with $\sigma \approx 25$ cm. Therefore, the coordinates are reconstructed using the measured times.

For LAND, both mentioned methods give hit positions in the direction along the paddle. Coordinates in the other two directions are obtained by randomization over the paddle width and thickness. For the 10 cm wide paddles, such an approach provides again a resolution of $\sigma \approx 3$ cm.

The detection efficiency for charged particles in TFW is very close to 100%. Therefore, each ion usually produces signals in two crossing paddles, one horizontal and one vertical, belonging to different layers. The horizontal paddle delivers the x coordinate, whereas the vertical one serves for determination of the y position. The values t_0 and E_0 are measured in both paddles and the mean value is calculated.

3.2 Stability of calibration parameters with time

For some years, the basic calibration procedures are automated and performed using the *land02* code, described in Ref. [39]. Thanks to this fact, one can

[1] It was found recently, that higher order corrections are needed.

not only calculate a set of calibration parameters, but also investigate their behavior during the experiment and introduce time-dependent corrections if needed. Below, the calibration of time signals in LAND is described in detail.

The conversion from electronic channels to nanoseconds is performed with the help of a pulser calibration. The pulser is generating 11 pulses with an interval of 10 ns. In order to be able to let the first pulse remain at zero, regardless of the drifts during the experiment in the electronic chain seen by the time calibrator module, a time calibrator offset (T_{tcal}) is introduced. Consequently, time in nanoseconds is calculated as

$$T = a \cdot N_{ch} + T_{tcal}, \tag{3.5}$$

where N_{ch} is the raw time signal in channels and a the TDC gain in ns/ch. In total 656 files with data are recorded during the experiment. If one observes the behavior of the parameter as a function of time, it is necessary to minimize statistical fluctuations of the calculated parameters, using more data files. From the other side as many points as possible are needed. A compromise solution in this particular case is to chain every three files together. The T_{tcal} parameters are calculated for each of the 400 PM tubes. It is found, that for almost all channels, the parameter is drifting as shown in the upper left panel of Fig. 3.2. Since we mainly operate with time differences, a common drift of all channels is equivalent to a stable behavior. However, some channels are drifting in a different way as shown in the upper right panel of Fig. 3.2. Thus, for each channel, the change of the T_{tcal} parameter over time can be split into two components, one is common to all channels, the other is specific to problematic channels. In order to enhance the individual corrections needed, the common component should be eliminated, using the following procedure. If one finds differences between T_{tcal} parameters, calculated for the first file and for the second one, the mean value of the main group of them is declared as a common shift for all channels between these two files. A typical distribution of differences between two sets of parameters is shown in Fig. 3.3. The common shift can be found using a gaussian fit of the obtained distribution. The same operation was repeated for the first and the third files, the first and the fourth files and so on. When all shifts are already known, the common drift of parameter can be eliminated using the equation

$$T^{cor}_{tcal}(i) = T_{tcal}(i) - T_{tcal}(1) - \Delta T(i, 1), \tag{3.6}$$

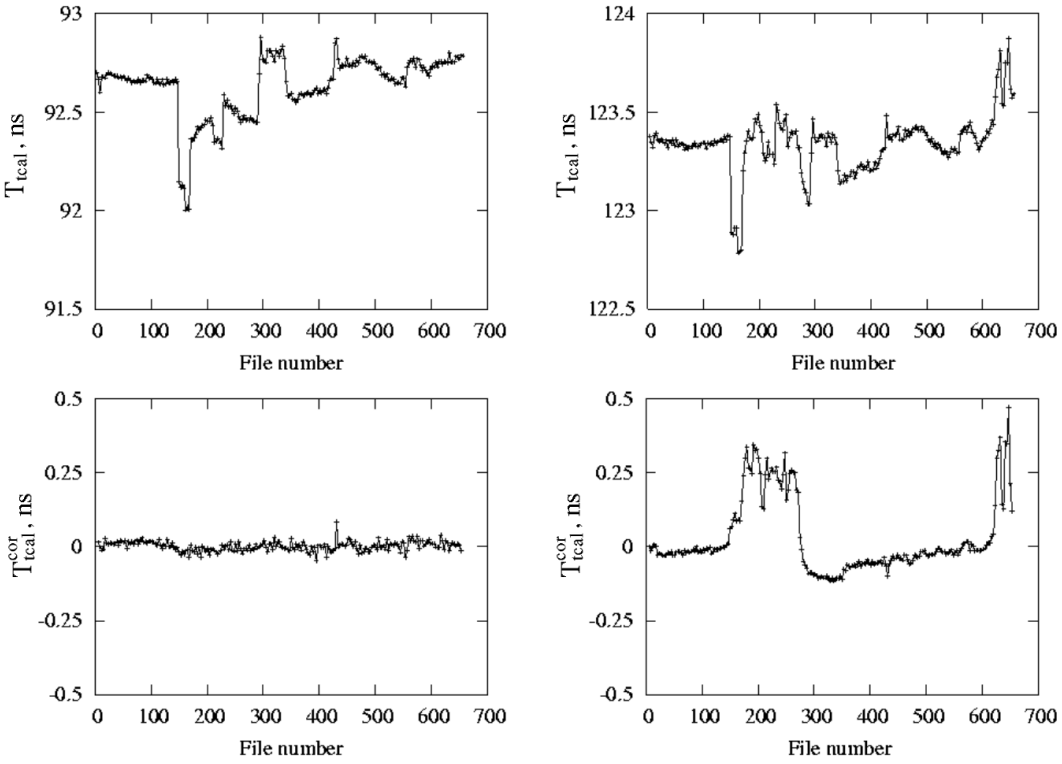

Figure 3.2: Time dependence of the T_{tcal} parameter. The upper left panel represents an example of a common drift of all channels, the upper right corresponds to a problematic channel. The lower panels represent the behavior after correction.

where $\Delta T(i,1)$ is the shift between i^{th} and first files, $T_{tcal}(i)$ is the time calibrator offset calculated for the i^{th} file and $T_{tcal}(1)$ the time calibrator offset calculated for the first file. As a result, for those channels where there are only common shifts, stable behavior is achieved (Fig. 3.2, lower left panel) whereas, for others the anomalous component (Fig. 3.2, lower right panel) could be extracted. Due to subtraction of the $T_{tcal}(1)$ parameter, all $T^{cor}_{tcal}(i)$ values are close to zero. After the anomalous components are found, a manual correction for 25 problematic channels has been applied.

The next step is the internal calibration of LAND. It is usually performed using interactions of cosmic particles, which present a natural source of radiation. The hard component of the cosmic ray flux at sea level, mainly muons (97%), has sufficiently high energy (mean energy 2 GeV) to penetrate the concrete ceiling of the cave, in which LAND is installed, and to traverse the neutron detector with approximately the speed of light. The total incident flux on LAND is estimated to be 600 Hz. Thus, after a short time, the detector is completely scanned by

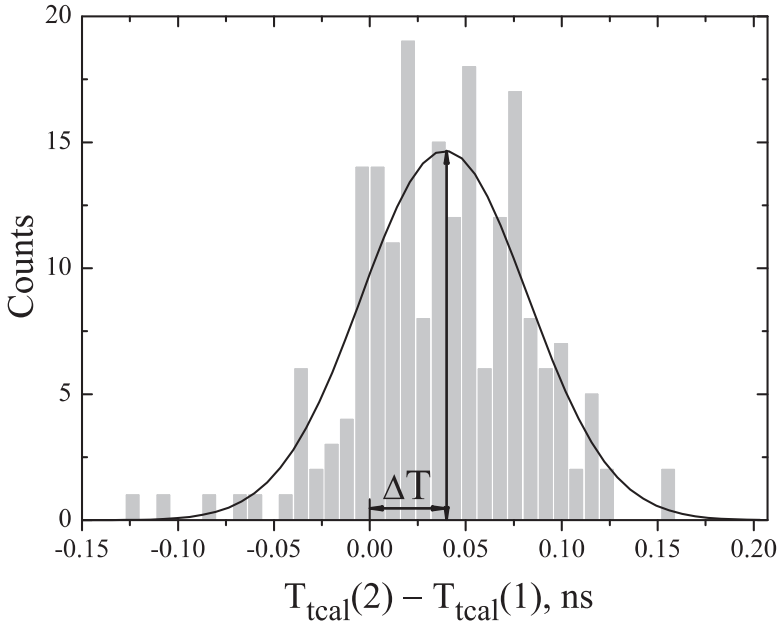

Figure 3.3: Differences between channelwise T_{tcal} parameters calculated for the first and the second files. The mean value gives common shift (ΔT) of all channels between these files.

the cosmic rays. The position of light production is calculated from the time difference of two signals from the PM tubes of each paddle (Eq. 3.2). Data for pairs of crossing paddles are collected into two-dimensional histograms. For each particular crossing, the position along one paddle is uniquely defined by the actual position of the second paddle, and vice versa. In such a way, the offset T_{diff} and the effective velocity in the paddle are found by linear fitting. Taking into account, that the muon velocity is close to the speed of light, a relative time calibration can be performed for the PM time signals. In other words, two hits of the same muon, but in neighboring paddles, should satisfy the condition

$$\frac{t_1 + t_2}{2} - \frac{t_3 + t_4}{2} = C, \tag{3.7}$$

where t_1 and t_2 are times measured in one paddle, while t_3 and t_4 measured in the other paddle. The constant C is the time of flight between two paddles, defined by their thickness. The synchronization is achieved by means of an offset T_{sync}, calculated per paddle, which is added to both PM tube time signals. In view of the fact that there is no way to assure the functionality of some chosen PM tube in the detector, instead of binding the calibration to a reference paddle, a more general condition is introduced [40]:

$$\sum_{all\_paddles} T_{sync} = 0. \tag{3.8}$$

When all offsets are found, the time signals in two PMs of the same paddle, T_1 and T_2, are calculated using the expressions

$$\begin{cases} T_1 = a_1 \cdot N_{ch1} + T_{tcal1} + T_{diff} + T_{sync}, \\ T_2 = a_2 \cdot N_{ch2} + T_{tcal2} - T_{diff} + T_{sync}. \end{cases} \tag{3.9}$$

For the calibration, data from a dedicated cosmic run before the experiment were taken. In order to check the calculated parameters, they are introduced into the code, and if they are correct, then a recalculation of the parameters should result in zero differences. To verify this, data from muon hits, that happened during the experiment between beam spills, were used. For every three files out of the available 656, the parameters T_{diff} and T_{sync} were recalculated for all 200 paddles. The behavior of these parameters during the experiment was investigated. The offset T_{diff} showed stable behavior, while the T_{sync} parameter was drifting for some channels, as shown in the right panel of Fig. 3.4, as compared to the left panel which represents a stable channel. In both cases, statistical fluctuations are observed. Using these data, an additional time-dependent correction of the T_{sync} parameter was applied for 5 unstable channels. After the parameter recalcula-

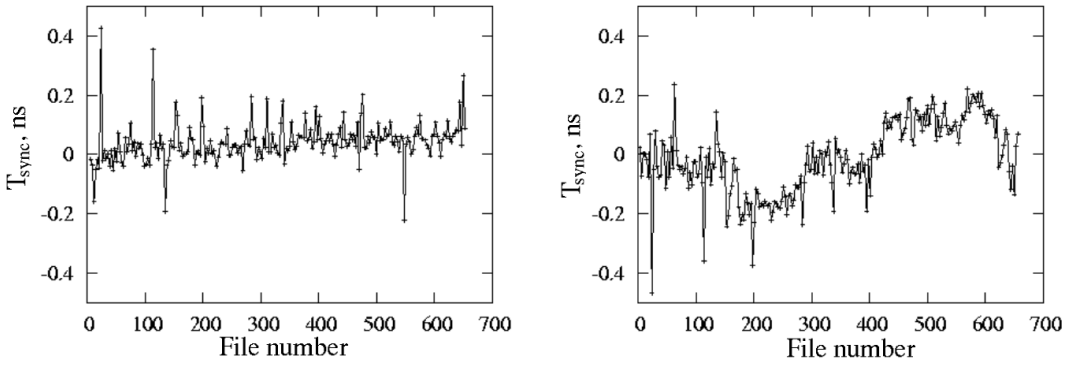

Figure 3.4: Time dependence of the offset T_{sync}, used for time synchronization of the paddles. The left panel shows stable parameter behavior and the right panel represents an unstable case. Statistical fluctuations are observed in both plots.

tion no further drifts are observed, which indicates that the internal calibration procedure for LAND has converged.

For the TFW detector the pulser calibration was performed in the same way, as for LAND. The offset T_{tcal} revealed unstable behavior and had to be

corrected in 11 channels out of 64. For the intrinsic calibration of TFW, the heavy ion hits are used. Usually the detector is not completely illuminated, especially in the y direction. Each ion is detected in both layers of the detector, hitting one horizontal and one vertical paddle. The synchronization of the detector is based on the fact, that hits in two crossing paddles are simultaneous, which means that for the TFW detector the constant C in Eq. 3.7 can be approximated with zero. An investigation of the behavior of the parameters T_{diff} and T_{sync} resulted in the introduction of time-dependent corrections of T_{sync} for 7 paddles out of 32.

3.3 Walk determination and elimination

The walk effect is the dependence of a time signal on its amplitude. It can lead to a significant worsening of the time resolution for a detector signal. Walk is inevitable in measurements where the time signal is produced by a leading-edge discriminator. Using a constant-fraction discriminator (CFD) supposedly should solve the problem, but any improper adjustment of the CFD can lead to an reappearance of walk in a particular channel. In this section, an algorithm for offline determination of the walk effect from collected physics data is presented.

The time t', measured by a single detector channel, can be viewed as

$$t' = t + f(e), \tag{3.10}$$

where t is the real time of the event appearance and $f(e)$ a function containing the amplitude dependence of the measured time. Thus, to perform walk correction, the function $f(e)$ has to be determined and corrected for. If events with known t are available, the function $f(e)$ is easily determined [41]. For the cases with unknown t, events with special properties can be used.

The present algorithm uses data from events where it can be expected (often by geometry), that a simple relationship between the measured times should exist. These can either be the four times of two simultaneously firing neighboring paddles of the LAND and TFW detectors or a single scintillator foil viewed by four photomultipliers, such as the POS detectors. This allows to assume that signals with the above mentioned properties are produced by the same particle and the Eq. 3.7 has to be fulfilled, with the times t_1 and t_2 (t_3 and t_4) belonging to opposite photomultipliers.

Events with hits in neighboring paddles are often characterized by incom-

plete passage through the paddles in beam direction, as shown in Fig. 3.5, therefore different flight paths of the particle in the two paddles cause different energy deposition. Although the energies measured in one paddle are correlated, the finite

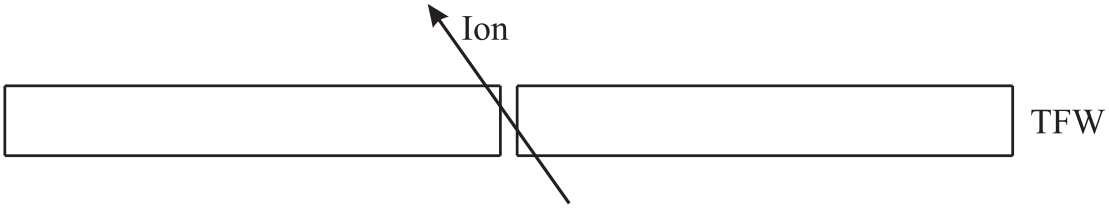

Figure 3.5: The passage of an ion through two neighboring paddles of the TFW detector, top view.

energy resolution allows to have different energies in one channel for the fixed energy in the second channel. In case of the POS detector, all four energies are correlated but because of the small detector size the light attenuation is comparable with resolution, and if three energies out of four are fixed, the fourth energy is not defined uniquely, but varies in a certain range. This allows to apply the present method.

By introducing a value

$$dt = \frac{t'_1 + t'_2}{2} - \frac{t'_3 + t'_4}{2}, \tag{3.11}$$

where t'_1, t'_2, t'_3 and t'_4 are the measured times, the combination of Eq. 3.7 and Eq. 3.10 leads to

$$dt(e_1, e_2, e_3, e_4) = \frac{f_1(e_1) + f_2(e_2)}{2} - \frac{f_3(e_3) + f_4(e_4)}{2} + C. \tag{3.12}$$

Accordingly, the function dt is affected by the walk effect in all four detector channels. If one applies narrow gates on e_2, e_3 and e_4, the corresponding walk functions can be treated as constants and Eq. 3.12 is simplified to

$$f_1(e_1) = 2 \cdot dt(e_1) + C_1, \tag{3.13}$$

where C_1 includes all constant offsets. By looping over e_1, the corresponding walk function is determined. By moving the gates over the whole ranges of e_2, e_3 and e_4 a set of curves

$$f_1(e_1) = 2 \cdot dt(e_1) + C_2 \tag{3.14}$$

is obtained, where the constant C_2 depends on the gate positions. The curves cover partial energy ranges, because of the remaining energy measurement correlations, limiting the obtainable values of e_1 as function of e_2, e_3 and e_4. They are

subsequently merged into one energy dependent function. A walk curve obtained for one of the POS detector channels is shown in Fig. 3.6. As one can see from the figure, the walk effect is in the order of several hundred picoseconds. However, in this particular case, it is not so pronounced within the energy-loss range, covered by one isotope. For example, the energy loss of ^{8}He is below 80 arb. units and in this energy range walk effect amounts to about 250 ps. This fact, in combination with the bad energy resolution of POS detector, explains, why this procedure results in an improvement of the time resolution in the order of several percents.

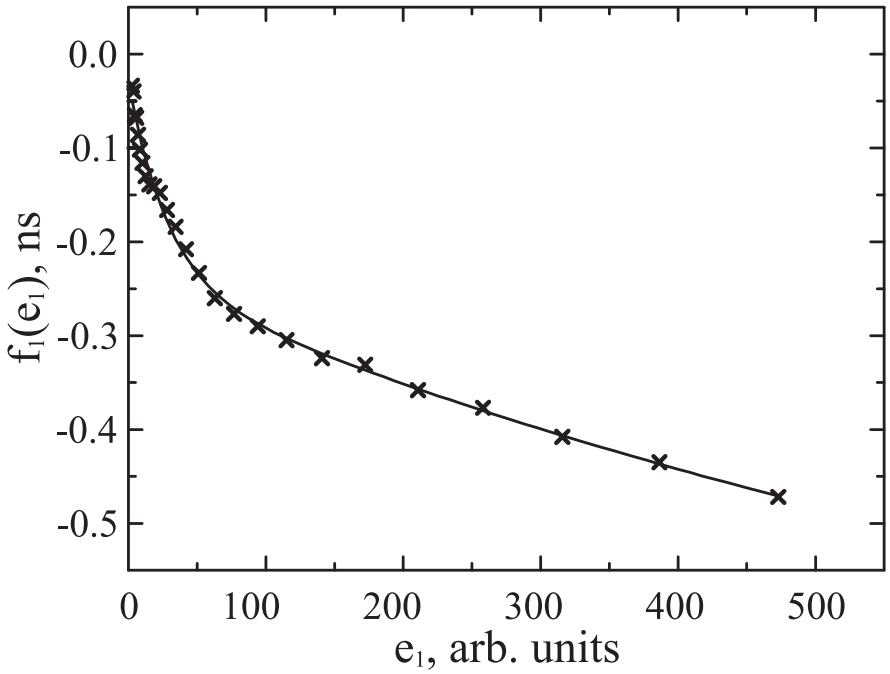

Figure 3.6: Walk curve obtained for one POS channel.

Each paddle, excluding the edges, in the LAND and TFW detectors, has two neighbours. Thus, for most of the paddles, the walk curves can be determined twice and the similarity of the obtained results can be used as a consistency check of the method.

Once the functions $f_i(e_i)$ are obtained, corrections have to be applied to the time-calibrated data, prior to calculation of the offsets T_{diff} and T_{sync}.

The method has been applied to the POS, TFW and LAND detectors. The lack of statistics for LAND and TFW results in no success. For these detectors, an alternative data collection scheme using only two or three signals is under investigation. Curves obtained for the POS detectors were applied and although

achieved improvement of resolution is in the order of several percents, the method has shown to work and will be very helpful in the future, when leading edge discriminators will be used in R^3B setup [42].

3.4 Relative calibration of detectors

After the intrinsic calibration of the detectors has been performed, the next step is their relative calibration. The time of flight between two POS detectors is calibrated using properties of the incoming beam (see Table 2.1). A time T_0, when a particle reaches the target, is defined as

$$T_0 = T_{POS2} + \frac{T_{POS2} - T_{POS1}}{d_{12}} \cdot d_{2t}, \tag{3.15}$$

where d_{12} is the distance between the two POS detectors and d_{2t} the distance between POS2 and the center of the target. The time of flight of reaction products is calculated relative to T_0. Using the velocities of the unreacted beam, corrected for energy loss in the beam line, the time offset for TFW can be found. Relative calibration of LAND is performed assuming, that after one-neutron removal from a two-neutron halo nucleus, the second neutron, being unaffected by the reaction, continues to move forward with the velocity of the incoming beam.

3.5 Time-of-flight resolution

The intrinsic time resolution of the POS, TFW and LAND detectors can be determined using Eq. 3.7. The width of this distribution is connected to the intrinsic resolution of detector. It is applied to crossing paddles of TFW and LAND and to the four time signals of the POS detectors. Results for different isotopes are listed in Table 3.1. The intrinsic LAND resolution is $\sigma_{\mathrm{LAND}} \approx 250$ ps. The accuracy of T_0 determination can then be found, using Eq. 3.15. The resolution for the fragments time-of-flight, σ_{tof}^{calc}, can therefore be calculated. The obtained values are cross-checked using the non-reacting beam. The measurement shows values, σ_{tof}^{exp}, which are unexpectedly high (see Table 3.1). The observed difference can partly be explained by an energy spread in the beam and different trajectories of the particles through the ALADIN magnet. However, the main contribution stems from jitter in the electronics chain common for the LAND and TFW detectors. This effect can be estimated using the time calibrator data. The panels (1),

Table 3.1: Intrinsic time resolution of the POS1, POS2 and TFW detectors and time-of-flight resolution for charged fragments, predicted from detectors resolutions σ_{tof}^{calc}, and being measured in the experiment σ_{tof}^{exp}.

	^{8}He	^{11}Li	^{14}Be
σ_{POS1}, ps	186	139	117
σ_{POS2}, ps	221	165	131
σ_{TFW}, ps	200	148	121
σ_{tof}^{calc}, ps	321	239	192
σ_{tof}^{exp}, ps	532	462	450

(2) and (3) of Fig. 3.7 show a time calibrator peak in the POS, TFW and LAND detectors, respectively. One can see a very narrow peak in POS, while the peak is asymmetric and broad both in the LAND and TFW detectors. Both width and shape of the spectra in the cases of the LAND and TFW detectors are dominated by jitter. The panel (4) of Fig. 3.7 shows the time difference between one POS channel and one TFW channel, which is close to time-of-flight. In this case both shape and width of the spectrum are also dominated by jitter. However, if one looks at time difference between any two TFW channels, as shown in panel (5) of Fig. 3.7, or any two LAND channels, the distributions are narrow. A similarly narrow distribution can be obtained if one looks at time difference between any TFW channel and any LAND channel. An example for these distributions is shown in panel (6) of Fig. 3.7. The narrow distributions in the latter two cases prove, that the jitter is common for all TFW and LAND channels. Therefore, neither the intrinsic resolution of detectors nor the relative timing of TFW and LAND are affected. It is shown, that this jitter in the electronics chain leads to an additional systematical error in measurement of fragments and neutrons time-of-flight without worsening the resolution for relative timing.

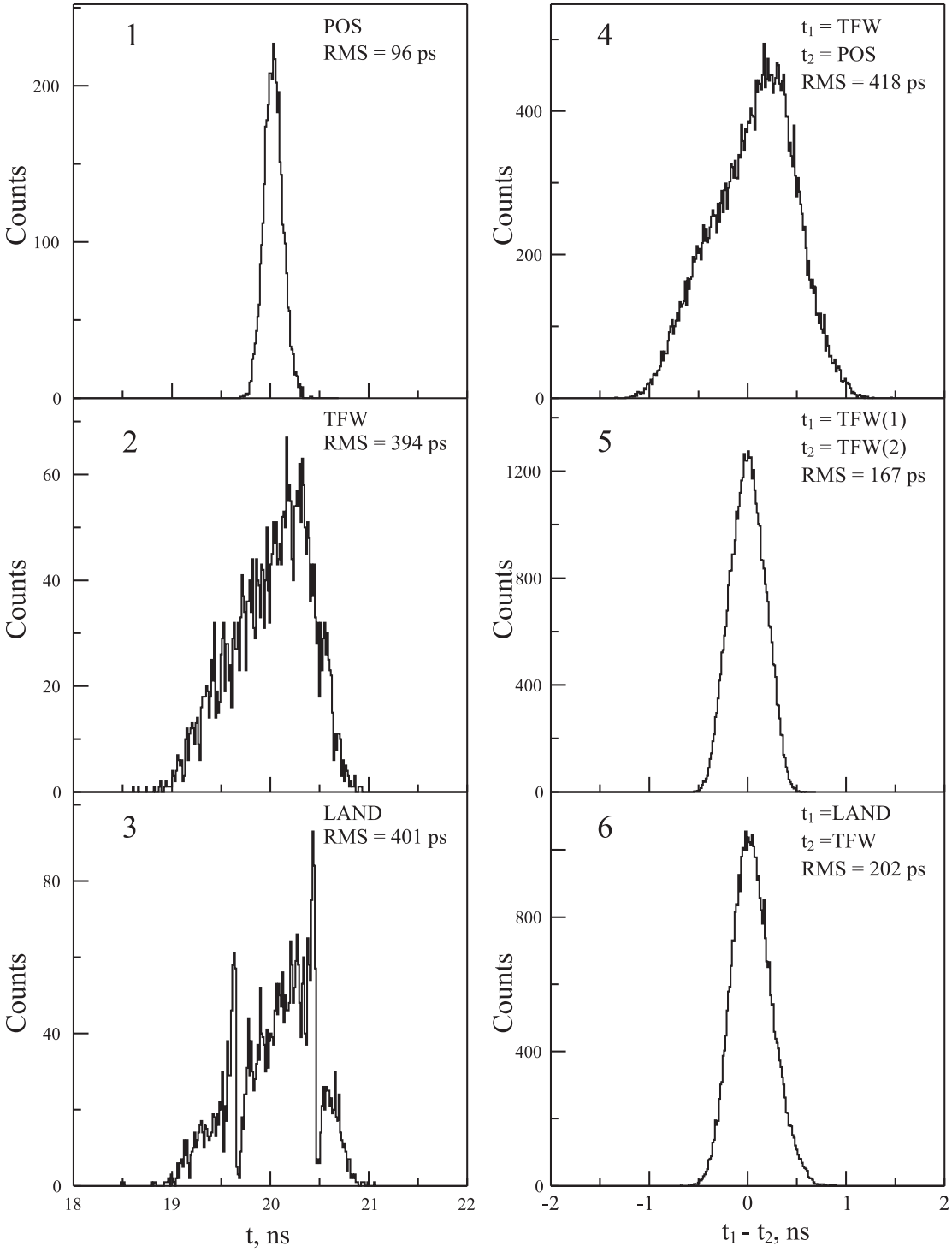

Figure 3.7: The left panels show a single time calibrator peak for different detector channels. The right panels contain distributions of time differences ($t_1 - t_2$) between channels of different detectors.

4. Observables and analysis tools

4.1 Reaction channels

The dominating breakup channels of light loosely bound nuclei at high energies are Coulomb and nuclear dissociation. The cross section of the former process is proportional to Z^2, where Z is the charge of the target nuclei, and is negligibly small for a proton target. The reaction mechanisms, observed in the present experiment, can be divided into three types:

- quasi-free stripping of one of the halo neutrons by the target nucleus. This channel is dominating. For this case, the knocked out neutron is scattered to large angle and is not detected by LAND. The remaining subsystem is unbound and decays into the constituent core and remaining neutrons.
- nuclear excitation. Diffractive dissociation of one of the halo neutrons, the analogue to Fraunhofer diffractive scattering of light on a black sphere. Here, because of scattering angles, most of the neutrons hit LAND [43]. This process allows the detection of all disintegration products of the incoming nucleus, and is therefore used to study its nuclear excitation energy spectrum.
- quasi-free scattering of a proton at a nucleon of a bound cluster inside the nucleus in inverse kinematics. As a result, the nucleon or the cluster is separated from the nucleus, while the rest of the nucleus acts as a spectator. The process leads to the formation of a system consisting of a modified core and the halo neutrons.

In the two first cases, because of both high beam energy and the fact that halo neutrons are loosely bound and spend most of the time outside the core, the remainder of the nucleus acts as a spectator. In contrast to neutrons, protons are deeply bound in the core. The proton binding energy in neutron-rich nuclei is about 20 MeV. Therefore, it is not easy to remove it without affecting the rest of the system and the possibility of momentum transfer to the core has to be taken into account. The diffractive dissociation is supressed on a hydrogen target due to small size of target nuclei.

The cross section for a specific reaction channel is calculated using the following equation

$$\sigma = \frac{M}{\omega N_A}\left(\frac{N_r}{N_{ip}} - \frac{N_r^{et}}{N_{ip}^{et}}\right) \tag{4.1}$$

with the variables

M: molar mass of the target nucleus in g/mol;

ω: target thickness in g/cm^2;

N_A: Avogadro's constant;

N_r: measured number of events in a specific reaction channel;

N_{ip}: measured number of incoming particles;

N_r^{et}: measured number of events in a specific reaction channel with empty target;

N_{ip}^{et}: measured number of incoming particles with empty target.

The number of incoming beam particles and charged reaction fragments is calculated involving the same detectors. Only events, which have produced signals in all of them, are taken into account during the analysis. Therefore, efficiencies of particular detectors do not play a role in the cross section calculation. The only exception is LAND. Efficiency and acceptance of this detector have an influence on the measurement. The correction procedure for these effects will be discussed later.

4.2 Momentum distributions

When all reaction products are identified and for each of them the time of flight and the coordinates of the hits in the detectors are known, the four-momenta $\vec{P} = (E, \vec{p})$ can be reconstructed. Here and below, units with $\hbar = 1$ and $c = 1$ are used. The velocities v of the reaction products are calculated from the time of flight. The total momentum in the laboratory frame is then calculated as

$$p_0 = m_0 v \gamma, \tag{4.2}$$

where $\gamma = \sqrt{1/(1-v^2)}$ and m_0 is the rest mass of the fragment. By measuring polar and azimuthal angles θ and ϕ, as defined in Fig. 2.4, the momentum components p_x, p_y and p_z can be found:

$$\begin{cases} p_x = p_0 \sin\theta \cos\phi \\ p_y = p_0 \sin\theta \sin\phi. \\ p_z = p_0 \cos\theta \end{cases} \tag{4.3}$$

The momentum components of charged fragments are calculated using the coordinates of the hit in MWPC2 and the time of flight between the target and the

TFW detector. The polar and azimuthal angles of neutrons, as well as their time of flight, are calculated using LAND.

4.3 Invariant mass and relative energy

For a system consisting of N particles, the total energy E and momentum $\vec{p}$ are

$$E = \sum_{i}^{N} E_i \qquad \text{and} \qquad \vec{p} = \sum_{i}^{N} \vec{p}_i. \tag{4.4}$$

The squared four-momentum of the particle system,

$$\vec{P}^2 = E^2 - \vec{p}^{\,2} = \left(\sum_{i}^{N} E_i\right)^2 - \left(\sum_{i}^{N} \vec{p}_i\right)^2 = \mathcal{M}^2, \tag{4.5}$$

is invariant under Lorenz transformations. The quantity $\mathcal{M}^2$ is also referred to as the invariant mass of the system. The invariant mass method has been successfully used in particle physics for determining the masses of very short-lived particles by measuring their decay products [44]. Nowadays, it is also widely used in nuclear physics for the study of systems whose production in nuclear reactions is followed by immediate decay.

The so-called relative energy is used in the following. If all reaction products are produced in their ground states, the relative energy is defined as

$$E_N \equiv \mathcal{M} - \sum_{i}^{N} m_i^0, \tag{4.6}$$

for the system consisting of N particles with rest masses m_i^0. This quantity represents the excitation energy of the system above the N-particle threshold. Usually, in this kind of experiments, total relative energy in the system does not exceed several MeV, therefore the system can be treated using non-relativistic relations. In the center of mass system $E_N = p_N^2/2\mu$, where p_N is the relative momentum of the N particles and μ the reduced mass. In the present work relative-energy spectra are calculated for two-body and three-body systems, consisting of core fragment and one or two neutrons, and are denoted as E_{Cn} and E_{Cnn}, respectively.

4.4 The hyperspherical harmonics method

For the description of three-body systems, it is convenient to introduce a set of so called Jacobi coordinates $\{\vec{\mathcal{P}}_1, \vec{\mathcal{P}}_2\}$, which are described in detail in Appendix A. The Jacobi momenta $\vec{\mathcal{P}}_1$ and $\vec{\mathcal{P}}_2$ are constructed as

$$\begin{cases} \vec{\mathcal{P}}_1 = \left(\dfrac{\vec{p_i}}{m_i} - \dfrac{\vec{p_j}}{m_j} \right) \dfrac{m_i m_j}{m_i + m_j} \\ \vec{\mathcal{P}}_2 = \left(\dfrac{\vec{p_l}}{m_l} - \dfrac{\vec{p_i} + \vec{p_j}}{m_i + m_j} \right) \dfrac{m_l (m_i + m_j)}{m_i + m_j + m_l}, \\ \vec{\mathcal{P}}_{cm} = \vec{p_i} + \vec{p_j} + \vec{p_l} \end{cases} \tag{4.7}$$

where $\vec{p_i}$, $\vec{p_j}$ and $\vec{p_l}$ are the conventional momenta of individual clusters in the projectile system with masses m_i, m_j and m_l, respectively. The usage of momenta in the projectile system permits to use non-relativistic relations. In the case when two out of three particles are identical, there are two choices of Jacobi coordinate system, the so called T and Y systems, where (ijl) = (123) and (ijl) = (231), respectively, as shown in Fig. 4.1.

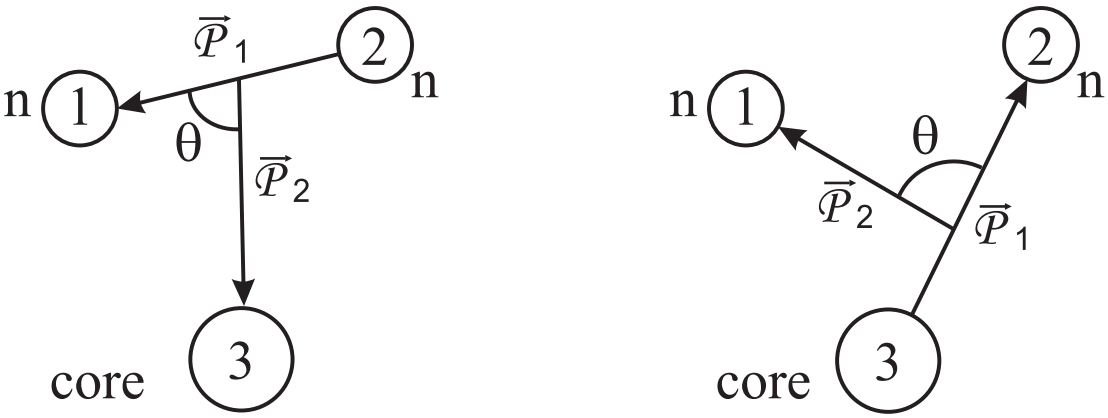

Figure 4.1: Definitions of the T (left frame) and Y (right frame) Jacobi coordinate systems.

The study of systems with more than two constituents exhibits a rich source of information by analysing different types of energy and angular correlations between clusters. The hyperspherical harmonics (HH) method provides a convenient tool for their study. It is described in detail in Appendix B. The method was used for the first time for studies of the nuclear reactions in Ref. [45, 46]. Recently it was applied to the study of electromagnetic dissociation of Borromean nucleus ^{6}He [47]. In the context of HH method the wave function of the three-body

system in the momentum space can be expressed in terms of the hyperspherical coordinates $\{\kappa, \theta_\kappa, \hat{\mathcal{P}}_1, \hat{\mathcal{P}}_2\}$, where

$$\kappa \equiv \sqrt{{\mathcal{P}_1}^2 + {\mathcal{P}_2}^2} \qquad \text{and} \qquad \theta_\kappa \equiv \arctan \frac{\mathcal{P}_1}{\mathcal{P}_2}, \qquad \theta_\kappa \in \left[0, \frac{\pi}{2}\right]. \tag{4.8}$$

The remaining four angles $\{\hat{\mathcal{P}}_1, \hat{\mathcal{P}}_2\} = \{\theta_1, \phi_1, \theta_2, \phi_2\}$ are the common angular coordinates of the Jacobi vectors $\vec{\mathcal{P}}_1$ and $\vec{\mathcal{P}}_2$. The "momentum" κ is connected to the total relative energy of the three-body system via $E_{Cnn} = \kappa^2/2m$, where m is the reduced mass. The hyperangle θ_κ is responsible for the energy distribution between clusters.

The differential cross section integrated over the transferred momentum can be described by

$$\begin{aligned} \frac{d^6\sigma}{dE} \propto & (\sin\theta_\kappa)^2 (\cos\theta_\kappa)^2 \sum_{K,K'} \sum_{l_1,l_1'} \sum_{l_2,l_2'} A^{KL}_{l_1 l_2}(E) A^{K'L}_{l_1' l_2'}(E)^* \\ & \times \sum_{M_L} \Gamma^{l_1 l_2}_{KLM_L}(\Omega_5) \Gamma^{l_1' l_2'}_{K'LM_L}(\Omega_5)^* d\hat{\mathcal{P}}_1 d\hat{\mathcal{P}}_2 d\theta_\kappa, \end{aligned} \tag{4.9}$$

where $\Gamma^{l_1 l_2}_{KLM_L}$ is the hyperspherical function and the complex expansion coefficients are normalized by

$$\sum_K \sum_{l_1,l_2} A^{KL}_{l_1 l_2}(E) A^{KL}_{l_1 l_2}(E)^* = 1. \tag{4.10}$$

The transitions between the T and Y Jacobi coordinate systems are accompanied by a change of HH according to the expression

$$A^{KL}_{l_1 l_2}(T) = \sum_{l_1',l_2'} \langle l_1' l_2' | l_1 l_2 \rangle_{KL} A^{KL}_{l_1' l_2'}(Y), \tag{4.11}$$

where $\langle l_1' l_2' | l_1 l_2 \rangle_{KL}$ are the Raynal-Revai coefficients [48].

By integrating over the orientation of the three-body core + n + n system and over the remaining azimuthal angle, the angular part of the differential cross section (4.9) can be simplified, leaving a dependency on the angle θ between the Jacobi momenta $\vec{\mathcal{P}}_1$ and $\vec{\mathcal{P}}_2$ (see Fig. 4.1) only. It is convenient to introduce the value $\varepsilon = \sin^2\theta_\kappa$, which describes the energy distribution in the system. Note,

that $\varepsilon = E_{nn}/E_{Cnn}$ in the T-system and $\varepsilon = E_{Cn}/E_{Cnn}$ in the Y-system. In terms of these variables, the cross section can be given as

$$\begin{aligned}\frac{d^3\sigma}{dE\,dcos\theta\,d\varepsilon} \propto & \frac{\sqrt{\varepsilon(1-\varepsilon)}}{4\pi} \sum_{K,K'} \sum_{l_1,l_1'} \sum_{l_2,l_2'} A^{KL}_{l_1 l_2} (A^{K'L}_{l_1' l_2'})^* \\ & \times \sqrt{(2l_1+1)(2l_2+1)(2l_1'+1)(2l_2'+1)} \Psi^{l_1 l_2}_K(\varepsilon) \Psi^{l_1' l_2'}_{K'}(\varepsilon) \\ & \times \sum_m \sqrt{\frac{(l_1-m)!(l_1'-m)!}{(l_1+m)!(l_1'+m)!}} C^{Lm}_{l_1,m,l_2,0} C^{Lm}_{l_1',m,l_2',0} P^m_{l_1}(\theta) P^m_{l_1'}(\theta),\end{aligned} \tag{4.12}$$

where $\Psi^{l_1 l_2}_K(\varepsilon)$ is the hyperangular function, $C^{Lm}_{l_1,m,l_2,0}$ the Clebsh-Gordan coefficients and $P^m_{l_1}(\theta)$ the associated Legandre polinomial. The expression 4.12 can be rewritten as

$$\frac{d^3\sigma}{dE\,dcos\theta\,d\varepsilon} = W(E,\varepsilon,\theta)\frac{d\sigma}{dE}. \tag{4.13}$$

where $W(E,\varepsilon,\theta)$ is the correlation function normalized to unity:

$$\int_{-1}^{1}\int_{0}^{1} W(E,\varepsilon,\theta) d\varepsilon\, dcos\theta = 1. \tag{4.14}$$

In the analysis, because of low statistics, the whole range of relative energy is being split into two intervals and two different projections of the correlation spectra: the fractional energy spectrum $W(\varepsilon) = \int_{-1}^{1} W(\overline{E},\varepsilon,\theta) d\cos\theta$ and the angular distribution $W(\theta) = \int_{0}^{1} W(\overline{E},\varepsilon,\theta) d\varepsilon$ are averaged within relative energy ($\overline{E}$) intervals. As follows from Eq. 4.12, for the given relative energy, the hyperangular part $W(\varepsilon)$ of the correlation function is defined by hyperangular functions and angular part $W(\theta)$ is described by Legandre polynomials. Figure 4.2 shows the examples of distributions $W(\varepsilon)$ for different combinations of quantum numbers K, l_1 and l_2.

4.5 Relative-energy spectra

In case of proton knockout a modified core fragment and two neutrons are produced in the final state. If one of the neutrons carries a transverse momentum larger than 60 MeV, it does not hit LAND. Its interaction with the system consisting of the core and the remaining second neutron is therefore considered to

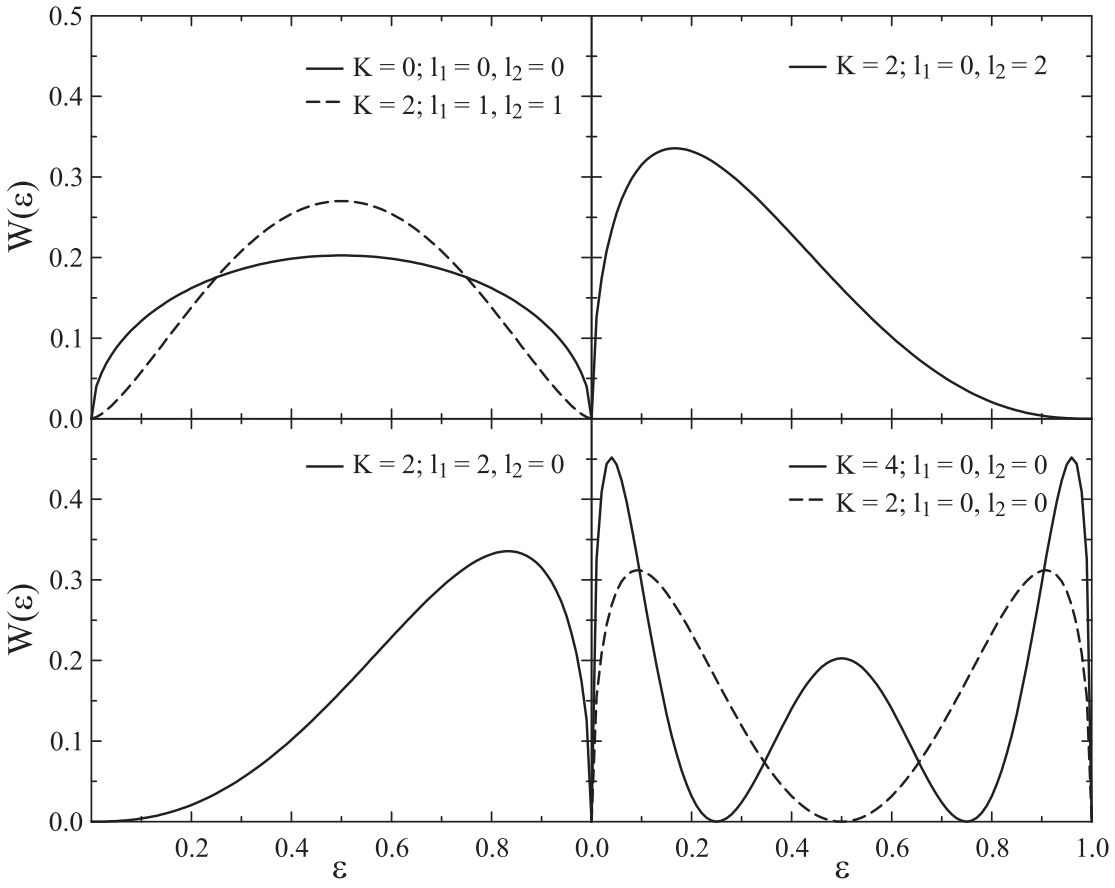

Figure 4.2: Examples of fractional energy distributions $W(\varepsilon)$ for different combinations of quantum numbers K, l_1 and l_2. The case of $K = 0$, $l_1 = 0$ and $l_2 = 0$ corresponds to phase space distribution, $W(\varepsilon) \sim \sqrt{\varepsilon(1-\varepsilon)}$.

be negligible. In the following this is referred to as a one-neutron event. Another type of reaction leading to the same final state is one-neutron knockout, where the knocked out neutron is scattered to large angles and the second neutron impinges onto LAND.

The particles in the final state (core fragment and neutrons) are not created in the reaction. They are already present in the projectile nucleus from the very beginning and are just released by the collision. Thus, the relative-energy distribution of the breakup fragments originates from initial state wave function and is modified by the final-state interaction. The populated resonances are usually described in terms of R-matrix theory [49] where the initial distribution is not taken into account. The obtained spectra are fitted using a Breit-Wigner

parametrization for resonances:

$$\frac{d\sigma}{dE_{Cn}} \propto \frac{\Gamma_l(E_{Cn})}{(E_r + \Delta_l(E_{Cn}) - E_{Cn})^2 + \frac{1}{4}\Gamma_l(E_{Cn})^2}, \tag{4.15}$$

where E_{Cn} is the relative energy in the core plus neutron two-body system and E_r the energy above the core plus neutron threshold. The dependence of the resonance width, $\Gamma_l(E_{Cn})$, on the relative energy and on the angular momentum is given by $\Gamma_l = 2P_l(E_{Cn})\gamma^2$, where γ^2 is the reduced width and $P_l(E_{Cn})$ the penetrability through the centrifugal barrier for a neutron with orbital angular momentum l [49]. The energy dependence of the resonance shift, $\Delta_l(E_{Cn})$, is determined by the relation $\Delta_l(E_{Cn}) = -[S_l(E_{Cn}) - B]\gamma^2$, where $S_l(E_{Cn})$ is the shift function and $B = S_l(E_r)$ [49].

The validity of such an approach is investigated in Ref. [50]. It is shown, that in case of strong final-state interaction, the initial relative-energy distribution is strongly modified, and the obtained spectrum can be treated as describing the final system only. It is the case for systems like ^{5}He, ^{7}He, ^{10}Li and ^{13}Be, which are unbound but if one adds one more neutron into any of these systems, the binding energy gained from the neutron pairing is enough to make the system bound. It is possible only in case of a strong interaction between the core and the neutron. If one moves beyond the dripline, where the amount of neutrons exceeds the number of protons so much, that the interaction gets weaker in the system, the situation can be different. Being in "terra incognita" one has to check, if the obtained spectrum can be described as originating from the initial nucleus. Only if it is not the case, one can claim the existence of a resonance state.

The lifetime, τ, of each resonance is directly related to the resonance width Γ through $\Gamma = \hbar/\tau$. In the case of a short-lived low-lying resonance, the width Γ can be larger than resonance energy E_r and the resonance overlaps with the threshold. Since the boundary condition for the cross section requires it to vanish at the threshold, the shape of the resonance becomes asymmetric. In the case of a low-lying s-wave resonances $\Gamma(E) \propto E^{1/2}$ and, thus, they often overlap with the threshold. Moreover, in the extreme case of $\Gamma > 4E_r$, the state is named "virtual" and can be treated using the expression

$$\frac{d\sigma}{dE_{Cn}} \propto p_{Cn} \left[\frac{1}{k^2 + p_{Cn}^2}\right]^2 \left[\cos\delta + \frac{k}{p_{Cn}}\sin\delta\right]^2, \tag{4.16}$$

with

$$p_{Cn} \cot \delta = -\frac{1}{a_s} + \frac{1}{2} r_0 p_{Cn}^2 + \mathcal{O}(p_{Cn}^2). \tag{4.17}$$

Here δ is the s-wave phase shift, a_s the scattering length, p_{Cn} the relative momentum in the core + n system, r_0 the effective range parameter and $k = \sqrt{2\mu\epsilon_{2n}}$, where μ is the reduced mass. In case of low momentum transfer to the core, value ϵ_{2n} should be close to the two-neutron separation energy, S_{2n}, in the mother nucleus [51]. In order to check the hypothesis about negligibility of momentum transfer, ϵ_{2n} is used as a free parameter of the fit. The effective range parameter does not have a significant influence on the shape of the spectrum obtained from Eqs. 4.16 and 4.17; a value of $r_0 = 3$ fm is used.

The obtained relative-energy spectra are fitted by a sum of Eq. 4.15 and Eqs. 4.16 and 4.17, folded with the experimental energy resolution function. In case of two-neutron events, the relative energy E_{Cnn} is used instead of E_{Cn} in Eq. 4.15. For the three-body systems two decay models, di-neutron emission and neutron emission leaving core + n system with zero relative energy, give the same result.

4.6 Virtual states in different theoretical models

The s-wave scattering at low energies can be described using several models:

- the effective-range approximation,
- the R-matrix reaction theory,
- the collision S-matrix.

The physical meaning of the model parameters is different for different models. However, connections between parameters from different models can be established.

The cross section for the scattering of two particles interacting via short-range potential can be described as

$$\frac{d\sigma}{dE_{Cn}} \propto \frac{\sin^2 \delta}{p_{Cn}}. \tag{4.18}$$

This equation is also known as Watson-Migdal factor [52, 53].

The effective-range approximation represents a variational principle applied for the solution of the corresponding Schrödinger equation. In case of s-wave scattering $p_{Cn} \cot \delta$ can be expanded as a power series of p_{Cn}^2 (see Eq. 4.17), where two parameters are enough to reproduce the cross section up to several MeV. The method can be used for any radius, depth and shape of the potential. Therefore, the effective-range expansion provides a model-independent description of a low-energy phase shift.

In case when the scattering length $a_s > 0$, the peak in the relative-energy cross section is especially intense and narrow if the potential describing the binary system has a bound state close to the threshold. The value of a_s is larger if the state is closer to the threshold. A negative scattering length $a_s < 0$ appears with decrease of the well depth, when the bound level is pushed into the continuum and becomes a resonance state. The absolute value of negative a_s is increasing with decreasing energy difference between the resonance position and the threshold energy.

The most popular and convenient formalism for the description of resonance reactions is the R-matrix theory. In this framework the existence of s-wave resonance state without a centrifugal barrier can only be explained by strong configuration mixing. The resonance state is described by two parameters, the resonance energy E_r and the resonance width $\Gamma_l(E_r)$. The relative-energy spectrum can be reproduced using Eq. 4.15, with $\Gamma_0(E_{Cn}) = \sqrt{E_{Cn}/E_r}\,\Gamma_r$, where $\Gamma_r = \Gamma_0(E_r)$. The resonance shift, $\Delta_l(E_{Cn})$, is equal to zero in the case of $l = 0$. If a_s and r_0 are known, combining Eqs. 4.15 and 4.18, the resonance position E_r and the resonance width Γ_r can be found. For a broad resonance the position of the maximum in the cross section is shifted towards low energy and does not correspond to the resonance energy E_r.

In scattering theory the collision matrix (or S-matrix) is defined as an unitary matrix connecting asymptotic initial and final states of interacting particles. A stable bound state is interpreted as a pole of the S-matrix at a purely imaginary value ik_0, with $k_0 > 0$, in momentum space or at an energy $E_s = -k_0^2/2\mu$. The energy E_s can be approximately evaluated from the parameters of the effective-range approximation using the expression [54]

$$E_s \simeq -\frac{\hbar^2\gamma^2}{2\mu} \qquad \text{with} \qquad \gamma \simeq \frac{1}{a_s} + \frac{1}{2} r_0 \gamma^2. \tag{4.19}$$

The value a_s can be positive in two cases: either the state is bound or the interaction is repulsive. A resonance state is characterized by the position of the pole in the S-matrix which corresponds to the roots of the denominator in Eq. 4.15. The R-matrix parameters are connected to the S-matrix poles in the complex energy plane E_s by the following expression [55]

$$E_s = E_r[1 - 2\lambda^2 - 2i\lambda\sqrt{1-\lambda^2}] \qquad \text{with} \qquad \lambda = \frac{\Gamma_r}{4E_r}. \tag{4.20}$$

As follows from Eq. 4.20, in case of a narrow resonance, when $\lambda \ll 1$, the pole energy is $E_s \approx E_r - \frac{1}{2}\Gamma_r$. If the resonance is broad and $\Gamma_r > 4E_r$, the pole moves into the negative energy region in the complex energy plane, but in this case does not correspond to a bound state. In terms of the S-matrix formalism such states with asymmetric peaks at low energy in s-wave scattering of neutrons are called anti-bound or virtual states. An anti-bound state has no definite lifetime. The R-matrix theory associates such peaks with very broad resonance states.

In the analysis of the present experiment the relations listed above are used to establish connections between different theoretical models. The results of the data analysis using the effective-range approximation are linked to the conventional language of the R- and S-matrix formalisms.

4.7 The least-squares method

The analysis of the experimental data was performed using least-square fit of theoretical expressions folded with the response function of the experiment to the measured distributions. If a variable y_i is measured at k points, x_i, with an error σ_i (i = 1, 2, ..., k) it is possible to fit a function $f(x; a_1, a_2, ..., a_m)$ to the data. The parameters $a_1, a_2, ..., a_m$ are unknown and have to be determined. The number of points must be greater than the number of parameters. The method of least squares states, that the best values of a_j are those for which the sum

$$\chi^2 = \sum_{i=1}^{n} \left[\frac{y_i - f(x_i; a_j)}{\sigma_i} \right]^2 \tag{4.21}$$

is minimum. One can see, that Eq. 4.21 is just the sum of the squared deviations of the data points from the curve $f(x_i)$ weighted by the respective errors on y_i. The method is also referred to as χ^2 minimization.

To find the values of a_j one must solve the system of equations

$$\frac{\partial \chi^2}{\partial a_j} = 0, \quad j = 1, 2, ..., m \tag{4.22}$$

and determine the real minimum.

In case of k independent data points being used to extract m parameters, the degrees of freedom is thus $n = k - m$ and the value χ^2/n should be close to unity for a good quality fit [56].

The probability density function for the value of χ^2 depends on degrees of freedom and is represented by

$$f(x, n) = \frac{1}{2^{n/2}\Gamma(n/2)} x^{(n/2)-1} e^{-x/2}, \tag{4.23}$$

where $\Gamma(n/2)$ is the gamma function. The probability density function can be used to estimate the confidence level of the fit. Figure 4.3 shows the probability

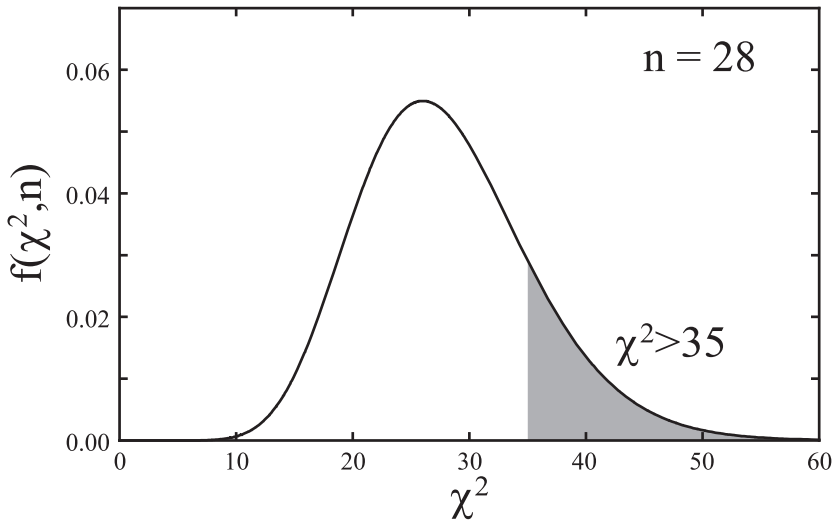

Figure 4.3: The probability density distribution of χ^2 for 28 degrees of freedom. The area marked by gray color denotes the probability for χ^2 to be above 35.

density distribution for the case of 28 degrees of freedom. If the obtained value of χ^2 in this case is larger than 35, for example, then there is 17% probability for the assumed fit to be valid.

5. Corrections for response of the setup

The overall response of the setup is obtained using a Monte-Carlo simulation, based on experimental data. For this purpose, a calibration measurement with monoenergetic neutrons between 70 and 1100 MeV was performed [57], allowing a detailed study of the neutron-induced charged particle showers in LAND. The neutrons were produced in deuteron break-up reactions. One measurement was performed at an energy of 270 MeV/nucleon, close to the neutron energies in the present experiment. The response of the LAND detector to a single neutron crossing the detector area is used in the Monte-Carlo simulations. The overall response of the setup is defined mainly by the neutron detector and can be described by the response function $F(E, E')$, where E' is the neutron energy and E the relative energy in the system. This function can be obtained from Monte-Carlo simulation and parametrized by the expression given in Ref. [58]. The theoretical cross sections are convoluted with the response function

$$\left(\frac{d\sigma}{dE}\right)_{exp} = \int_0^\infty F(E, E') \left(\frac{d\sigma}{dE'}\right)_{theor} dE'. \tag{5.1}$$

The function $F(E, E')$ is normalized to unity for any fixed value of E'

$$\int_0^\infty F(E, E')dE = 1. \tag{5.2}$$

The energy resolution is about 60 keV at low energies, increasing to about 400 keV at an energy of 4 MeV.

Because of the limited acceptance of the setup, the overall efficiency is not constant, but depends on the relative energy. The response function has to include this dependency. In order to simplify the analysis, a correction for the efficiency is performed in a separate procedure. Efficiency curves are obtained for each reaction channel by means of Monte-Carlo simulations, taking into account the momentum distributions of the reaction products and the beam energy. Examples of the obtained curves for the one and two neutron cases are shown in Fig. 5.1. All measured spectra are corrected for the corresponding efficiency curves. As has been mentioned in Section 4.1, only the efficiency of LAND is taken into account. LAND covers an area of 2×2 m^2. Because of the strong kinematical focusing of neutrons emitted from excited projectiles, most of them

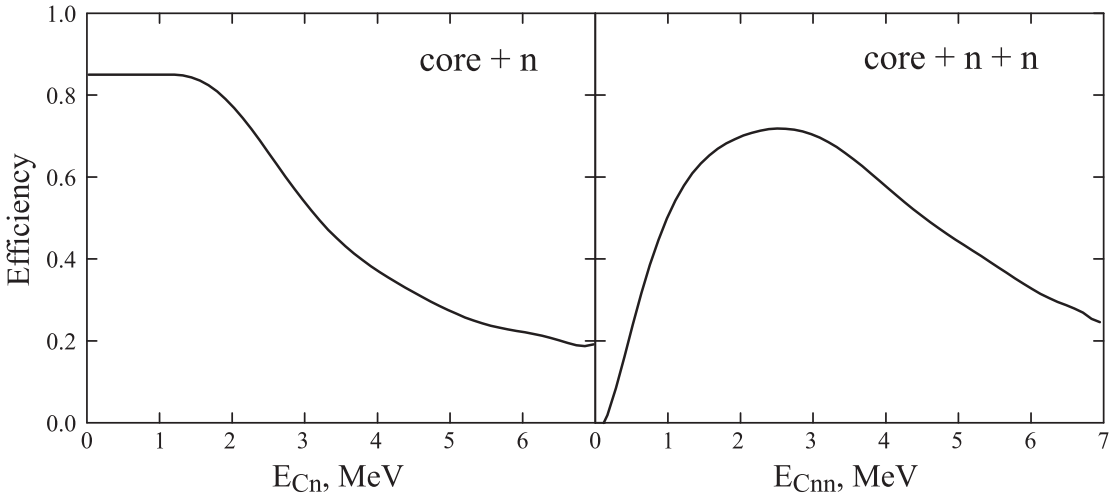

Figure 5.1: Setup efficiency for one neutron (left frame) and two neutron (right frame) events as obtained from a Monte Carlo simulation.

hit the detector. Starting at relative energies of about 2 MeV, neutrons start to escape LAND and the efficiency decreases, as shown in the left panel of Fig. 5.1. In case of two geometrically close neutron hits, which are not separated in time, they can not be resolved, and at low relative energies the efficiency is equal to zero up to certain threshold of about 100 keV. With the increase of relative energy, the probability to resolve two neutrons also increases. At relative energies above 2 MeV, neutrons start to escape LAND and efficiency is decreasing again, as shown in the right panel of Fig. 5.1.

The previous chapter comprises a description of the processes where one or two neutrons traverse the LAND detector. A special tracking routine is then used to disentangle multiple neutron hits. There is a certain probability for this routine to misidentify the number of neutron hits. Therefore, in the analysis of the experimental data the results of the tracking routine are used together with the Monte-Carlo simulation allowing to estimate the so-called "faked" neutron background and correct for it.

6. Neutron knockout channel – ^{10}Li

As already mentioned above, one of the first discovered halo nuclei is ^{11}Li and until now it is one of the most illustrative examples of this phenomenon. Its unbound subsystem ^{10}Li was observed for the first time in 1975 in transfer reaction ^{9}Be(^{9}Be, ^{8}B)^{10}Li at the energy of 121 MeV/nucleon [59]. The obtained spectrum was interpreted as a resonance with $E_r = 0.81(25)$ MeV and width $\Gamma = 1.2(3)$ MeV and was assumed to be the ground state. However, according to theoretical calculations, the measurement relates most probably to the first excited state, characterized by a neutron in $p_{1/2}$ shell, while groud state was suggested to be just above threshold and correspond to a neutron in $s_{1/2}$ shell [60]. After more than 10 years break an experiment studying the proton spectrum from the ^{11}B(π^-, p)^{10}Li reaction showed a broad resonance at the energy of 0.15(15) MeV with $\Gamma \sim 1$ MeV. It was described by a Breit-Wigner parametrization assuming an s-wave behavior for the resonance [61]. Since then the ground state of ^{10}Li was subject to many discussions, which inspired numerous experiments.

A study of the ^{10}Be(^{12}C, ^{12}Ne)^{10}Li reaction showed a p-wave ground state at $E_r = 0.24(6)$ MeV [62]. The distribution of relative velocities between ^{9}Li fragments and neutrons, produced by fragmentation of ^{18}O at the energy of 80 MeV/nucleon contained a peak around zero, which could not be brought in agreement with the previous results. The best description of this spectrum was achieved with the assumption of an s-wave with a scattering length $a_s < -20$ fm and a p-wave resonance at 0.540 MeV [63, 64]. A similar result could be obtained if ^{10}Li would decay to excited state in ^{9}Li at 2.7 MeV, but all doubts were removed after studying the proton removal from ^{11}Be. It was shown, that the excited state in ^{9}Li is populated only in 7% of all cases [65]. The neutron momentum distributions from coincidence measurements with ^{9}Li after neutron removal from ^{11}Li at the energy of 280 MeV/nucleon and after proton removal from ^{11}Be at the energy of 460 MeV/nucleon were narrow, which could only be explained if the ground state of ^{10}Li was an s-state [66]. The analysis of the invariant-mass spectrum using a Breit-Wigner parametrization for both s-state and p-state showed the ground state to be located at 0.21(5) MeV and a first excited state at 0.62(10) MeV [43].

In the present experiment the relative-energy spectrum of ^{10}Li is obtained in the ^{1}H(^{11}Li, pn)^{10}Li reaction. The measured distribution is shown in Fig. 6.1. The sharp peak at low energy is interpreted as low-

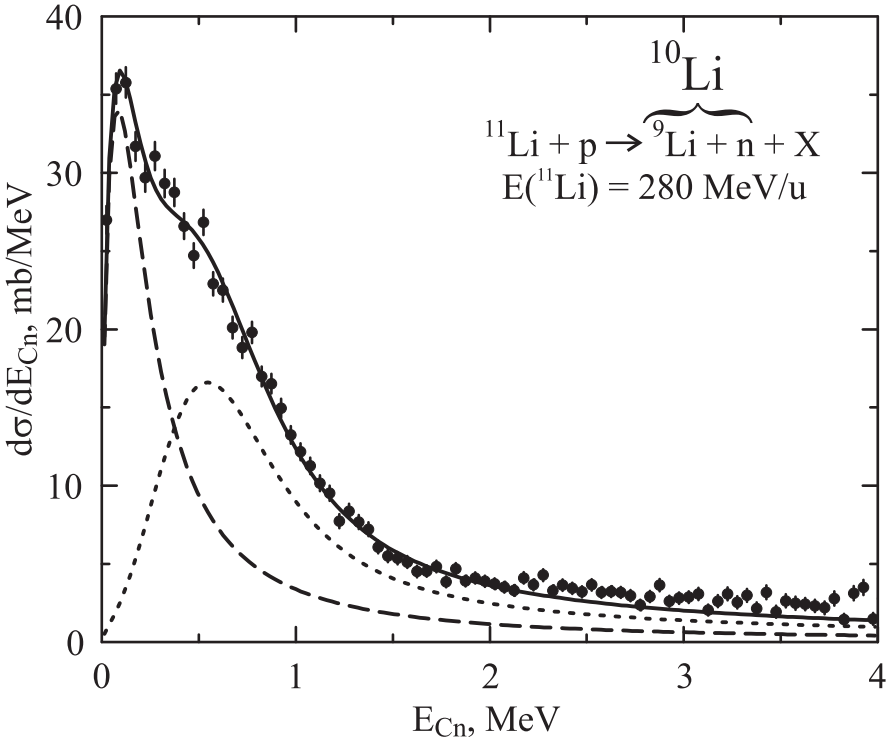

Figure 6.1: Differential cross section as a function of relative energy E_{Cn} for ^{10}Li obtained after one neutron knockout from ^{11}Li. The dashed line corresponds to a virtual s-state, while dotted line represents a p-wave resonance.

lying virtual s-state (dashed line) and described by Eqs. 4.16 and 4.17 with a scattering length $a_s = -22.4(4.8)$ fm. The obtained value for the binding energy $\epsilon_{2n} = 0.352(22)$ MeV is very close to known value of ($S_{2n}(^{11}\mathrm{Li}) = 0.378(5)$ MeV [67]), which confirms the validity of applied model. The second observed state is interpreted as a p-wave resonance at $E_r = 0.566(14)$ MeV above the $^{9}\mathrm{Li} + \mathrm{n}$ threshold with the width of $\Gamma_{l=1}(E_r) = 0.548(30)$ MeV. The resonance shift $\Delta_l(E_{Cn})$, defined in Eq. 4.15, is neglected, due to its small value. For the sake of consistency with the previous interpretations, it has been also omitted in the present analysis.

The obtained parameters together with the results of earlier experiments are presented in Table 6.1. The present results are in perfect agreement with studies of neutron knockout from ^{11}Li at 264 MeV/nucleon using a carbon target [68] and in good agreement with results obtained from a neutron transfer reaction $^{9}\mathrm{Li(d, p)}$ at 2.36 MeV/nucleon [69].

However, there are also slight discrepancies between results obtained on

Table 6.1: Comparison of results obtained for ^{10}Li in the present experiment with some of the previous measurements.

	s-state		p-state	
	a_s, fm	ϵ_{2n}, MeV	E_r, MeV	Γ, MeV
H target	$-22.4(4.8)$	0.352(22)	0.566(14)	0.548(30)
C target [68]	-30^{+12}_{-31}	0.3	0.510(44)	0.54(16)
^{9}Li(d,p) [69]	$-24 \leq a \leq -13$	not given	≈ 0.4	≈ 0.2

carbon target and the present one. Namely, the possible observation of d-strength at about 1.5 MeV in the carbon-target experiment, cannot be observed here. This state can neither be populated in the $^{9}\mathrm{Li}(\mathrm{d},\mathrm{p})$ reaction, while it was observed at $E_r = 1.40(8)$ MeV in a multi-nucleon transfer reaction $^{10}\mathrm{Be}(^{12}\mathrm{C},^{12}\mathrm{N})^{10}\mathrm{Li}$ [70].

7. Proton knockout channels

7.1 Reaction channels ^{14}Be + p $\rightarrow$ ^{11}Li + xn

A search for lithium isotopes heavier than ^{11}Li was performed in 1973 with a 4.8 GeV proton beam bombarding an uranium target. It was shown that ^{12}Li is particle-unbound and an upper limit for the ^{13}Li production cross section was estimated [71].

In the present experiment, at an energy of 305 MeV/nucleon it is possible to perform quasi-free proton knockout from ^{14}Be without disturbing the rest of the system and to observe ^{11}Li nucleus in coincidence with one or two neutrons in the final state. The absence of momentum transfer to ^{11}Li during the reaction can be shown using the fact, that the two-neutron separation threshold for this nucleus is only $S_{2n} = 0.378(5)$ MeV [67], and in case of any significant momentum transfer the nucleus would not survive.

7.1.1 ^{12}Li

The obtained relative-energy spectrum for ^{12}Li is shown in Fig. 7.1. It can be described as a single virtual s-state and being fitted using Eqs. 4.16 and 4.17. The resulting scattering length is $a_s = -13.7(1.6)$ fm, and the value of parameter $\epsilon_{2n} = 1.47(19)$ MeV is very close to the known two-neutron separation energy in ^{14}Be, which equals to 1.26(13) MeV [72]. This fact confirms the validity of applied model as well as the assumption of low momentum transfer to the ^{11}Li nucleus during the reaction. No additional resonances are observed [73]. The obtained result contradicts to the only available shell-model calculation, which predicts two excited states at energies of 0.41 and 0.73 MeV above the ground state [74], respectively.

7.1.2 ^{13}Li

The relative energy of the breakup fragments can be strongly influenced by the initial-state wave function, as has been discussed in Section 4.5. The term correlated background was introduced in Ref. [75] to describe the contribution of an initial-state wave function to the relative-energy spectrum in the final state. It was shown, that a correlated background can exhibit a peak-like structure at low energies and can be falsely interpreted as a resonance. Even if its maximum

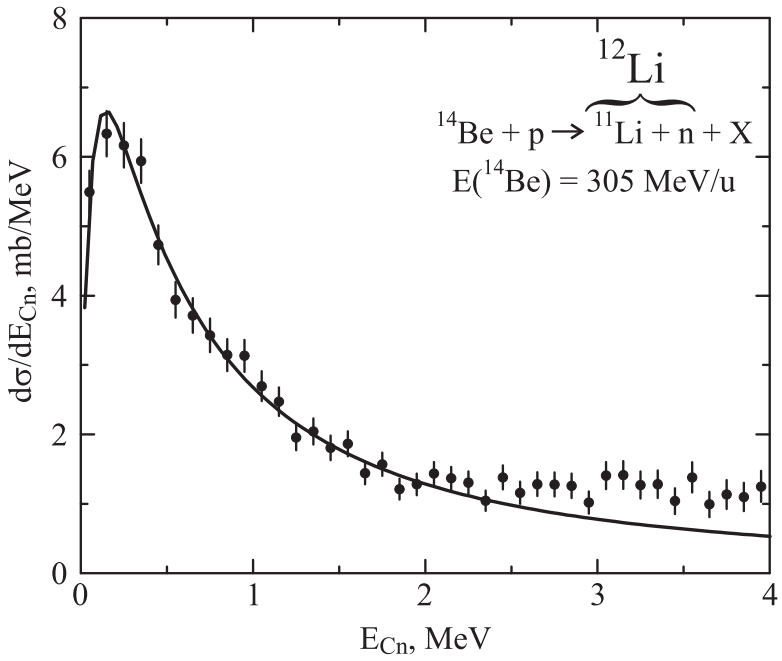

Figure 7.1: Differential cross section as a function of relative energy in the $^{11}\mathrm{Li} + \mathrm{n}$ system obtained after proton knockout from $^{14}\mathrm{Be}$. The spectrum is described as a single virtual s-state with a scattering length $a_s = -13.7(1.6)$ fm.

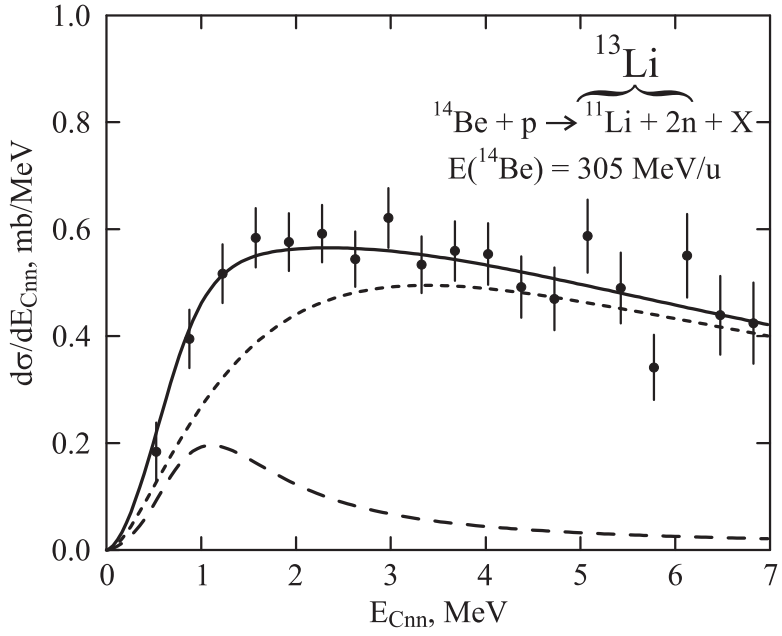

Figure 7.2: Differential cross section as a function of relative energy in the $^{11}\mathrm{Li} + 2\mathrm{n}$ system, obtained from coincidence measurements after proton knockout from $^{14}\mathrm{Be}$. The long-dashed line corresponds to a resonance with $E_r = 1.47(31)$ MeV and $\Gamma \sim 2$ MeV. The correlated background (see text) is shown by a short-dashed line.

is situated far from the region of excited states, it can still influence the derived position of the real resonances. Therefore, it has to be taken into account during the analysis of the spectra.

The two-neutron events have their origin in the fragmentation of the halo nucleus ^{14}Be into four particles p + ^{11}Li + 2n in the final state. The proton is knocked out to a large angle and does not interact with the rest of the system. Moreover, if there is no momentum transfer to the core fragment, meaning that its energy remains the same, it is possible to use a three-body picture of ^{12}Be + 2n in ^{14}Be for the system ^{11}Li+2n. A similar approach was used for ^{10}He, as described in Ref. [76]. In case of proton knockout from ^{14}Be one obtains ^{11}Li plus two neutrons in the final state. It was shown above, that the momentum transfer to the ^{11}Li fragment is low, which serves as a criterion for the applicability of the described model. The ground state wave function of ^{14}Be is expanded in HH, assuming a dominating K = 0 term with a small admixture of K = 2 and K = 4 components. Instead of exact calculations presented in Ref. [75], the following parametrization

$$\frac{d\sigma}{dE_{Cnn}} \propto \frac{E^2_{Cnn}}{(2.21\epsilon_{2n} + E_{Cnn})^{7/2}}, \tag{7.1}$$

with ϵ_{2n} taken to be equal to the two-neutron separation energy of projectile nucleus $S_{2n}(^{14}\mathrm{Be}) = 1.26(13)$ MeV [72] was used.

The differential cross section as a function of the relative energy for the ^{11}Li + 2n system is shown in Fig. 7.2. A good description of the obtained spectra is achieved if it is decomposed into two components: a three-body resonance (long-dashed curve) at an energy of $E_r = 1.47(31)$ MeV and a width $\Gamma = 1 \div 3$ MeV, superimposed on a broad correlated background distribution (short-dashed curve). Such a treatment allows to achieve a reduced χ^2/n of 1.1. Assuming the absence of this resonance it is impossible to reproduce the two-neutron separation energy, the obtained result of $\epsilon_{2n} = 0.78(5)$ MeV differs dramatically from the above mentioned value of 1.26(13) MeV. At the same time, χ^2/n cannot be brought below 1.9. The obtained resonance cross section equals to $\sigma_{res} = 0.49(9)$ mb and can be increased, if one uses the value for ϵ_{2n}, obtained in the analysis of the ^{12}Li spectrum. The spectrum can alternatively be described by several closely-spaced overlapping resonances.

Theory predicts the ground state of ^{13}Li at 3.34 MeV above the ^{11}Li + 2n threshold with the spin and parity $J^\pi = 3/2^-$ [74], which corresponds to four neutrons with total spin 0 surrounding the ^{9}Li core. The nucleus can also be

considered as a Borromean system with two neutrons around the ^{11}Li core. More investigations, both experimental and theoretical, are needed in order to better understand ^{13}Li system.

7.2 Reaction channels ^{11}Li + p $\rightarrow$ ^{8}He + xn

Helium isotopes, heavier than ^{4}He, can be described as a system consisting of an α-particle surrounded by neutrons. Isotopes up to ^{10}He have been observed, while only ^{6}He and ^{8}He are bound (see Fig. 1.3). All others are particle-unstable and were identified via their decay products.

The ^{6}He nucleus is a classical example of a Borromean system. The two-neutron separation energy of this nucleus equals to 0.972 MeV. According to the shell model, valence neutrons should occupy $p_{3/2}$ shell. However, three-body calculations predict contributions of $(s_{1/2})^2$ and $(p_{1/2})^2$ configurations with probabilities of 3 - 10% and 5 - 6%, respectively [77]. The presence of these components has been experimentally confirmed [78].

The binding energy of ^{8}He is 2.139(7) MeV [72]. It can be naively viewed as an α core surrounded by four valence neutrons, occupying the full $p_{3/2}$ subshell. However, experimental results contradict this picture [33, 79]. Theoretical calculations predict a contribution of the $(p_{3/2})^4$ configuration to the ground-state wave function of ^{8}He at a level of 35%, while the rest are admixtures of $(p_{3/2})^2(s_{1/2})^2$, $(p_{3/2})^2(d_{1/2})^2$ and $(p_{3/2})^2(p_{1/2})^2$ configurations [77]. It is obvious, that the situation with ^{9}He and ^{10}He is even more unclear.

7.2.1 ^{9}He

The ^{9}He nucleus was observed for the first time in the pion charge-exchange reaction $^{9}\mathrm{Be}(\pi^-, \pi^+)^{9}\mathrm{He}$. The spectrum, obtained in this experiment, was described by three resonances at energies of 1.14, 3 and 5 MeV [80]. A subsequent measurement confirmed these results and allowed to determine the widths of these states [81]. Further investigations [70, 82, 83] provided similar results. Therefore, for a long time the knowledge of the ground state of ^{9}He was considered to be well established. The resonance at an energy of about 1.2 MeV was interpreted as ground state of ^{9}He with a width $\Gamma \approx 0.1$ MeV. Measurements of neutron-fragment velocity difference in the two-proton knockout reaction $^{9}\mathrm{Be}(^{11}\mathrm{Be}, \mathrm{n}^{8}\mathrm{He})$ indicated the presence of virtual s-state with an upper limit

on the scattering length $a_s < -10$ fm [84]. The recent measurement provides a different value for the scattering length, $a_s > -20$ fm [85], with low statistics. An experiment with improved statistics provides a value for the scattering length between -2 and 0 fm [86]. Some of the experimental results for ^{9}He are presented in Table 7.1. All measurements but one are in agreement about the resonance states, while the situation for the low-energy part is unclear. A recent experiment shows a broad resonance at 2 MeV [85]. However, the reported energy resolution is about 0.8 MeV (FWHM) and the observed broad distribution can result from two overlapping resonances. The following analysis procedure concentrates mainly on a description of the low-energy part of the spectrum.

In the present experiment the relative-energy spectrum of ^{9}He is obtained by a coincident measurement of a ^{8}He fragment and a neutron after one-proton knockout from ^{11}Li at an energy of 280 MeV/nucleon. A similar result was obtained after proton knockout from ^{11}Li at an energy of 61 MeV/nucleon [76]. A comparison of the two spectra is shown in Fig. 7.3.

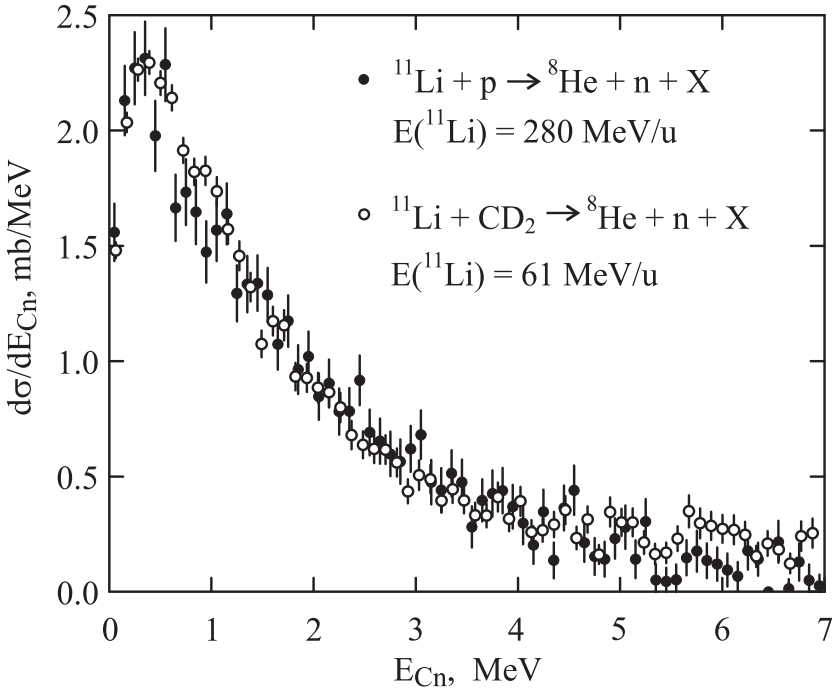

Figure 7.3: Comparison of the relative-energy spectra for ^{9}He obtained in the present experiment and after one-proton knockout from ^{11}Li at an energy of 61 MeV/nucleon [76]. The spectrum from Ref. [76] is normalized in the peak region to the spectrum obtained in the present experiment.

The analysis of ^{9}He data, described in Ref. [76], indicated that the low-energy part of the spectrum originates from the decay of ^{10}He and corresponds to

Table 7.1: Compilation of experimental results for $^{9}\mathrm{He}$. Most of them agree on resonances at energies of 1.2, 2.4, 4.3 and 5 MeV, while situation at the low-energy part of the spectrum is unclear.

Reaction	$^{9}\mathrm{Be}(\pi^-,\pi^+)$	$^{9}\mathrm{Be}(\pi^-,\pi^+)$	$^{9}\mathrm{Be}(^{14}\mathrm{C},^{14}\mathrm{O})$	$^{9}\mathrm{Be}(^{13}\mathrm{C},^{13}\mathrm{O})$	$^{9}\mathrm{Be}(^{14}\mathrm{C},^{14}\mathrm{O})$	$^{9}\mathrm{Be}(^{11}\mathrm{Be},\mathrm{n}^{8}\mathrm{He})$	$^{1}\mathrm{H}(^{11}\mathrm{Li},2\mathrm{pn})$
Ref.	[80]	[81]	[82]	[83]	[70]	[84]	[85]
a, fm	-	-	-	-	-	< -10	> -20
ϵ_{2n}, MeV	-	-	-	-	-		-
E_r, MeV	1.14(12)	1.13(10)	1.14(1.0)	1.8(6)	1.27(10)	-	2.0(2)
Γ, MeV	-	0.42(1)	1	-	0.10(6)	-	2
E_r, MeV	≈ 3	2.4	≈ 3	-	2.42(10)	-	-
Γ, MeV	-	0.42(1)	≈ 3	-	0.7(2)	-	-
E_r, MeV	-	-	-	-	4.30(10)	-	≥ 4.2
Γ, MeV	-	-	-	-	-	-	> 0.5
E_r, MeV	≈ 5	5.0	-	5.0	5.25(10)	-	-
Γ, MeV	-	0.5(1)	-	-	-	-	-

the case when one of the two neutrons is not detected. However, in the present analysis, such an interpretation is checked and rejected. The contribution from events, where two neutrons are crossing LAND but only one is detected, is estimated as described in Chapter 5 and subtracted, as shown in Fig. 7.4. The left panel of Fig. 7.4 shows the relative-energy spectrum for the ^{8}He + n system. The dashed line denotes the contribution of events originating from ^{10}He decay. The right panel of Fig. 7.4 shows the relative-energy spectrum for ^{8}He + n + n system. Here the background consists of events, where only one neutron was crossing LAND and the tracking routine misinterpreted it as two neutrons. In both cases, the corrections do not exceed 15% of the total amount of events.

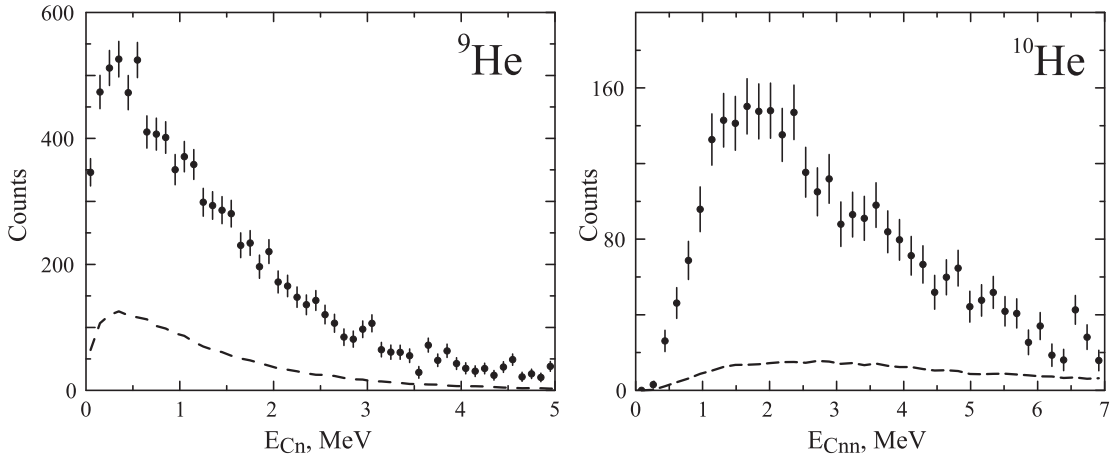

Figure 7.4: Relative-energy spectra for ^{9}He (left frame) and ^{10}He (right frame). Background, consisting of events with misinterpreted number of neutrons, is shown by dashed line.

Figure 7.5 shows the comparison of neutron transverse momentum distributions in cases, where one and two neutrons are detected in coincidence with ^{8}He. These distributions have different shapes because of different final-state interaction in the two-body and the three-body system. This is one more argument against an interpretation of the low-energy part of ^{9}He relative-energy spectrum as originating from ^{10}He decay, since in this case neutron momentum distributions would be similar.

The ground-state wave function of ^{11}Li contains 45(10)% of $(s_{1/2})^2$ neutrons [87]. Therefore, after quasi-free knockout of one proton from this nucleus, there is a high probability to obtain an s-wave neutron in the final state, which influences the low-energy part of the ^{9}He spectrum. (i) As a first attempt, the obtained relative-energy distribution is described as a single virtual state, using

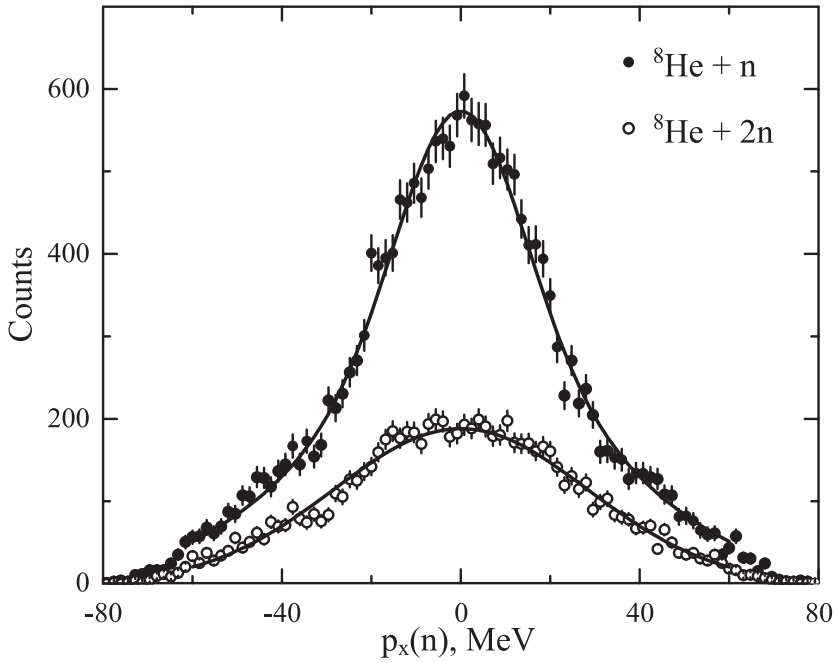

Figure 7.5: Neutron momentum distributions in ^{9}He and ^{10}He systems. The filled circles correspond to one-neutron events and open circles denote momentum distribution for one of the two neutrons. Different shapes of the spectra are determined by different final state interactions in two-body and three-body systems.

Eqs. 4.16 and 4.17. The result of the fit procedure is shown in Fig. 7.6. The obtained value for the scattering length is $a_s = -2.52(47)$ fm and the parameter $\epsilon_{2n} = 0.95(9)$ MeV, which is higher than expected. The achieved value for $\chi^2/n = 1.42$ allows to reject the hypothesis.

(ii) Guided by results of previous experiments, where two resonances were observed at energies of 1.2 and 2.4 MeV, with widths of 0.1 and 0.7 MeV [70], respectively, these two resonances were suggested to be present in the measured spectrum. However, since the statistics is low, not all parameters of the fit are varied and three of four parameters for two Breit-Wigner resonances are fixed, whereas the fourth parameter, namely the position of the first resonance is used as a free parameter in order to check the consistency of this approach. The obtained value for the position of the low-lying resonance $E_r = 1.33(8)$ MeV is in perfect agreement with previous experiments, which proves the consistency of the approach. The full result of the fit is shown in Fig. 7.7. Dotted and dashed-dotted lines correspond to Breit-Wigner resonances at energies of 1.33 and 2.4 MeV, respectively. The low-energy part of the spectrum is described

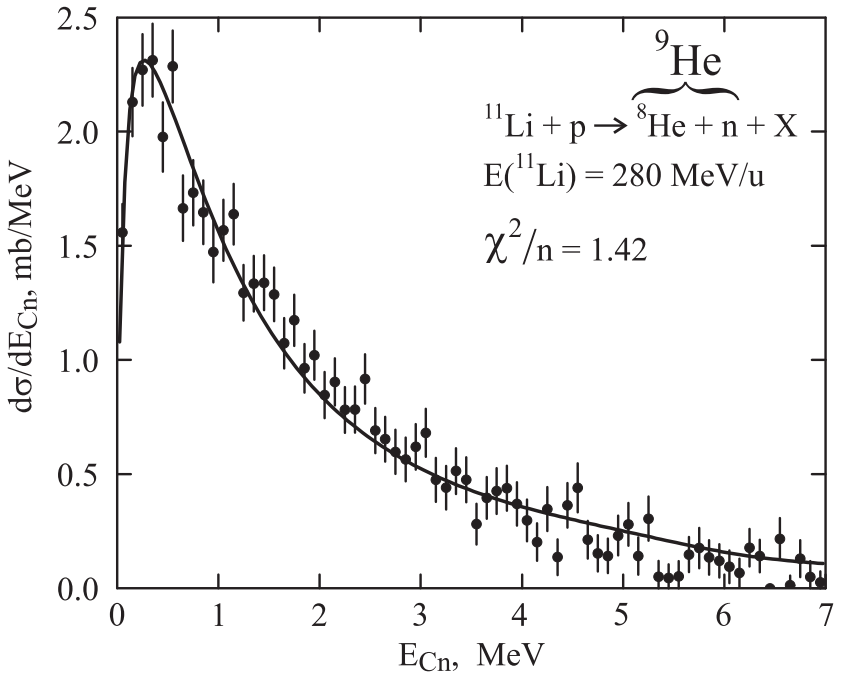

Figure 7.6: Differential cross section as a function of relative energy E_{Cn} for ^{9}He obtained after one-proton knockout from ^{11}Li, described as a single virtual s-state. The obtained value for scattering length is $a_s = -2.52(47)$ fm. The achieved value of $\chi^2/n = 1.42$ allows to reject the assumption.

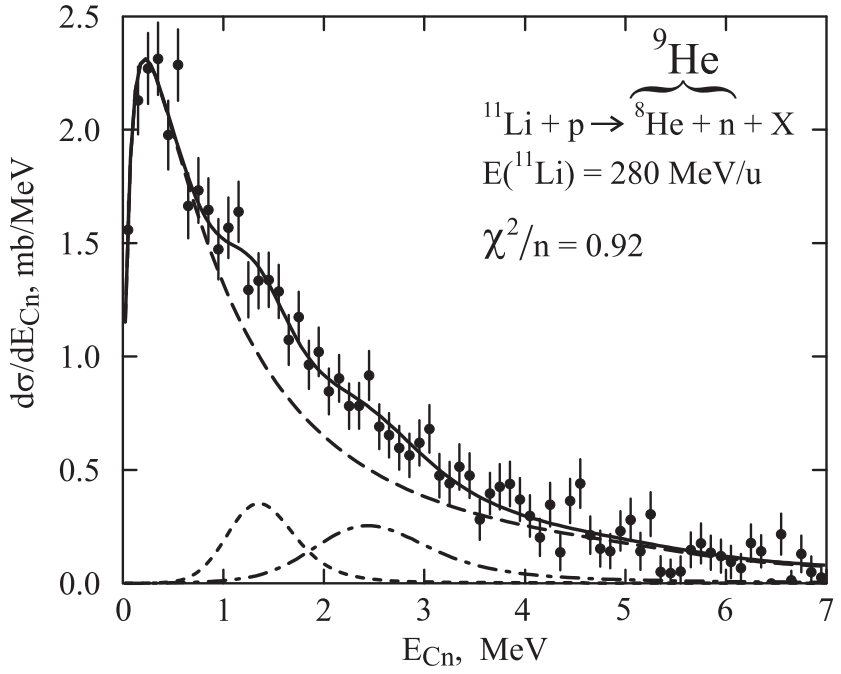

Figure 7.7: Differential cross section as a function of relative energy E_{Cn} for ^{9}He obtained after one-proton knockout from ^{11}Li. The dashed line shows virtual s-state with the scattering length $a_s = -3.16(78)$ fm, dotted and dash-dotted lines correspond to excited states at energies of 1.33 and 2.4 MeV, respectively.

as a virtual s-state using Eqs. 4.16 and 4.17 and is shown as dashed line. The obtained value for the scattering length is $a_s = -3.16(78)$ fm. The negative sign for the obtained scattering length a_s is in agreement with Refs. [84, 85], while its absolute value is much smaller. This is an indication of weaker interaction between ^{8}He and neutron within ^{9}He, than one would expect from the previous results. The obtained value for the parameter ϵ_{2n} is 0.79(10) MeV, which is higher than $S_{2n}(^{11}\mathrm{Li}) = 0.378$ MeV. The interpretation of the proton knockout data from ^{11}Li is more complicated, than for the proton knockout data from ^{14}Be. The break-up threshold of the ^{8}He fragment ($S_{2n} = 2.139(7)$ MeV) is much higher than the one of ^{11}Li and, therefore, it can still survive after momentum transfer and in this case the value of ϵ_{2n} becomes higher then it would be expected from the model.

It was mentioned above, that the shape of the spectrum, obtained using Eqs. 4.16 and 4.17 is not very sensitive to the effective range parameter r_0. In order to check this, the fit procedure was repeated with a value for the effective range parameter of $r_0 = 1.66$ fm. The obtained parameters $E_r = 1.35(9)$ MeV, $a_s = -3.56(84)$ fm and $\epsilon_{2n} = 0.90(13)$ MeV are within error bars in agreement with results obtained for $r_0 = 3$ fm. In both cases the values of the parameter ϵ_{2n} are much higher, than the known value for the two-neutron binding energy in ^{11}Li. The typical single-particle width for a p-wave resonance at an energy of about 1.2 MeV is about 2 MeV. Thus, a narrow resonance can be an indication for populating the *sd* shells.

7.2.2 ^{10}He

The heaviest known helium isotope is ^{10}He. The search for this nucleus has an almost 30 years history, since the first attempts in 1966 [88], until it was finally observed at RIKEN (Japan) by Korsheninnikov ***et al.*** in 1994 [76]. The invariant mass spectrum of ^{8}He + 2n system, produced in a d(^{11}Li, 2n^{8}He) reaction, shows a peak at an energy of 1.2(0.3) MeV and a width $\Gamma \leq 1.2$ MeV. This result was confirmed by following experiments [89, 90]. Excited states were observed at energies $E_r = 4.31(20)$ MeV and $E_r = 7.87(6)$ MeV. These results could not be reproduced by theory assuming ^{8}He with a $(p_{3/2})^4$ structure for the valence neutrons, the description has to be enhanced taking more complicated configurations into account [77].

The distribution of relative energy in the three-body ^{8}He + 2n system, obtained in the present experiment, is compared to the result of proton knockout

from ^{11}Li at an energy of 61 MeV/nucleon [76] in Fig. 7.8. The cross section is not calculated in Ref. [76] and the spectrum is normalized to the one obtained in the present experiment. The two spectra are similar within their uncertainties, despite different projectile energies and targets. This is an indication, that both of them reflect either the wave function of the initial nucleus, ^{11}Li, or the properties of the ^{10}He system. Figure 7.9 shows an attempt to describe the obtained spectrum by a correlated background calculated from the three-body wave function of ^{11}Li without considering any interaction between the reaction products in the final state

$$\frac{d\sigma}{dE_{Cnn}} \propto \frac{E_{Cnn}^2}{(1.87\epsilon_{2n} + E_{Cnn})^{7/2}}. \tag{7.2}$$

A similar approach was used in Ref. [76], involving the COSMA model [19] for the wave function calculation. The spectra, obtained with different assumptions, had their maxima above 5 MeV, while the experimental distribution peaks at 1 MeV. It was found, that a wrong asymptotics of the wave function has been used [91]. The problem is solved in the present analysis and the recalculated correlated background has a shape close to the experimental distribution. The used model cannot describe the spectrum at high energies, therefore the relative-energy range restricted to 0 - 5 MeV is used for the fit. As one can see from Fig. 7.9, the correlated background does not provide a proper description of the spectrum. The obtained result for the parameter $\epsilon_{2n} = 0.397(21)$ MeV is very close to the two-neutron separation energy in ^{11}Li, which equals to 0.378 MeV. It has been shown in the analysis of ^{9}He, that there is a momentum transfer to the fragment during the reaction, leading to a higher value of ϵ_{2n}. Therefore, another assumption is tested, namely to introduce a Breit-Wigner resonance in addition to the correlated background, as shown in Fig. 7.10. As a result, the new value $\epsilon_{2n} = 0.64(20)$ MeV is in agreement with the result of the ^{9}He analysis. The resonance parameters, $E_r = 1.42(10)$ MeV and $\Gamma = 1.04(76)$ MeV, are furthermore in good agreement with the results, reported in Ref. [76].

The observation of an excited state at the energy $E_r = 4.31(20)$ MeV [89] allows the alternative description of the measured spectrum as a superposition of two Breit-Wigner resonances without the correlated background involved, as shown in Fig. 7.11. In this case, the ground state has the parameters $E_r = 1.54(11)$ MeV and $\Gamma = 1.91(41)$ MeV and the excited state is found to be at the energy $E_r = 3.99(26)$ MeV with the width $\Gamma = 1.64(89)$ MeV.

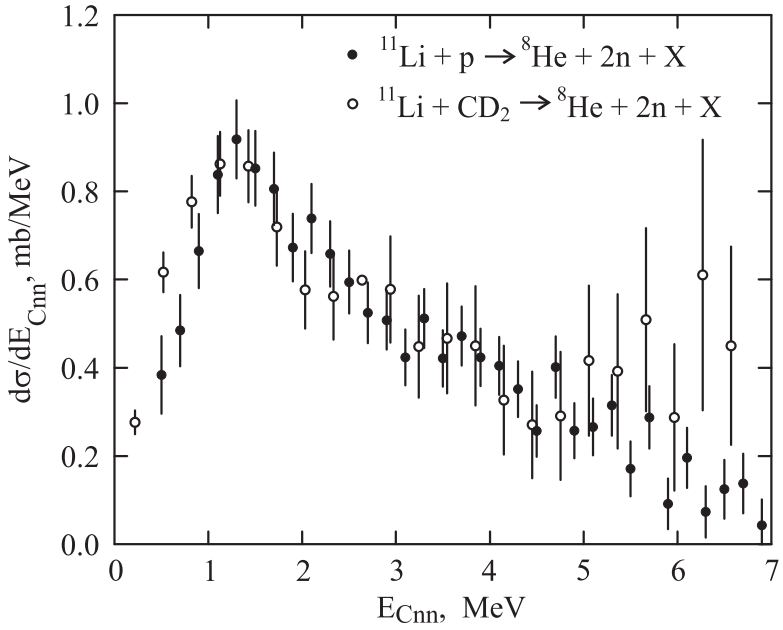

Figure 7.8: Comparison of the ^{10}He relative-energy spectra obtained after proton knockout from ^{11}Li at the energies of 61 MeV/nucleon (empty circles), obtained in RIKEN [76], and 280 MeV/nucleon (filled circles), obtained in the present experiment. The differential cross section as a function of the relative energy is calculated in the present work and the spectrum [76] is normalized at the peak region.

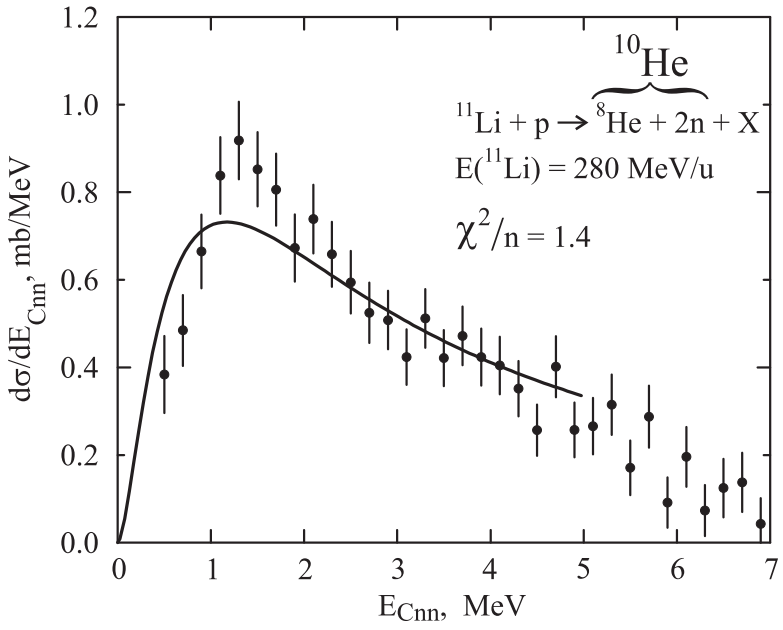

Figure 7.9: The description of the relative-energy distribution in the ^{10}He by the correlated background, calculated from the ^{11}Li wave function, without assuming any final-state interaction and any momentum transfer to the ^{8}He. The fit is restricted by relative energies 0 - 5 MeV, since the model does not describe high energy behavior of the spectrum.

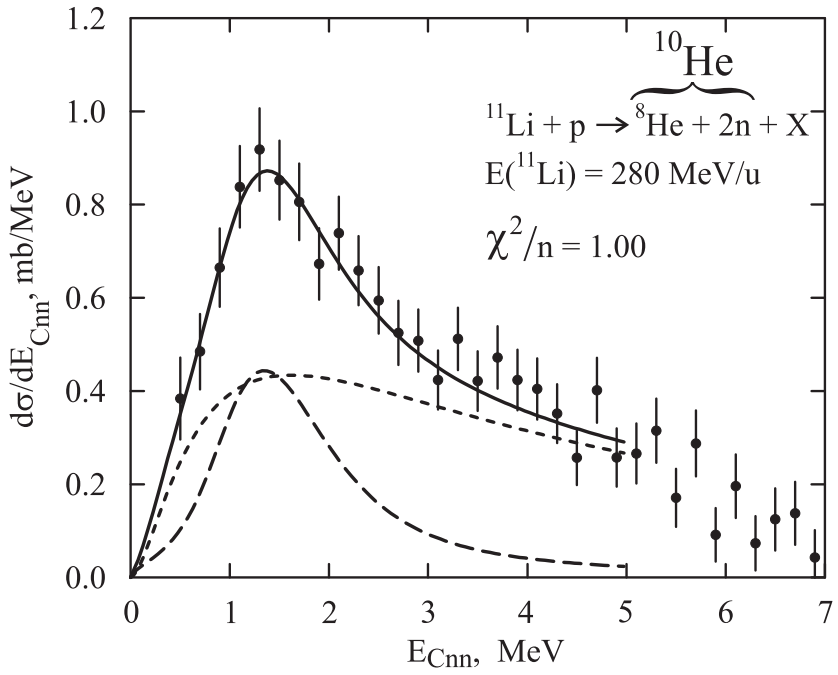

Figure 7.10: The description of the relative-energy spectrum by sum of correlated background (dotted line) and Breit-Wigner resonance (dashed line) at an energy of E_r = 1.42(10) MeV and a width Γ = 1.04(76) MeV.

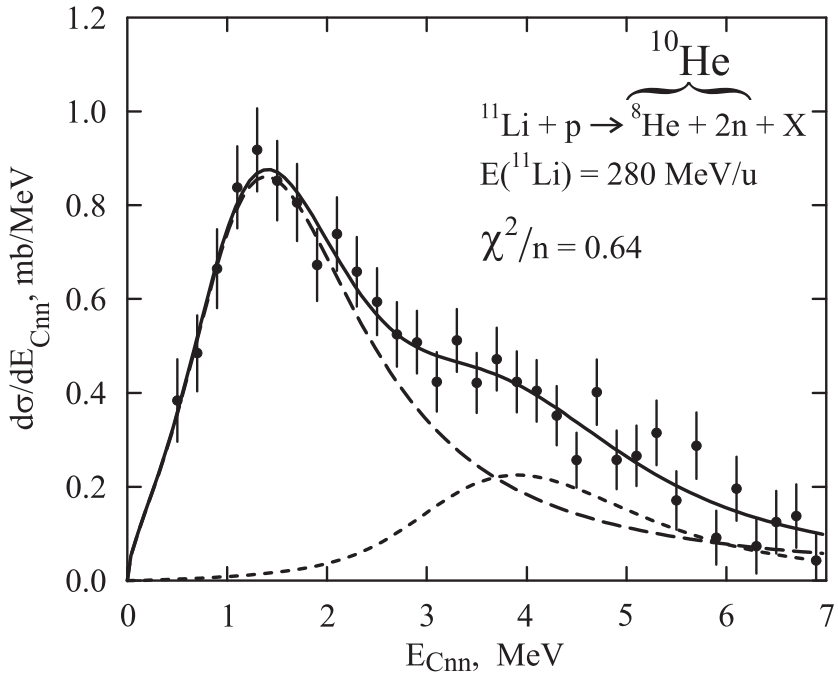

Figure 7.11: Differential cross section as a function of relative energy E_{Cnn} for ^{10}He obtained after one-proton knockout from ^{11}Li, described by two Breit-Wigner resonances at energies E_r = 1.54(11) MeV and E_r = 3.99(26) MeV with widths Γ = 1.91(41) MeV and Γ = 1.64(89) MeV, respectively.

Some theoretical calculations predict the ground state of ^{10}He with a $(s_{1/2})^2$ configuration [92, 93]. If it is the case, this resonance has to be accompanied by a virtual s-state in ^{9}He with a large value for the scattering length. This is not observed in the present experiment. Recent measurement showed an absence of any resonances below 2.5 MeV, however, the total statistics was very low [94].

The available experimental information about ^{10}He, including the present measurement, is summarized in Table 7.2. Both versions describing the spectrum agree with each other, and with other measurements. In the present measurement

Table 7.2: Compilation of available experimental results for ^{10}He including the present experiment.

Ref.	[76]	[89]	[90]	Present exp.	Present exp.
E_r^0, MeV	1.2(3)	1.07(7)	1.7(0.3)	1.42(10)	1.54(11)
Γ^0, MeV	$\leq$1.2	0.3(2)	-	1.04(76)	1.91(41)
E_r^1, MeV	-	4.31(20)	-	-	3.99(26)
Γ^1, MeV	-	1.0(3)	-	-	1.64(89)
E_r^2, MeV	-	7.87(6)	-	-	-
Γ^2, MeV	-	0.6(3)	-	-	-

and in the experiments presented in Refs. [76, 90] the initial nucleus was the same, ^{11}Li. It may be, that all spectra reflect only the initial nucleus wave function. This contradicts the result of an experiment, described in Ref. [89], where ^{10}Be was used as initial nucleus. The similarity of results obtained with different initial nuclei indicates strongly that they describe the properties of the ^{10}He system.

7.3 Virtual states

The phenomenon of neutron-nucleus s-wave scattering was described in Section 4.6 in terms of different theoretical approaches. The anti-bound states have been observed for several neutron-rich nuclei. In particular, in the present experiment they are observed in ^{9}He, ^{10}Li and ^{12}Li. Table 7.3 contains parameters for anti-bound states in these nuclei and also for ^{13}Be, for the three models. The parameters in R-matrix and S-matrix theory are calculated from the effective range parameters, which in turn are obtained from least-square fits of the data.

As one can see from the Table 7.3, the nuclei can be divided into two

Table 7.3: Comparison of parameters of virtual states in different nuclei, obtained in different theoretical approaches. The properties of the measured distributions, namely widths and positions of the maxima, are introduced for qualitative comparison of the data.

Nucleus	Spectrum		Effective range		R-matrix			S-matrix
	E_{max}, MeV	FWHM, MeV	a_s, fm	r_0, fm	E_r, MeV	Γ_r, MeV	λ	E_S, MeV
^{9}He	1.03	8.4	-3.17	3.00	4.97	24.6	1.2	-1.28
^{9}He	1.45	11.5	-3.55	1.66	8.05	46.5	1.4	-1.30
^{10}Li	0.037	0.52	-22.4	3.00	0.691	6.01	2.2	-0.041
^{12}Li	0.062	0.60	-13.7	3.00	0.379	2.02	1.3	-0.077
^{13}Be [68]	0.97	8.2	-3.2	3.00	4.74	23.5	1.2	-1.21

groups. Taking into account the experimental resolution and the influence of the prepared state, the relative-energy spectra for ^{10}Li and ^{12}Li peak at several tens keV with a FWHM of about 500 keV. In the effective-range approximation these nuclei are characterized by a large absolute value of the scattering length a_s. The R-matrix parameters for low-lying states in ^{10}Li and ^{12}Li nuclei correspond to the resonances below 1 MeV with several MeV width. The ^{9}He and ^{13}Be spectra are characterized by an extremely broad bump with a FWHM in the order of 10 MeV centered at about 1 MeV. The low-lying states in these nuclei are characterized by small absolute value of the scattering length in effective range approximation. In terms of the R-matrix theory it corresponds to resonance at several MeV with tens MeV width. Since in this case the R-matrix parameters are determined in a narrow region far from E_r, they have very large uncertainties for ^{9}He and depend strongly on the effective-range parameter r_0. However, this does not affect the position of the S-matrix pole, which is determined from E_r and Γ_r of the R-matrix approach.

From the position of E_r one can conclude, that the anti-bound states observed in ^{9}He and ^{13}Be cannot be interpreted as ground states, but rather a threshold phenomenon. In the case of ^{10}Li the obtained R-matrix resonance energy is $E_r = 0.691$ MeV. Taking into account, that the first resonance state is observed at $E_r = 0.57$ MeV, the interpretation of the virtual s-state as ground state can also be doubted.

7.4 Angular and energy correlations

From the relative-energy spectra at most positions and widths of the resonances are extracted. In order to understand the observed systems, further knowledge of their internal structure is needed. This information can be extracted from correlations between decay products. Angular and energy correlations for the three-body ^{8}He + 2n and ^{11}Li + 2n systems are studied at the region of their ground states, $0 < E_{Cnn} < 3$ MeV, using the hyperspherical harmonics (HH) formalism, described in detail in Section 4.4 and Appendix B.

For each three-body system four correlation plots are obtained – projections of the correlation function $W(\varepsilon, \theta)$ to the energy and angular axis in T and Y Jacobi coordinate systems. The obtained distributions for ^{8}He + 2n and ^{11}Li + 2n systems are shown in Figs. 7.12 and 7.13, respectively. The partial energy ε is defined as $\varepsilon = E_{nn}/E_{Cnn}$ in the T-system and in this case the distribution $W(\varepsilon)$ characterizes the energy correlations between the two neutrons. In the Y-system $\varepsilon = E_{Cn}/E_{Cnn}$ and $W(\varepsilon)$ describes the energy correlations between the core fragment and one of the neutrons. An uncorrelated energy distribution in the system is described by the phase space $W(\varepsilon) \propto \sqrt{\varepsilon(1-\varepsilon)}$, which is shown as dashed line in all fractional energy spectra. If the mean relative energy between two particles (n - n or core - n) peaks at small values, the corresponding spectrum is enhanced compared to the phase space at low ε, while a shift towards high ε indicates preferably high relative energies.

In the analysis of the two-neutron events neutrons are sorted by velocity. Since two neutrons are identical, it is impossible to determine the sign of $\cos\theta$ in the T-system and this requires the distribution to be symmetric. Therefore, angular distribution is calculated twice, with fast neutron being the first and slow neutron being the second, and vice versa. The summation of these two mirrored spectra leads to symmetry of the final distribution.

If one compares the relative-energy spectra of ^{10}He and ^{13}Li (see Figs. 7.2 and 7.10), the resonance structure is more pronounced in the former case, while the distribution is very broad in the latter case. The situation with the correlation plots seems to be different. There are practically no correlations between constituents of ^{10}He. The obtained angular distribution in the T-system is uniform, as shown in the lower left panel of Fig. 7.12 and energy in the Y-system is distributed according to phase space, as shown in the upper right panel of

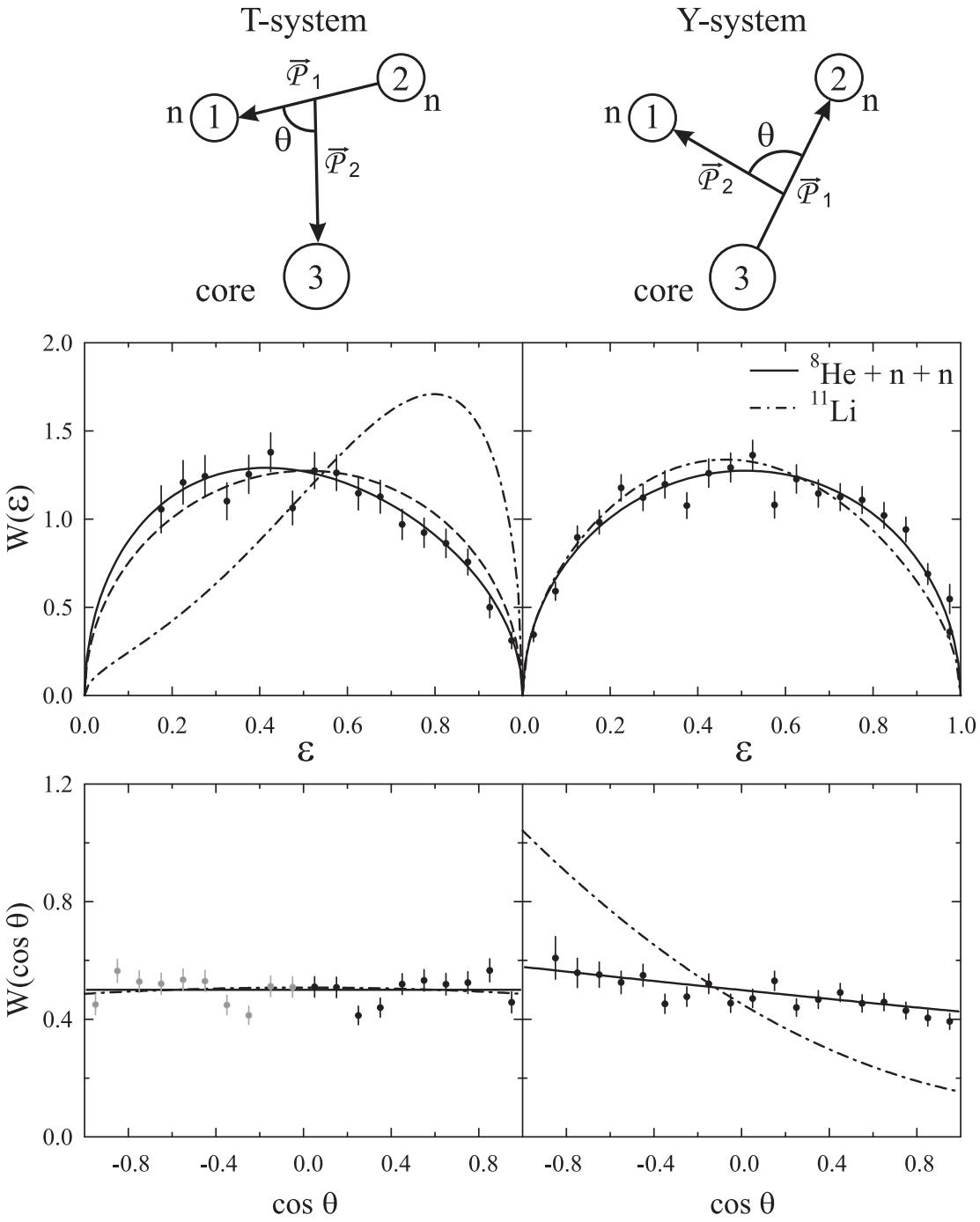

Figure 7.12: Energy (upper panels) and angular (lower panels) correlations in $^8\mathrm{He} + 2\mathrm{n}$ system in the region of the ground state, $0 < E_{Cnn} < 3$ MeV. The distributions in the T-system are shown in the left panels and the distributions in the Y-system are shown in the right panels. The angular distribution in the T-system is symmetric because of equivalence of two neutrons. Results of a fit are shown by solid line. The dashed line represents a phase-space distribution. Correlations, obtained from the ground-state wave function of $^{11}\mathrm{Li}$ assuming no final-state interaction [95] are shown by the dash-dotted line.

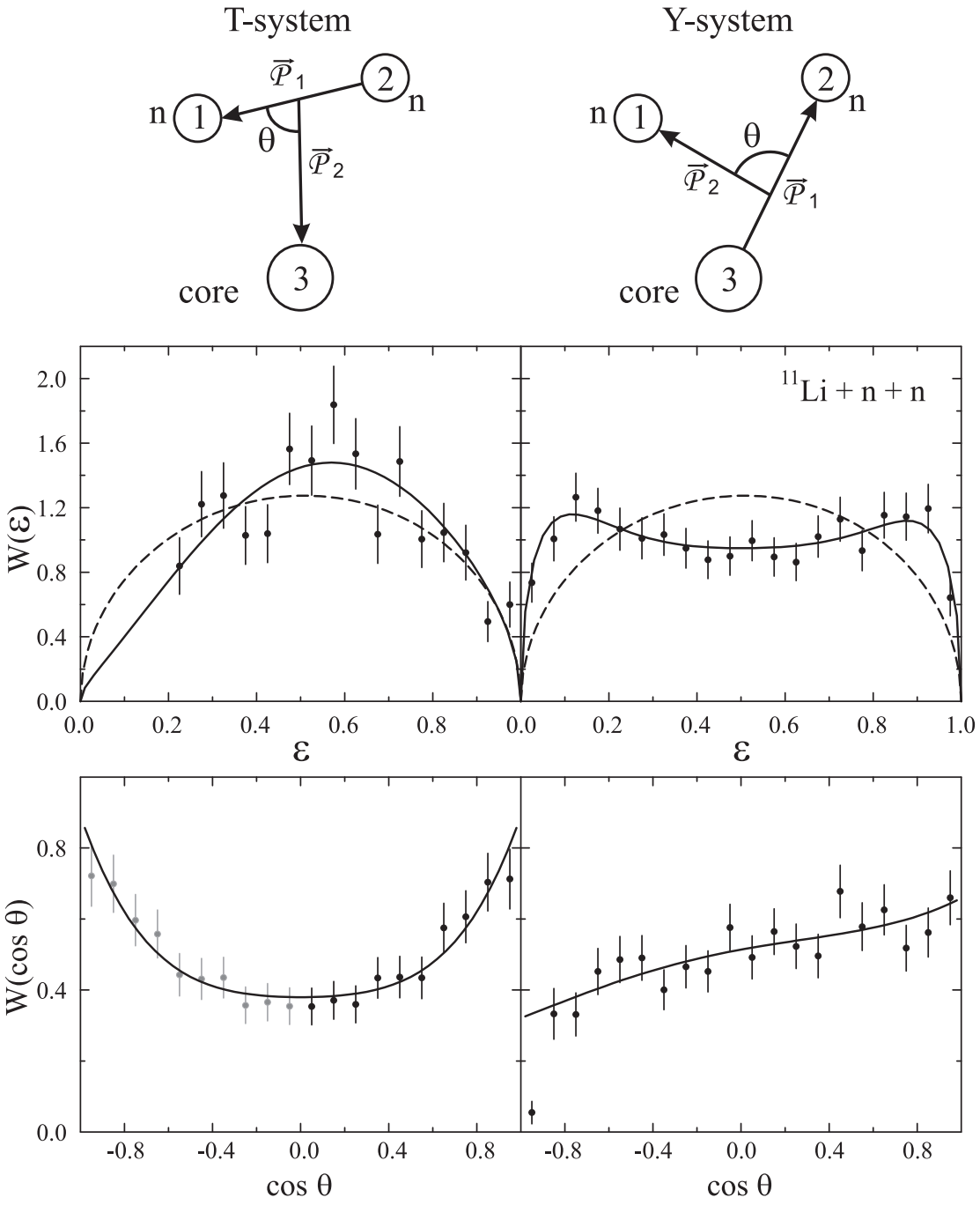

Figure 7.13: Energy (upper panels) and angular (lower panels) correlations in $^{11}\mathrm{Li} + 2\mathrm{n}$ system in the region of ground state, $0 < E_{Cnn} < 3$ MeV. The distributions in the T-system are shown in the left panels and the distributions in the Y-system are shown in the right panels. The angular distribution in the T-system is symmetric because of equivalence of two neutrons. Solid line corresponds to the results of the fit. Dashed line denotes phase-space distribution.

Fig. 7.12. These two spectra indicate the absence of any interaction between the fragment and the neutrons. The shape of the energy distribution in the T-system, which is shifted towards low ε, reveals correlations between the energies of the neutrons. The same effect is reflected in the angular distribution in the Y-system, which is enhanced at the region of low θ, as shown in the lower right panel of Fig. 7.12.

In contrast to the case of ^{8}He + 2n, the correlation plots indicate strong interaction in the ^{11}Li + 2n system. The energy distribution in Y-system exhibits a double-hump structure. The low-energy hump corresponds to strong energy correlations of core fragment and one of the neutrons. This agrees with the result for ^{12}Li, where a strong attraction between the ^{11}Li core and neutron is observed. If the relative energy between the core and one neutron is low, consequently the relative energy between the core fragment and the second neutron is high. Since the two neutrons are equivalent, the second hump appears at high energies, which corresponds to anticorrelation between the core and the second neutron. The same feature is reflected in the angular distribution in T-system. Low values of θ correspond to the case, where the neutron and the core fragment are close in the momentum space, while high values of θ are achieved when relative energy between the core fragment and the neutron is large. For the given total energy in the system, if the relative energy between the core fragment and one of the neutrons is small, then, consequently, the relative energy between the two neutrons is high. This results in an energy distribution in the T-system, which indicates anticorrelation of neutron energies, as shown in the upper left panel of Fig. 7.13 and reflected in the angular distribution in Y-system, which reveals predominantly large angles between the Jacobi momenta $\vec{\mathcal{P}}_1$ and $\vec{\mathcal{P}}_2$.

For the analysis of the obtained spectra the spin-parity $J^\pi = 0^+$ was assumed for the ^{10}He ground state and a similar structure was considered for ^{13}Li. A full set of HH with $K = 0,\ 2,\ 4$; $l_1, l_2 = 0,\ 1,\ 2$ and $S = 0,\ 1$ was tested on the distributions in the T-system and restricted to the necessary components. The antisymmetrization of the wave function with respect to the two neutrons in the T-system results in even values of l_1 for $S = 0$ and odd values for $S = 1$. The

correlation function in the T-system can be written as

$$
\begin{aligned}
W(\theta,\varepsilon) =& \frac{4}{\pi}\sqrt{\varepsilon(1-\varepsilon)}\Big\{|A_{00}^{00}|^2 + 4|A_{00}^{20}|^2(1-2\varepsilon)^2 \\
&+ 8|A_{11}^{20}|^2(1-\varepsilon)\varepsilon\sin^2\theta + 32|A_{22}^{40}|^2(\varepsilon-1)^2\varepsilon^2(3\cos^2\theta-1)^2 \\
&+ 16\sqrt{2}|A_{00}^{20}||A_{22}^{40}|\cos(\varphi_{00}^{20}-\varphi_{22}^{40})(2\varepsilon-1)(\varepsilon-1)\varepsilon(3\cos^2\theta-1) \\
&+ 2|A_{00}^{00}|\Big[|A_{00}^{20}|\cos\varphi_{00}^{20}(2-4\varepsilon) \\
&+ 4\sqrt{2}|A_{22}^{40}|\cos\varphi_{22}^{40}(1-\varepsilon)\varepsilon(3\cos^2\theta-1)\Big]\Big\}
\end{aligned}
\tag{7.3}
$$

,

where the complex amplitudes have to satisfy the condition

$$|A_{00}^{00}|^2 + |A_{00}^{20}|^2 + |A_{11}^{20}|^2 + |A_{22}^{40}|^2 = 1. \tag{7.4}$$

The phases $\varphi_{l_1 l_2}^{KL}$ are calculated relative to the φ_{00}^{00}. All four spectra are fitted with one set of parameters. Transformation of the parameters between T and Y systems is performed using Raynal-Revai coefficients (see Eq. 4.11). Results of the fit are shown by the solid line in the spectra. The obtained coefficients are shown in Table 7.4.

Table 7.4: Coefficients obtained from the fit of energy and angular correlations between the decay products of ^{10}He and ^{13}Li nuclei in T-system. All phases are calculated relative to φ_{00}^{00}.

Nucleus	$KLSl_1l_2$	$\lvert A_{l_1l_2}^{KL}\rvert^2$	$\varphi_{l_1l_2}^{KL}$, deg.
^{10}He	$K=2,\ L=0,\ S=0,\ l_1=0,\ l_2=0$	0.23(11)	0.70(42)
^{13}Li	$K=2,\ L=0,\ S=0,\ l_1=0,\ l_2=0$	1.2(5)	178(27)
	$K=2,\ L=0,\ S=1,\ l_1=1,\ l_2=1$	33.1(5)	
	$K=4,\ L=0,\ S=0,\ l_1=2,\ l_2=2$	6.7(1.1)	0.4(20.)

It is found, that distributions in the ^{8}He + 2n system are determined mainly by the harmonic with $K = 0$. Weak correlations are observed and explained by a contribution of $K = 2$ at a level of only 0.23(11)%. Several interpretations for the ^{10}He relative-energy spectrum are presented in Section 7.2.2. The study of correlations helps to choose the more reasonable interpretation. In case there is no final-state interaction in the ^{8}He + 2n system, the measured distributions should

reflect the ones, obtained from ^{11}Li wave function [95]. The theoretical curves are shown by dash-dotted lines in Fig. 7.12. The experimental data look very different, which can be explained by the fact, that the initial distributions are altered by final state interaction. Taking into account this information, one can conclude, that the most reasonable interpretation of the ^{10}He relative-energy spectrum is using two Breit-Wigner resonances, without any correlated background involved. The observed faint correlations between the decay products of the ^{10}He ground state, indicate a more complicated structure of the nucleus, than consisting of a ^{8}He core surrounded by two valence neutrons.

In order to describe the correlation spectra for the ^{13}Li system, higher harmonics have to be involved. The contribution of the lowest harmonic with $K = 0$ is found to be 59%. The harmonics with $K = 2$ is present with $l_1 = l_2 = 0$ and $l_1 = l_2 = 1$ at the levels of 1.2(5)% and 33.1(5)% respectively. Strong correlations in the system are explained mainly by an appearance of $K = 4$ harmonics at a level of 6.7(1.1)%. The theoretical description based on the wave function of the initial nucleus, ^{14}Be, is still missing. In the future, it would be useful to have it in order to compare to the measured distributions and to estimate the validity of the correlation background approach to the description of the ^{13}Li spectrum.

All coefficients in Eq. 7.3 are determined from fits to the experimental data. Thus, the two-dimensional correlation function $W(\varepsilon, \theta)$ can be reconstructed. Figure 7.14 shows the functions in the T-system, describing the correlations between the decay products of ^{10}He (left panel) and ^{13}Li (right panel) nuclei.

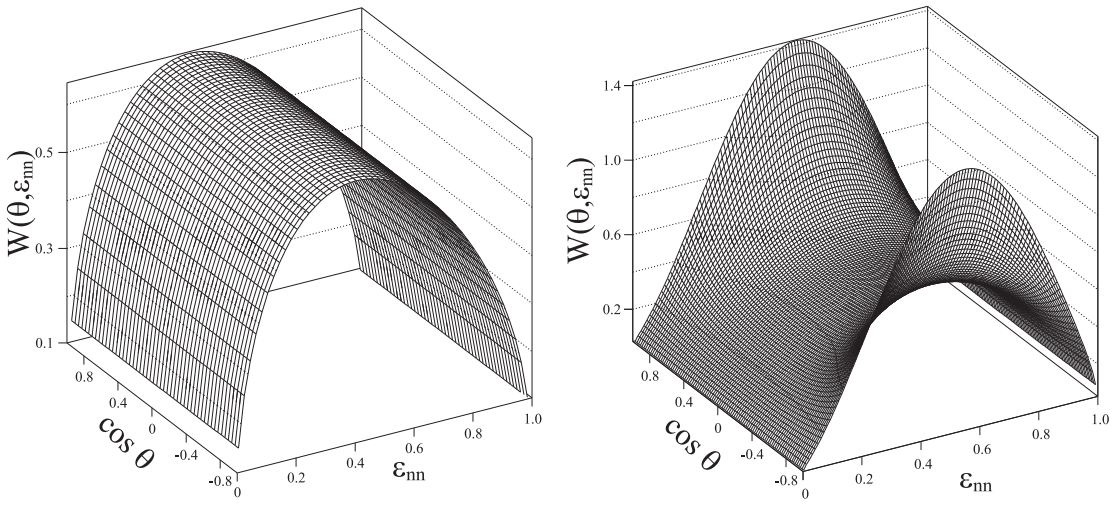

Figure 7.14: Correlation functions $W(\varepsilon, \theta)$ for ^{10}He (left panel) and ^{13}Li (right panel) in the T-system.

8. Summary and outlook

The unbound nuclear systems ^{9}He, ^{10}He, ^{10}Li, ^{12}Li and ^{13}Li have been studied using proton-induced nucleon knockout in inverse kinematics using relativistic ^{8}He, ^{11}Li and ^{14}Be projectiles.

The isotope ^{10}Li was produced in one-neutron knockout reaction from the halo nucleus ^{11}Li. The obtained relative-energy spectrum is described by a low-lying virtual s-state with the scattering length $a_s = -22.4(4.8)$ fm and a p-wave resonance with $E_r = 0.566(14)$ MeV and $\Gamma = 0.548(30)$ MeV, which is in good agreement with previous experimental results.

The isotopes ^{12}Li and ^{13}Li are observed for the first time. They are produced in a one-proton knockout reaction from ^{14}Be. The ^{11}Li isotopes were detected in coincidence with one or two neutrons. The obtained invariant-mass spectrum of ^{12}Li is described as a single virtual s-state with a scattering length $a_s = -13.7(1.6)$ fm. The spectrum of ^{13}Li is interpreted as a resonance at an energy of $E_r = 1.47(13)$ MeV with a width $\Gamma \approx 2$ MeV, superimposed on a broad correlated background distribution.

The detection of ^{8}He in coincidence with one or two neutrons, after proton knockout from ^{11}Li, allows the reconstruction of the relative-energy spectra for the heaviest helium isotopes, ^{9}He and ^{10}He. The low-energy part of the ^{9}He spectrum is dominated by a virtual s-state with the scattering length $a_s = -3.16(78)$ fm. An evidence for two resonance states with $l \neq 0$ in ^{9}He at energies of 1.33(8) and 2.4 MeV is also obtained. Several interpretations can be used to describe the ^{10}He spectrum. It can be seen as (i) a superposition of narrow resonance at $E_r = 1.42(10)$ MeV with $\Gamma = 1.04(76)$ MeV and broad correlated background distribution. Alternatively, the spectrum can be interpreted using two resonances (ii) at energies of 1.54(11) and 3.99(26) MeV with widths of 1.91(41) MeV and 1.64(89) MeV, respectively.

In addition, a study of three-body correlations in the decay of ^{10}He and ^{13}Li systems in the region of the relative energy 0 - 3 MeV is performed. No strong correlations are observed in $^{8}\mathrm{He}+2\mathrm{n}$ system. However, the obtained distributions are very different from what one would expect in case if there is no final-state interaction in the system, which favours the second (ii) interpretation above. The system $^{11}\mathrm{Li}+2\mathrm{n}$ reveals strong correlations between the constituents. In this case it is necessary to have theoretical calculations based on ^{14}Be wave function in

assumption of no final-state interaction. It is very important for understanding of the ^{13}Li structure. The interpretation of angular and energy correlations in ^{10}He and ^{13}Li systems in the region of relative energy 3 - 7 MeV has to be performed. In this region relative-energy spectrum in the case of ^{13}Li is mainly described by a parametrization for the correlated background. Two possibilities exist for ^{10}He. Combination of experimental distributions and theoretical calculations in this region will provide information about excited states in ^{13}Li, if there are any, and additional arguments for any of the two interpretations of ^{10}He spectrum.

In future, with the R^{3}B setup [42], experimental technique will be improved drastically. Higher beam intensity together with upgraded detector design will permit measurements with better statistics and resolution. Kinematically complete detection of all reaction products including recoil protons will provide the full information about the reaction process. In the present experiment we can only estimate the role of momentum transfer to the core fragment, while in future it will be possible to investigate the process in detail.

9. Zusammenfassung

Die ungebundenen Kernsysteme ^{9}He, ^{10}He, ^{10}Li, ^{12}Li und ^{13}Li wurden mittels protoneninduziertem Nukleonenaufbruch aus relativistischen Strahlen, bestehend aus ^{8}He, ^{11}Li und ^{14}Be mit Energien von 240, 280 bzw. 305 MeV/Nukleon hergestellt und in inverser Kinematik untersucht. Hohe Strahlenergien führen zu kurzen Wechselwirkungszeiten bei kleinen Streuwinkeln, so dass vereinfachte Näherungen für die Beschreibung des Reaktionsmechanismus möglich sind. Aus experimenteller Sicht sind große Strahlgeschwindigkeiten für eine starke kinematische Fokussierung verantwortlich, die Messungen unter Abdeckung des volles Raumwinkels mit mäßig großen Detektoren bei einer hohen Nachweis-Effizienz erlaubt.

Das Experiment wurde an der GSI (Darmstadt) durchgeführt. Der Experimentieraufbau ist in Abb. 9.1 gezeigt. Er besteht aus dem Neutronendetektor LAND, aus dem Dipol-Spektrometer ALADIN und aus verschiedenen Arten von Tracking-Detektoren. Die Hauptaufgabe des Detektorsystems ist die Rekonstruk-

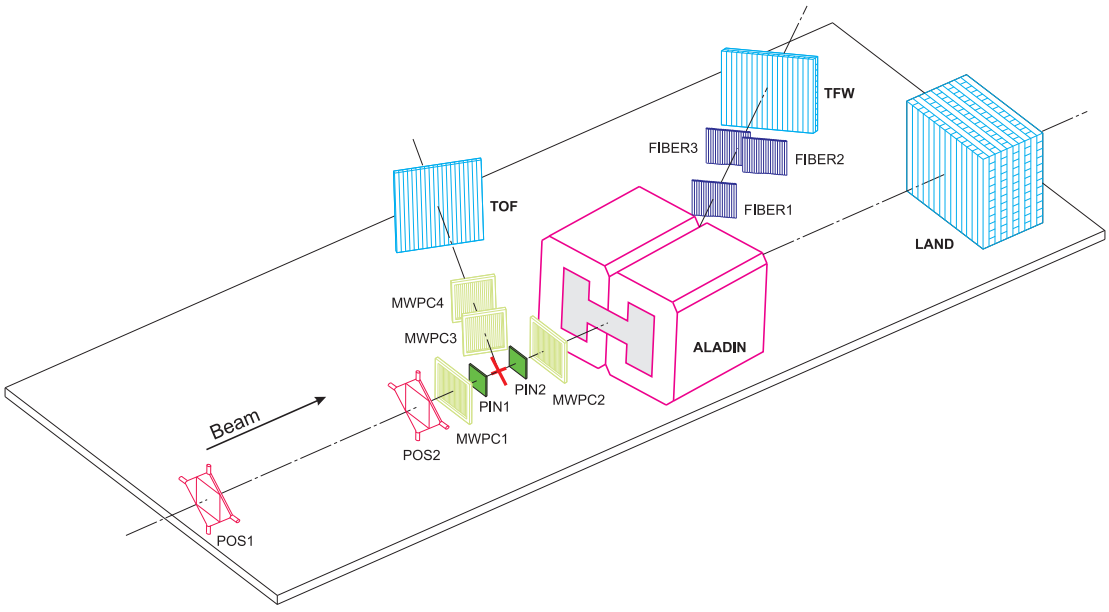

Abbildung 9.1: Schema des experimentellen Aufbaus: Aufgrund der kinematischen Strahlfokussierung ermöglicht die Anordnung kinematisch vollständige Messungen aller Reaktionsprodukte mit Detektoren, die nur einen kleinen Teil des gesamten Raumwinkels im Laborsystem abdecken. POS – POsition Sensitive scintillator, PIN – p-i-n diode, MWPC – Multi-Wire Proportional Chamber, ALADIN – A LArge gap DIpole magNet, LAND – Large Area Neutron Detector, TFW – Time of Flight Wall, TOF – Time Of Flight wall.

tion des Vierer-Impulses der Reaktionsprodukte mit hoher Auflösung. Der Experimentieraufbau umfasst Detektoren mit komplexer Struktur, z.B. der LAND-Detektor besteht aus 200 unabhängigen Szintillatoren, die beidseitig mit Photomultipliern ausgelesen werden. Um die gewünschte Auflösung zu erreichen, müssen alle Detektoren untereinander kalibriert und zeitlich synchronisiert werden. Die grundlegenden Kalibrierungsverfahren sind automatisch und ermöglichen nicht nur die Berechnung einer Reihe von Kalibrierungparametern, sondern auch die Untersuchung von deren Stabilität während des Experiments und wenn nötig, eine Einführung von zeitabhängigen Korrekturen. Im vorliegenden Experiment wurde eine zeitabhängige Kalibrierung für die meisten der Detektoren durchgeführt.

Neutronen-/Protonen-Aufbruchreaktionen führen u.a. zur Bildung von ungebundenen Systemen, die unmittelbar Zerfallen. Die Eigenschaften von neutronenreichen ungebundenen Kernen werden sowohl durch Rekonstruktion der Relativenenergiespektren als auch durch die Untersuchung der Winkelkorrelationen zwischen den Reaktionsprodukten studiert. In den Relativenergiespektren werden Position und Breite der auftretenden Resonanzen extrahiert. Die Korrelationen zwischen den Reaktionsprodukten beinhalten Informationen über die Struktur der beobachteten Kernsysteme.

Im Falle des Neutronenaufbruchs, bedingt durch hohe Strahlenergie und die Tatsache, dass Halo-Neutronen schwach gebunden und die meiste Zeit außerhalb des Kernrumpfs lokalisiert sind, verhält sich dieser als "Zuschauer". Im Gegensatz zu Neutronen sind Protonen stark im Kern gebunden. Die Separationsenergie eines Protons in neutronenreichen Kernen ist etwa 20 MeV. Daher ist es nicht einfach, ein Proton aus dem Kern ohne Auswirkungen auf den Rest des Systems zu entfernen, und die Möglichkeit eines Impulsübertrags auf den Restkern muss berücksichtigt werden.

Im Falle des Protonenaufbruchs werden ein modifiziertes Kernfragment und zwei Neutronen im Endzustand produziert. Wenn eines der Neutronen einen transversalen Impuls größer als 60 MeV hat, wird der LAND-Detektor nicht getroffen. Die Wechselwirkung dieses Neutrons mit dem System, das aus dem Restkern und dem anderen Neutron besteht, wird als vernachlässigbar beschrieben. Im Folgenden werde diese Ereignisse als "Ein-Neutron-Event" bezeichnet. Eine spezielle Tracking-Routine wird für die Trennung mehrerer Neutronentreffer verwendet. Mit einer gewissen Wahrscheinlichkeit ermittelt diese Routine eine nicht korrekte Anzahl von Neutronentreffern. Daher wird bei der Analyse der exper-

imentellen Daten das Verhalten der Tracking-Routine mit einer Monte-Carlo-Simulation berechnet. Die Simulation basiert auf den experimentellen Daten und ermöglicht die Bestimmung eines so genannten "gefälschten" Neutronenuntergrundes und die Durchfürung einer Korrektur.

Leichte, schwach gebundene Kerne zeichnen sich durch einen hohen Grad an Cluster-Bildung aus. Somit entstehen die Teilchen im Endzustand (Restkern und schwerere Fragmente) nicht in der Reaktion. Sie werden als bereits von Anfang an im Projektil-Kern bestehend beschrieben und werden durch den Zusammenstoß nur freigesetzt. Dementsprechend ist die Relativenenergie-Verteilung der Aufbruchfragmente durch die Wellenfunktion des Anfangszustandes, modifiziert durch die Endzustandswechselwirkung, definiert. Die bevölkerten Resonanzen werden in der Regel in Rahmen der R-Matrix-Theorie [49] beschrieben, die die ursprüngliche Verteilung nicht berücksichtigt. Die erhaltenen Spektren werden durch eine Breit-Wigner-Parametrisierung der Resonanzen mit der Resonanzenergie E_r und der Resonanzbreite Γ als freien Parametern beschrieben. Dieser Ansatz kann im Falle starker Wechselwirkung zwischen Restkern und Neutronen angewendet werden. Beim Überschreiten der Neutronen-Abbruchkante, wo die Neutronenzahl die Anzahl der Protonen stark überschreitet, kann sich die Situation ändern. Wenn man sich auf der "terra incognita" befindet, muss geprüft werden, ob das erhaltene Spektrum nicht nur durch die Eigenschaften des Anfangkernes entstanden ist. Nur wenn dies nicht der Fall ist, kann auf die Existenz eines Resonanzzustandes zurückgeschlossen werden.

Im Falle einer kurzlebigen niedrigliegenden Resonanz kann die Breite Γ größer als E_r sein und damit Resonanz kann mit der Schwelle überlappen. Da an der Schwelle der Aufbruchquerschnitt verschwinden muss, wird die Form der Resonanz asymmetrisch. Im Fall von tiefliegenden s-Resonanzen ist $\Gamma(E) \propto E^{1/2}$, deshalb überlappen sie typischerweise mit der Schwelle. Im Extremfall $\Gamma > 4E_r$ wird der Zustand als "virtuell"bezeichnet und kann in Rahmen der sogenannten "effective range theory" mit den Parametern: Streulänge a_s und in diesem Fall [51] der Zwei-Neutronenseparationsenergie des Projektil-Kernes, ϵ_{2n} beschrieben werden.

Eine der ersten je entdeckten Halokern ist ^{11}Li. Er ist bis heute eines der anschaulichsten Beispiele für dieses Phänomen. Sein ungebundenes Subsystem ^{10}Li wird via Ein-Neutronenaufbruch produziert, wobei das Aufbruchwechselwirkende Halo-Neutron zu großen Winkeln gestreut wird. Der Nachweis von

^{9}Li-Fragmenten in Koinzidenz mit dem verbleibenden Neutron ermöglicht die Rekonstruktion des Relativenenergiespektrums des ungebundenen ^{10}Li. Die erhaltene Verteilung wird durch einen tiefliegenden virtuellen s-Zustand mit der Streulänge $a_s = -22.4(4.8)$ fm und einer p-Resonanz mit $E_r = 0.566(14)$ MeV und $\Gamma = 0.548(30)$ MeV beschrieben, was in guter Übereinstimmung mit früheren experimentellen Ergebnissen ist. Der aus dem Fit extrahierte Wert für die Zwei-Neutronenseparationsenergie des Projektil-Kerns, $\epsilon_{2n} = 0.352(22)$ MeV, liegt in der Nähe der Bindungsenergie von ^{11}Li bei 0.375(5) MeV. Diese Tatsache bestätigt die Annahme, dass sich verbleibende ^{10}Li-System als Zuschauer verhält.

Die Isotope ^{12}Li und ^{13}Li wurden hier zum ersten Mal beobachtet. Sie wurden in den Aufbruchreaktionen ^{1}H(^{14}Be, 2pn)^{12}Li und ^{1}H(^{14}Be, 2p)^{13}Li erzeugt. Das Isotop ^{11}Li wurde in Koinzidenz mit einem oder zwei Neutronen nachgewiesen. Die Bindungsenergie von ^{11}Li ist mit 0.376 MeV niedrig, es würde im Falle eines signifikanten Impulsübertrages während der Reaktion aufbrechen. Das heißt, dass bei dem Protonenaufbruch von ^{14}Be das Restsystem im wesentlichen unbeeinflusst bleibt.

Das erhaltene Relativenenergiespektrum von ^{12}Li wird als ein einzelner virtueller s-Zustand mit einer Streulänge von $a_s = -13.7(1.6)$ fm gut beschrieben. Die Bindungsenergie des Projektil-Kerns ^{14}Be wird ebenfalls gut reproduziert. Der aus dem Fit extrahierte Wert für den Parameter $\epsilon_{2n} = 1.47(19)$ MeV stimmt mit der bekannten Separationsenergie von 1.26(13) MeV gut überein.

Die breite Relativenenergie-Verteilung von ^{13}Li kann nicht als korrelierter Untergrund beschrieben werden. Dieser berechnet sich aus der Wellenfunktion des Ausgangskernes ^{14}Be mit Annahme, dass keine Endzustandswechselwirkung stattfindet. Daher wurde dem korrelierten Untergrund eine Resonanz bei einer Energie von $E_r = 1.47(13)$ MeV mit einer Breite von $\Gamma \sim 2$ MeV superponiert. Es kann auch nicht ausgeschlossen werden, dass das Spektrum eine Überlagerung mehreren Resonanzen repräsentiert. Für eine sichere Aussage sind weiterreichende experimentelle Untersuchungen notwendig.

Der Nachweis von ^{8}He in Koinzidenz mit einem oder zwei Neutronen nach dem Protonenaufbruch von ^{11}Li ermöglicht die Rekonstruktion der Relativenenergiespektren für die schwersten Helium-Isotope, ^{9}He and ^{10}He. Die Interpretation der Daten bei Entfernung eines Protons von ^{11}Li ist komplizierter als im Falle des ^{14}Be. Die Aufbruchsschwelle des ^{8}He-Fragments liegt viel höher ($S_{2n} = 2.14$ MeV) als in ^{11}Li, deshalb kann der Kern einen signifikanten Impulsübertrag überleben.

Dieser Effekt muss während der Datenanalyse berücksichtigt werden.

Für ^{9}He wurden Resonanzen mit Energien von etwa 1.2, 2.4, 4.3 und 5 MeV in mehreren Experimenten beobachtet. Die Situation im niederenergetischen Teil des Spektrums ist ungeklärt. Verschiedene Experimente liefern Werte für die Streulänge zwischen -20 fm und 0 fm [84–86]. Im vorliegenden Experiment wird der niederenergetische Teil des ^{9}He-Spektrums durch einen virtuellen s-Zustand mit der Streulänge $a_s = -3.16(78)$ fm dominiert. Der erhaltene Wert für die Zwei-Neutronenbindungsenergie, $\epsilon_{2n} = 0.79(10)$ MeV, ist höher als der bekannte Wert für ^{11}Li. Dies ist wahrscheinlich durch den Impulsübertrag auf das ^{8}He-Fragment während der Reaktion bedingt. Ein Hinweis auf zwei Resonanzen mit $l \neq 0$ in ^{9}He bei Energien von 1.33(8) und 2.4 MeV wird in diesem Experiment gesehen, in Übereinstimmung mit früheren Messungen.

Der Kern ^{10}He ist das schwerste bekannte Helium-Isotop. Die Suche nach diesem Kern hat eine fast 30-jährige Geschichte, von den ersten Versuchen im Jahr 1966 [88] bis zur Beobachtung bei RIKEN (Japan) durch Korsheninnikov *et al.* im Jahr 1994 [76]. Trotzdem ist die experimentelle Information über ^{10}He heute immer noch sehr fragmentarisch und basiert auf nur drei Messungen [76, 89, 90]. Im vorliegenden Experiment wurden mehrere Interpretationen zur Beschreibung des ^{10}He-Spektrums benutzt. Es kann nicht durch eine korrelierten Untergrund beschrieben werden, der aus der Wellenfunktion von ^{11}Li unter vernachlässigung der Endzustandswechselwirkung bestimmt wird. Eine gute Beschreibung wird durch eine Überlagerung einer schmalen Resonanz bei einer Energie von $E_r = 1.42(10)$ MeV mit einer Breite von $\Gamma = 1.04(76)$ MeV und einer breiten Verteilung des korrelierten Untergrundes erreicht (i). Die Beobachtung eines angeregten Zustandes bei einer Energie von $E_r = 4.31(20)$ MeV [89] ermöglicht eine alternative Beschreibung des gemessenen Spektrums als Überlagerung von zwei Breit-Wigner-Resonanzen (ii) ohne den korrelierten Untergrund. In diesem Fall werden die Resonanzen bei Energien von 1.54(11) und 3.99(26) MeV mit den Breiten 1.91(41) MeV bzw. 1.64(89) MeV beobachtet.

Bei der Untersuchung von Systemen mit mehr als zwei Komponenten erweist sich die Analyse der verschiedenen Arten von Energie- und Winkelkorrelationen zwischen den Clustern als reiche Informationsquelle. Die Expansion der partiellen Energie- und Winkelverteilungen in hyperspherische Harmonische Funktionen bietet ein praktisches Werkzeug für deren Studium. Diese Methode wurde

zum ersten Mal für die Analyse von Kernreaktionen in Ref. [45, 46] eingesetzt. Sie wurde vor kurzem für die Untersuchung der elektromagnetischen Aufspaltung des borromäischen Kerns ^{6}He angewendet [47].

In der vorliegenden Arbeit wurden Dreikörper-Korrelationen beim Zerfall von ^{10}He- und ^{13}Li-Systemen in der Region ihrer Grundzustände, die einem Relativenenergie-Intervall von 0 - 3 MeV entsprechen, untersucht. Es wurden keine starken Korrelationen im System ^{8}He + 2n gefunden. Die gewonnenen Verteilungen unterscheiden sich sehr stark von denen, die man im Fall fehlender Endzustandswechselwirkung erwarten würde. Das ist ein Hinweis auf die Tatsache, dass Ausgangsverteilung hier durch die Endzustandswechselwirkung im ^{8}He + 2n System modifiziert wird. Dies spricht für die bereits angesprochene Interpretation (ii), die ohne korrelierten Untergrund die Spektren beschreibt. Das System ^{11}Li + 2n zeigt eine starke Korrelation zwischen den Komponenten. In diesem Fall sind theoretische Rechnungen, basierend auf der ^{14}Be-Wellenfunktion ohne Berücksichtigung der Endzustandswechselwirkung, für das Verständnis der Struktur von ^{13}Li notwendig. Die Interpretation der Winkel- und Energiekorrelationen in den Systemen ^{10}He und ^{13}Li im Bereich einer Relativenenergie von 3 - 7 MeV muss noch durchgeführt werden. In diesem Energiebereich werden die Relativenenergiespektren im Fall von ^{13}Li vor allem durch den korrelierten Untergrund beschrieben. Es gibt zwei Möglichkeiten für das ^{10}He-System. Im Energie-Intervall von 3 - 7 MeV wird das Spektrum entweder (i) mit Hilfe des berechneten korrelierten Untergrundes oder (ii) einer Breit-Wigner parametrisierten Resonanzstruktur beschrieben. Die Kombination von experimentellen Verteilungen und theoretischen Rechnungen in dieser Region werden Informationen über die angeregten Zustände in ^{13}Li, wenn es welche gibt, und zusätzliche Argumente für eine der beiden Interpretationen des ^{10}He-Spektrums liefern.

Die logische Fortentwicklung des jetzigen LAND-Experiments ist das an FAIR geplante R^{3}B-Experiment [42]. Höhere Strahlintensitäten zusammen mit einem optimierten Design aller Detektoren werden Messungen mit verbesserter Statistik und genauerer Auflösung ermöglichen. Die kinematisch vollständige Erfassung aller Reaktionsprodukte zusammen mit den Rückstoß-Protonen aus dem Target wird komplette Informationen über den Reaktionsprozess liefern. Im vorliegenden Experiment kann die Rolle des Impulsübertrages auf das Kern-Fragment bestimmt werden, während es in Zukunft möglich sein wird, den gesamten Prozess im Detail zu untersuchen.

A. Jacobi coordinates

For the description of three-body systems (core + n + n) it is convenient to use a set of translation invariant coordinates $\{\vec{\mathcal{R}}_1, \vec{\mathcal{R}}_2\}$, also known as Jacobi coordinates, where $\vec{\mathcal{R}}_i = \{\mathcal{R}_i, \hat{\mathcal{R}}_i\}$. Here $\mathcal{R}_i$ is the length and $\hat{\mathcal{R}}_i$ are the angular coordinates of the vector $\vec{\mathcal{R}}_i$.

If $\vec{r}_i$, $\vec{r}_j$ and $\vec{r}_l$ are individual cluster coordinates, then Jacobi coordinates for a three-body system can be written as

$$\begin{cases} \vec{\mathcal{R}}_1 = \vec{r_i} - \vec{r_j} \\ \vec{\mathcal{R}}_2 = \vec{r_l} - \dfrac{m_i\vec{r_i} + m_j\vec{r_j}}{m_i + m_j}, \\ \vec{\mathcal{R}}_{cm} = \dfrac{m_i\vec{r_i} + m_j\vec{r_j} + m_l\vec{r_l}}{m_i + m_j + m_l} \end{cases} \tag{A.1}$$

where $(ijl) = (123)$ corresponds to a so called T-system and $(ijl) = (231)$ to Y-system, defined in Fig. A.1.

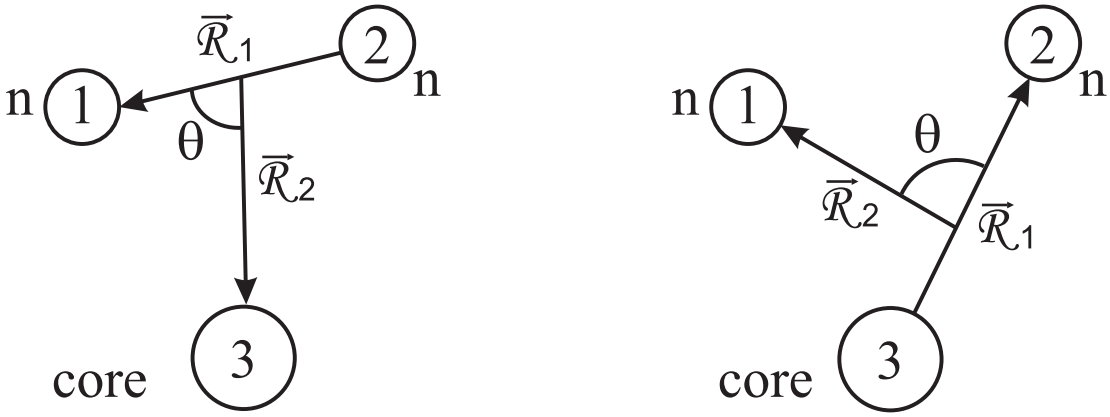

Figure A.1: Definitions of T (left) and Y (right) Jacobi coordinate systems.

One may define the conjugated momenta corresponding to the Jacobi coordinates $\vec{\mathcal{R}}_1$, $\vec{\mathcal{R}}_2$ and $\vec{\mathcal{R}}_{cm}$. These corresponding momenta, denoted as $\vec{\mathcal{P}}_1$, $\vec{\mathcal{P}}_2$ and $\vec{\mathcal{P}}_{cm}$, can be expressed via individual cluster momenta $\vec{p_i}$, $\vec{p_j}$ and $\vec{p_l}$. The conjugated momentum $\vec{\mathcal{P}}_1$ corresponding to the Jacobi coordinate $\vec{\mathcal{R}}_1$ is defined as

$$\vec{\mathcal{P}}_1 = M_1 \frac{d\vec{\mathcal{R}}_1}{dt}, \tag{A.2}$$

where M_1 is the reduced mass of the two particles connected by the Jacobi vector $\vec{\mathcal{R}}_1$. Thus, applying Eq. A.2 to Eq. A.1 one obtains the conjugated momenta

$$\begin{cases} \vec{\mathcal{P}}_1 = \left(\dfrac{\vec{p_i}}{m_i} - \dfrac{\vec{p_j}}{m_j} \right) \dfrac{m_i m_j}{m_i + m_j} \\ \vec{\mathcal{P}}_2 = \left(\dfrac{\vec{p_l}}{m_l} - \dfrac{\vec{p_i} + \vec{p_j}}{m_i + m_j} \right) \dfrac{m_l (m_i + m_j)}{m_i + m_j + m_l}. \\ \vec{\mathcal{P}}_{cm} = \vec{p_i} + \vec{p_j} + \vec{p_l} \end{cases} \tag{A.3}$$

In analogy to coordinate space, in momentum space one can introduce variables

$$\kappa \equiv \sqrt{\vec{\mathcal{P}_1}^{\,2} + \vec{\mathcal{P}_2}^{\,2}} \qquad \text{and} \qquad \theta_\kappa \equiv \arctan \frac{\mathcal{P}_1}{\mathcal{P}_2}, \qquad \theta_\kappa \in \left[0, \frac{\pi}{2} \right]. \tag{A.4}$$

The "momentum" κ is connected to the total relative energy of the three-body system and the hyperangle θ_κ is responsible for the energy distribution between the clusters. The application of the Jacobi coordinates is described in Section 4.4.

B. Hyperspherical harmonics

The hyperspherical harmonics (HH) method for the description of three-body systems is a generalization of the commonly used approach for description of two-body systems. The two-body system in spherical coordinates is described by the set of variables $\{r, \hat{r}\}$, where $\hat{r} \equiv \{\theta, \phi\}$. The kinetic energy operator is defined as

$$\hat{T}^2 = -\frac{\hbar^2}{2m}\nabla^2_{\vec{r}} = -\frac{\hbar^2}{2m}\left[\frac{1}{r^2}\frac{\partial}{\partial r}\left(r^2\frac{\partial}{\partial r}\right) - \frac{1}{r^2}\hat{L}^2(\hat{r})\right], \tag{B.1}$$

where $\hat{L}$ is the orbital angular momentum operator, describing angular part of the two-body motion. The eigenfunctions of $\hat{L}$ are the spherical harmonics $Y_{lm}(\hat{r})$. The eigenvalue of operator $\hat{L}^2$ is $l(l+1)$ which results in eigenvalue equation

$$\hat{L}^2 Y_{lm}(\hat{r}) = l(l+1)Y_{lm}(\hat{r}). \tag{B.2}$$

A three-body system can be described by the set of Jacobi coordinates $\{\vec{\mathcal{R}}_1, \vec{\mathcal{R}}_2\}$, defined in Appendix A. In the context of the HH method, the wave function describing the three-body system is expressed as a function of the hyperspherical coordinates $\{\rho, \theta_\rho, \hat{\mathcal{R}}_1, \hat{\mathcal{R}}_2\}$. The hyperradius ρ is given by

$$\rho \equiv \sqrt{\mathcal{R}_1^2 + \mathcal{R}_2^2}, \tag{B.3}$$

where

$$\mathcal{R}_1 = \rho \sin\theta_\rho \qquad \text{and} \qquad \mathcal{R}_2 = \rho\cos\theta_\rho, \tag{B.4}$$

and hyperangle θ_ρ is defined by

$$\theta_\rho \equiv \arctan\frac{\mathcal{R}_1}{\mathcal{R}_2}, \qquad \theta_\rho \in \left[0, \frac{\pi}{2}\right]. \tag{B.5}$$

The remaining four angles $\{\hat{\mathcal{R}}_1, \hat{\mathcal{R}}_2\} = \{\theta_1, \phi_1, \theta_2, \phi_2\}$ are the common angular coordinates of Jacobi vectors $\vec{\mathcal{R}}_1$ and $\vec{\mathcal{R}}_2$.

In terms of hyperspherical coordinates the kinetic energy operator for a three-body system becomes

$$\hat{T}^2 = -\frac{\hbar^2}{2m}(\nabla^2_{\vec{\mathcal{R}}_1} + \nabla^2_{\vec{\mathcal{R}}_2}) = -\frac{\hbar^2}{2m}\left(\frac{\partial^2}{\partial\rho^2} + \frac{5}{\rho}\frac{\partial}{\partial\rho} - \frac{1}{\rho^2}\hat{K}^2(\Omega_5^\rho)\right), \tag{B.6}$$

where $\Omega_5^\rho \equiv \{\theta_\rho, \theta_1, \phi_1, \theta_2, \phi_2\}$ and $\hat{K}^2(\Omega_5^\rho)$ is the hypermomentum operator describing the angular and hyperangular parts of the three-body motion defined as

$$\hat{K}^2(\Omega_5^\rho) = -\frac{\partial^2}{\partial\theta_\rho^2} - 4\cot(2\theta_\rho)\frac{\partial}{\partial\theta_\rho} + \frac{\hat{L}^2(\hat{\mathcal{R}}_1)}{\sin^2\theta_\rho} + \frac{\hat{L}^2(\hat{\mathcal{R}}_2)}{\cos^2\theta_\rho} \tag{B.7}$$

The eigenfunctions of the hypermomentum operator are the hyperspherical harmonics, which describe the distribution of the clusters in the three-body system

$$\Gamma^{l_1 l_2}_{KLM_L}(\Omega_5^\rho) = \Psi^{l_1 l_2}_K(\theta_\rho) Y^{l_1 l_2}_{LM_L}(\hat{\mathcal{R}}_1, \hat{\mathcal{R}}_2). \tag{B.8}$$

Here $\Psi^{l_1 l_2}_K(\theta_\rho)$ are the hyperangular functions and $Y^{l_1 l_2}_{LM_L}(\hat{\mathcal{R}}_1, \hat{\mathcal{R}}_2)$ spherical harmonics. The corresponding eigenvalues of the operator $\hat{K}$ are defined by the eigenvalue equation

$$\hat{K}^2 \Gamma^{l_1 l_2}_{KLM_L} = K(K+4)\Gamma^{l_1 l_2}_{KLM_L}, \tag{B.9}$$

where K is called the hypermomentum. This quantum number is a generalization of the normal angular momentum and is given by

$$K = l_1 + l_2 + 2\nu \qquad \text{with} \qquad \nu = 0, 1, 2, \ldots . \tag{B.10}$$

The quantum number $l_1(l_2)$ is the relative orbital angular momentum between the clusters separated by Jacobi vector $\vec{\mathcal{R}}_1(\vec{\mathcal{R}_2})$.

The hyperangular part of the hyperspherical harmonics is the hyperangular function

$$\Psi^{l_1 l_2}_K(\theta_\rho) = N^{l_1 l_2}_K (\sin\theta_\rho)^{l_1} (\cos\theta_\rho)^{l_2} P_\nu^{l_1+1/2, l_2+1/2}(\cos 2\theta_\rho), \tag{B.11}$$

where $N^{l_1 l_2}_K$ is a normalization coefficient

$$N^{l_1 l_2}_K = \left[\frac{\nu!(K+2)(\nu+l_1+l_2+2)!}{2^{l_1+l_2+2}\Gamma(\nu+l_1+\frac{3}{2})\Gamma(\nu+l_2+\frac{3}{2})}\right]^{1/2} \tag{B.12}$$

and $P_\nu^{l_1+1/2, l_2+1/2}(\cos 2\theta_\rho)$ the Jacobi polynomial

$$P_\nu^{\alpha,\beta}(x) = 2^{-\nu}\sum_{k=0}^{\nu}\begin{pmatrix} \nu+\alpha \\ k \end{pmatrix}\begin{pmatrix} \nu+\beta \\ \nu-k \end{pmatrix}(x-1)^{\nu-k}(x+1)^k. \tag{B.13}$$

The normalization conditions for the hyperangular functions are

$$\int_0^{\pi/2} d\theta_\rho \sin^2\theta_\rho \cos^2\theta_\rho \Psi^{l_1 l_2}_K(\theta_\rho)\Psi^{l_1 l_2}_{K'}(\theta_\rho) = \delta_{KK'}. \tag{B.14}$$

The angular part is expressed in terms of spherical harmonics as

$$Y^{l_1 l_2}_{LM_L}(\hat{\mathcal{R}}_1, \hat{\mathcal{R}}_2) = \sum_{m_{l_1}=-l_1}^{l_1} \sum_{m_{l_2}=-l_2}^{l_2} Y_{l_1 m_{l_1}}(\theta_1, \phi_1) Y_{l_2 m_{l_2}}(\theta_2, \phi_2) \times C^{LM_L}_{l_1 m_{l_1} l_2 m_{l_2}}, \quad \text{(B.15)}$$

where $C^{LM_L}_{l_1 m_{l_1} l_2 m_{l_2}}$ are Clebsch-Gordan coefficients. The spherical harmonics are the eigenfunctions of the angular momentum operator $\hat{L}^2$ and can be explicitly written as

$$Y_{l m_l}(\theta, \phi) = \sqrt{\frac{(2l+1)(l-m_l)!}{4\pi(l+m_l)!}} P_l^{m_l}(\cos\theta) e^{i m_l \phi}, \quad \text{(B.16)}$$

where $P_l^{m_l}$ are the associated Legendre polynomials. The normalization and orthogonality relation of the angular functions is given by

$$\int_0^{2\pi} d\phi \int_0^{\pi} d\theta \sin\theta Y^*_{l m_l}(\theta, \phi) Y_{l' m'_l}(\theta, \phi) = \delta_{l l'} \delta_{m_l m'_l}. \quad \text{(B.17)}$$

C. Correlated background

As was mentioned above, three-body systems can be described by a set of hyperspherical coordinates $\{\rho, \theta_\rho, \hat{\mathcal{R}}_1, \hat{\mathcal{R}}_2\}$ and the wave function can therefore be expanded in HH:

$$\Psi_{JM}(\vec{\mathcal{R}}_1, \vec{\mathcal{R}}_2) = \rho^{-5/2} \sum_{KLSl_1l_2} \chi^{l_1l_2}_{KLS}(\rho) \left[\Gamma^{l_1l_2}_{KL}(\Omega^\rho_5) \otimes \theta_{SM_S}\right], \tag{C.1}$$

where $\Gamma^{l_1l_2}_{KL}(\Omega^\rho_5)$ is the HH, θ_{SM_S} the spin function. For Borromean systems, the hyperradial functions χ in Eq. C.1 behave asymptotically as

$$\chi^{l_1l_2}_{KLS}(\rho) \sim exp(-\kappa_0\rho) \qquad \text{for} \qquad \rho \to \infty, \tag{C.2}$$

where κ_0 is connected to the binding energy via $E_0 = (\hbar\kappa_0)^2/(2m)$ and m is the nucleon mass. Since such asymptotic behavior is the same for all terms in the expansion one can choose a simple bound-state wave function

$$\chi^{l_1l_2}_{KLS}(\rho) = a^{l_1l_2}_{KLS}\chi^{(2)}(\rho), \tag{C.3}$$

where

$$\chi^{(2)}(\rho) \equiv c[exp(-\kappa_0\rho) - exp(-\kappa_1\rho)] \tag{C.4}$$

with

$$c = \sqrt{\frac{2\kappa_0\kappa_1(\kappa_0+\kappa_1)}{(\kappa_0-\kappa_1)^2}} \qquad \text{and} \qquad \sum |a^{l_1l_2}_{KLS}|^2 = 1. \tag{C.5}$$

This two-parameter hyperradial wave function reproduces simultaneously the true asymptotic behavior of the bound-state wave function and size of the system. The parameters κ_0 and κ_1 are defined using experimental values for binding energy and RMS matter radius, respectively.

For a three-body system the distribution of momenta is given by

$$\frac{d^6N}{d\vec{\mathcal{P}}_1 d\vec{\mathcal{P}}_2} \propto |\Psi_0(\vec{\mathcal{P}}_1, \vec{\mathcal{P}}_2)|^2, \tag{C.6}$$

where $\vec{\mathcal{P}}_1$ and $\vec{\mathcal{P}}_2$ are the conjugated Jacobi momenta.

If $\vec{p}_1$, $\vec{p}_2$ and $\vec{p}_3$ are momenta of particles with masses m_1, m_2 and m_3, respectively, then the relative energy of the three-body system is given by

$$E_{Cnn} = \frac{\hbar^2}{2m}\left(\frac{p_1^2}{m_1} + \frac{p_2^2}{m_2} + \frac{p_3^2}{m_3}\right) = \frac{\hbar^2}{2m}(\mathcal{P}_1^2 + \mathcal{P}_2^2) = \frac{\hbar^2}{2m}\kappa^2, \tag{C.7}$$

where value κ is introduced similar to the hyperradius, $\kappa = \sqrt{\mathcal{P}_1^2 + \mathcal{P}_2^2}$. Thus, the six-dimensional volume element can thus be written as

$$d\vec{\mathcal{P}}_1 d\vec{\mathcal{P}}_2 = \kappa^2 d\kappa d\Omega_5^\kappa \propto E_{Cnn}^2 dE_{Cnn} d\Omega_5^\kappa, \tag{C.8}$$

which indicates the possibility to obtain the distribution of relative energy, $\frac{dN}{dE_{Cnn}}$, from the momentum-space wave function by performing an integration over the five hyperspherical angles (Ω_5^κ).

Using the model wave function from Eq. C.4 the Fourier transform and the hyperspherical angular integration can be performed analytically. Introducing $E_i = \hbar^2\kappa_i^2/(2m)$ (i = 0,1) in Eq. C.4, one obtains

$$\frac{dN}{dE_{Cnn}} \propto \sum_K A_K |F_K(E_{Cnn})|^2, \tag{C.9}$$

where

$$A_K = \sum_{LSl_1l_2} |a_{KLS}^{l_1l_2}|^2 \tag{C.10}$$

and

$$F_K(E_{Cnn}) \propto E_{Cnn}^{-3/4} \frac{\Gamma(K+7/2)}{2^K\Gamma(K+3)}\left[f_K\left(\frac{E_{Cnn}}{E_0+E_{Cnn}}\right) - f_K\left(\frac{E_{Cnn}}{E_1+E_{Cnn}}\right)\right], \tag{C.11}$$

where $\Gamma(x)$ is the gamma function and the function $f_K(y)$ is defined as

$$f_K(y) = y^{(2K+7)/4}{}_2F_1\left(\frac{2K+7}{4}, \frac{2K+3}{4}, K+3, y\right) \tag{C.12}$$

with ${}_2F_1(\alpha,\beta,\gamma,y)$ being the hypergeometric function.

Bibliography

[1] Evaluated Nuclear Structure Data File, http://www.nndc.bnl.gov/ensdf/.

[2] H. Grave, M. Lewitowicz, Nucl. Phys. **A 693** (2001) 116.

[3] P.E. Haustein (ed.), At. Data Nucl. Tables **39** (1988) 39.

[4] W.A. Friedman, G.F. Bertsch, Phys. Rev. **C 76** (2007) 057301.

[5] T. Otsuka, R. Fujimoto, Y. Utsuno, B.A. Brown, M. Honma, T. Mizusaki, Phys. Rev. Lett. **87** (2001) 082502.

[6] G.C. Ball, S. Bishop, J.A. Behr, G.C. Boisvert, P. Bricault, J. Cerny, J.M. D'Auria, M. Dombsky, J.C. Hardy, V. Iacob, J.R. Leslie, T. Lindner, J.A. Macdonald, H.-B. Mak, D.M. Moltz, J. Powell, G. Savard, I.S. Towner, Phys. Rev. Lett. **86** (2001) 8.

[7] N. Paar, T. Nikšić, D. Vretenar, P. Ring, Phys. Lett. **B 606** (2005) 288.

[8] N. Tsoneva, H. Lenske, Prog. Part. Nucl. Phys. **59** (2007) 317.

[9] S. Goriely, Phys. Lett. **B 460** (1998) 136.

[10] C. Wheldon, R. D'Alarcao, P. Chowdhury, P.M. Walker, E. Seabury, I. Ahmad, M.P. Carpenter, D.M. Cullen, G. Hackman, R.V.F. Janssens, T.L. Khoo, D. Nisius, C.J. Pearson, P. Reiter, Phys. Lett. **B 425** (1998) 239.

[11] K. Jain, O. Burglin, G.D. Dracoulis, B. Fabricius, N. Rowley, P.M. Walker, Nucl. Phys. **A 591** (1995) 61.

[12] I. Tanihata, H. Hamagaki, O. Hashimoto, Y. Shida, N. Yoshikawa, K. Sugimoto, O. Yamakawa, T. Kobayashi, N. Takahashi, Phys. Rev. Lett. **55** (1985) 2676.

[13] A. Ozawa, T. Suzuki, I. Tanihata, Nucl. Phys. **A 693** (2001) 32.

[14] ISOLDE Collaboration, E. Arnold, J. Bonn, A. Klein, R. Neugart, M. Neuroth, E.W. Otten, P. Lievens, H. Reich, W. Widdra, Phys. Lett. **B 281** (1992) 16.

[15] P.G. Hansen, B. Jonson, Europhys. Lett. **4** (1987) 409.

[16] L.-B. Wang, P. Müller, K. Bailey, G.W.F. Drake, J.P. Greene, D. Henderson, R.J. Holt, R.V.F. Janssens, C.L. Jiang, Z.-T. Lu, T.P. O'Connor, R.C. Pardo, K.E. Rehm, J.P. Schiffer, X.D. Tang, Phys. Rev. Lett. **93** (2004) 142501.

[17] P. Müller, I.A. Sulai, A.C.C. Vilalri, J.A. Alcántara-Núñez, R. Alves-Condé, K. Bailey, G.W.F. Drake, M. Dubois, C. Eléon, G. Gaubert, R.J. Holt, R.V.F.Janssens, N. Lecesne, Z.-T. Lu, T.P. O'Connor, M.-G. Saint-Laurent, J.-C. Thomas, L.-B. Wang, Phys. Rev. Lett. **99** (2007) 252501.

[18] R. Sánchez, W. Nörtherhäuser, G. Ewald, D. Albers, J. Behr, P. Bricault, B.A. Bushaw, A. Dax, J. Dilling, M. Dombsky, G.W.F. Drake, S. Götte, R. Kirchner, H.-J. Kluge, Th. Kühl, J. Lassen, C.D.P. Levy, M.R. Pearson, E.J. Prime, V. Ryjkov, A. Wojtaszek, Z.-C. Yan, C. Zimmermann, Phys. Rev. Lett. **96** (2006) 033002.

[19] M.V. Zhukov, B.V. Danilin, D.V. Fedorov, J.M. Bang, I.J. Thompson, J.S. Vaagen, Phys. Rep. **4** (1993) 151.

[20] M.V. Zhukov, I.J. Tompson, Phys. Rev. **C 52** (1995) 3505.

[21] L.V. Grigorenko, I.G. Mukha, M.V. Zhukov, Nucl. Phys. **A 713** (2003) 372.

[22] T. Baumann, A.M. Amthor, D. Bazin, B.A. Brown, C.M. Folden III, A. Gade, T.N. Ginter, M. Hausmann, M. Matoš, D.J. Morrissey, M. Portillo, A. Schiller, B.M. Sherrill, A. Stolz, O.B. Tarasov, M. Thoennessen, Nature **449** (2007) 1022.

[23] A.A. Korsheninnikov, M.S. Golovkov, I. Tanihata, A.M. Rodin, A.S. Fomichev, S.I. Sidorchuk, S.V. Stepantsov, M.L. Chelnokov, V.A. Gorshkov, D.D. Bogdanov, R. Wolski, G.M. Ter-Akopian, Yu.Ts. Oganessian, W. Mittig, P. Roussel-Chomaz, H. Savajols, E.A. Kuzmin, E.Yu. Nikolsky, A.A. Ogloblin, Phys. Rev. Lett. **87** (2001) 092501.

[24] M.S. Golovkov, Yu.Ts. Oganessian, D.D. Bogdanov, A.S. Fomichev, A.M. Rodin, S.I. Sidorchuk, R.S. Slepnev, S.V. Stepantsov, G.M. Ter-Akopian, R. Wolski, V.A. Gorshkov, M.L. Chelnokov, M.G. Itkis, E.M. Kozulin, A.A. Bogatchev, N.A. Kondratiev, I.V. Korzyukov, A.A. Yukhimchuk, V.V. Perevozchikov, Yu.I. Vinogradov, S.K. Grishechkin, A.M. Demin, S.V. Zlatoustovskiy, A.V. Kuryakin, S.V. Fil'chagin, R.I. Il'kaev, F. Hanappe, T.

Materna, L. Stuttge, A.H. Ninane, A.A. Korsheninnikov, E.Yu. Nikolskii, I. Tanihata, P. Roussel-Chomaz, W. Mittig, N. Alamanos, V. Lapoux, E.C. Pollacco, L. Nalpas, Phys. Lett. **B 566** (2003) 70.

[25] S.I. Sidorchuk, D.D. Bogdanov, A.S. Fomichev, M.S. Golovkov, Yu.Ts. Oganessian, A.M. Rodin, R.S. Slepnev, S.V. Stepantsov, G.M. Ter-Akopian, R. Wolski, V.A. Gorshkov, M.L. Chelnokov, M.G. Itkis, E.M. Kozulin, A.A. Bogatchev, N.A. Kondratiev, I.V. Korzyukov, A.A. Korsheninnikov, E.Yu. Nikolskii, I. Tanihata, Nucl. Phys. **A 719** (2003) 229c.

[26] M.G. Gornov, M.N. Ber, Yu.B. Gurov, S.V. Lapushkin, P.V. Morokhov, V.A. Pechkurov, N.O. Poroshin, V.G. Sandukovsky, M.V. Tel'kushev, B.A. Chernyshev, JETP Lett. **77** (2003) 344.

[27] M. Meister, L.V. Chulkov, H. Simon, T. Aumann, M.J.G. Borge, Th.W. Elze, H. Emling, H. Geissel, M. Hellström, B. Jonson, J.V. Kratz, R. Kulessa, K. Markenroth, G. Münzenberg, F. Nickel, T. Nilsson, G. Nyman, V. Pribora, A. Richter, K. Riisager, C. Scheidenberger, G. Schrieder, O. Tengblad, Nucl. Phys. **A 723** (2003) 13.

[28] M. Meister, L.V. Chulkov, H. Simon, T. Aumann, M.J.G. Borge, Th.W. Elze, H. Emling, H. Geissel, M. Hellström, B. Jonson, J.V. Kratz, R. Kulessa, K. Markenroth, G. Münzenberg, F. Nickel, T. Nilsson, G. Nyman, V. Pribora, A. Richter, K. Riisager, C. Scheidenberger, G. Schrieder, O. Tengblad, Phys. Rev. Lett. **91** (2003) 162504.

[29] M.S. Golovkov, L.V. Grigorenko, A.S. Fomichev, S.A. Krupko, Yu.Ts. Oganessian, A.M. Rodin, S.I. Sidorchuk, R.S. Slepnev, S.V. Stepantsov, G.M. Ter-Akopian, R. Wolski, M.G. Itkis, A.S. Denikin, A.A. Bogatchev, N.A. Kondratiev, E.M. Kozulin, A.A. Korsheninnikov, E.Yu. Nikolskii, P. Roussel-Chomaz, W. Mittig, R. Palit, V. Bouchat, V. Kinnard, T. Materna, F. Hanappe, O. Dorvaux, L. Stuttgé, C. Angulo, V. Lapoux, R. Raabe, L. Nalpas, A.A. Yukhimchuk, V.V. Perevozchikov, Yu.I. Vinogradov, S.K. Grishenkin, S.V. Zlatoustovskiy, Phys. Rev. **C 72** (2005) 064612.

[30] A.G. Sitenko, *Theory of Nuclear Reactions*, World Scientific Publishing Co., 1990.

[31] H. Geissel, G. Münzenberg, K. Riisager, Annu. Rev. Nucl. Part. Sci. **45** (1995) 163.

[32] T. Aumann, Eur. Phys. J. **A 26** (2005) 441.

[33] L.V. Chulkov, F. Aksouh, A. Bleile, O.V. Bochkarev, D. Cortina-Gil, A.V. Dobrovolsky, P. Egelhof, H. Geissel, M. Hellström, N.B. Isaev, O.A. Kiselev, B.G. Komkov, M. Matoš, F.N. Moroz, G. Münzenberg, M. Mutterer, V.A. Mylnikov, S.R. Neumaier, V.N. Pribora, D.M. Seliverstov, L.O. Sergeev, A. Shrivastava, K. Sümmerer, S.Yu. Torilov, H. Weick, M. Winkler, V.I. Yatsoura, Nucl. Phys. **A 759** (2005) 43.

[34] H. Geissel, P. Armbruster, K.H. Behr, A. Brünle, K. Burkard, M. Chen, H. Folger, B. Franczak, H. Keller, O. Klepper, B. Langenbeck, F. Nickel, E. Pfeng, M. Pfützner, E. Roeckl, K. Rykaczewski, I. Schall, D. Schardt, C. Scheidenberger, K.-H. Schmidt, A. Schröter, T. Schwab, K. Sümmerer, M. Weber, G. Münzenberg, T. Brohm, H.-G. Clerc, M. Fauerbach, J.-J. Gaimard, A. Grewe, E. Hanelt, B. Knödler, M. Steiner, B. Voss, J. Weckenmann, C. Ziegler, A. Magel, H. Wollnik, J.P. Dufour, Y. Fujita, D.J. Vieira, B. Sherrill, Nucl. Instrum. Meth. **B 70** (1992) 286.

[35] H. Stelzer, Nucl. Instrum. Meth. **A 310** (1991) 103.

[36] The ALADIN Collaboration, GSI Scientific Report, Darmstadt (1989) 292.

[37] LAND Collaboration, Th. Blaich, Th.W. Elze, H. Emling, H. Freiesleben, K. Grimm, W. Henning, R. Holzmann, G. Ickert, J.G. Keller, H. Klingler, W. Kneissl, R. König, R. Kulessa, J.V. Kratz, D. Lambrecht, J.S. Lange, Y. Leifels, E. Lubkiewicz, M. Proft, W. Prokopowicz, C. Schütter, R. Schmidt, H. Spies, K. Stelzer, J. Stroth, W. Walus, E. Wajda, H.J. Wollersheim, M. Zinser, E. Zude, Nucl. Instrum. Meth. **A 314** (1992) 136.

[38] ATIMA webpage, http://www-linux.gsi.de/~weick/atima/.

[39] H.T. Johansson, *The DAQ always runs*, Thesis for the degree of Licentiate of Engineering, Chalmers University of Technology, Göteborg, Sweden (2006).

[40] H.T. Johansson, Private communication.

[41] L. Heilbronn, Y. Iwata, H. Iwase, Nucl. Instrum. Meth. **A 522** (2004) 495.

[42] The R^3B Collaboration, Technical design report, Darmstadt (2005).

[43] M. Zinser, F. Humbert, T. Nilsson, W. Schwab, H. Simon, T. Aumann, M.J.G. Borge, L.V. Chulkov, J. Cub, Th.W. Elze, H. Emling, H. Geissel, D. Guillemaud-Mueller, P.G. Hansen, R. Holzmann, H. Irnich, B. Jonson, J.V. Kratz, R. Kulessa, Y. Leifels, H. Lenske, A. Magel, A.C. Mueller, G. Münzenberg, F. Nickel, G. Nyman, A. Richter, K. Riisager, C. Scheidenberger, G. Schrieder, K. Stelzer, J. Stroth, A. Surowiec, O. Tengblad, E. Wajda, E. Zude, Nucl. Phys. **A 619** (1997) 151.

[44] B.R. Martin, G. Shaw, *Particle physics*, John Wiley & Sons, Inc., West Sussex, England, 1997.

[45] L.M. Delves, Nucl. Phys. **9(59)** (1958) 391.

[46] L.M. Delves, Nucl. Phys. **20** (1960) 275.

[47] L.V. Chulkov, H. Simon, I.J. Thompson, T. Aumann, M.J.G. Borge, Th.W. Elze, H. Emling, H. Geissel, L.V. Grigorenko, M. Hellström, B. Jonson, J.W.V. Kratz, R. Kulessa, K. Markenroth, M. Meister, G. Münzenberg, F. Nickel, T. Nilsson, G. Nyman, V. Pribora, A. Richter, K. Riisager, C. Scheidenberger, G. Schrieder, O. Tengblad, M.V. Zhukov, Nucl. Phys. **A 759** (2005) 23.

[48] J. Raynal, J. Revai, Nuovo Cimento **A 68** (1970) 612.

[49] A.M. Lane, R.G. Thomas, Rev. Mod. Phys. **30** (1958) 257.

[50] E. Garrido, D.V. Fedorov, A.S. Jensen, K. Riisager, Phys. Rev. Lett. **86** (2001) 1986.

[51] G.F. Bertsch, K. Hencken, H. Esbensen, Phys. Rev. **C 57** (1998) 1366.

[52] K.M. Watson, Phys. Rev. **88** (1952) 1163.

[53] A.B. Migdal, Zh. Eksp. Teor. Fiz. **28** (1955) 3.

[54] J.M. Blatt, J.D. Jackson, Phys. Rev. **29** (1949) 18.

[55] K.W. McVoy, Nucl. Phys. **A 115** (1968) 481.

[56] W.R. Leo, *Techniques for Nuclear and Particle Physics Experiments*, Springer-Verlag, Berlin, Germany, 1987.

[57] LAND Collaboration, GSI Scientific Report, Darmstadt (1994) 275.

[58] R. Palit, P. Adrich, T. Aumann, K. Boretzky, B.V. Carlson, D. Cortina, U. Datta Pramanik, Th.W. Elze, H. Emling, H. Geissel, M. Hellström, K.L. Jones, J.V. Kratz, R. Kulessa, Y. Leifels, A. Leistenschneider, G. Münzenberg, C. Nociforo, P. Reiter, H. Simon, K. Sümmerer, W. Walus, Phys. Rev. **C 68** (2003) 034318.

[59] K.H. Wilcox, R.B. Weisenmiller, G.J. Wozniak, N.A. Jelley, D. Ashery, J. Cernyet, Phys. Lett. **B 59** (1975) 142.

[60] F.C. Barker, G.T. Hickey, J. Phys. G: Nucl. Phys. **3** (1977) L23.

[61] A.I. Amelin, M.G. Gornov, Yu.B. Gurov, A.L. Ilin, P.V. Morokhov, V.A. Pechkurov, V.I. Savelev, F.M. Sergeev, S.A. Smirnov, B.A. Chernyshev, R.R. Shafigullin, A.V. Shishkovet, Yad. Fiz. **52** (1990) 1231.

[62] H.G. Bohlen, W. von Oertzen, Th. Stolla, R. Kalpakchieva, B. Gebauer, M. Wilpert, Th. Wilpert, A.N. Ostrowski, S.M. Grimes, T.N. Masseyet, Nucl. Phys. **A 616** (1997) 254.

[63] R.A. Kryger, A. Azhari, A. Galonsky, J.H. Kelley, R. Pfaff, E. Ramakrishnan, D. Sackett, B.M. Sherill, M. Thoennessen, J.A. Winger, S. Yokoyama, Phys. Rev. **C 47** (1993) R2439.

[64] M. Thoennessen, S. Yokoyama, A. Azhari, T. Baumann, J.A. Brown, A. Galonsky, P.G. Hansen, J.H. Kelley, R.A. Kryger, E. Ramakrishnan, P. Thirolf, Phys. Rev. **C 59** (1999) 111.

[65] M. Chartier, J.R. Beeneb, B. Blank, L. Chen, A. Galonsky, N. Gan, K. Govaert, P.G. Hansen, J. Kruse, V. Maddalena, M. Thoennessen, R.L. Varner, Phys. Rev. **B 510** (2001) 24.

[66] M. Zinser, F. Humbert, T. Nilsson, W. Schwab, Th. Blaich, M.J.G. Borge, L.V. Chulkov, Th.W. Elze, H. Emling, H. Freisleben, H. Geissel, K. Grimm, D. Guillemaud-Mueller, P.G. Hansen, R. Holzmann, H. Irnich, B. Jonson, J.G. Keller, H. Klinger, J.V. Kratz, R. Kulessa, D. Lambrecht, Y. Leifels, A. Magel, M. Mohar, A.C. Mueller, G. Münzenberg, F. Nickel, G. Nyman, A. Richter, K. Riisager, C. Scheidenberger, G. Schrieder, B.M. Sherill, H. Simon, K. Stelzer, J. Stroth, O. Tengblad, W. Trautmann, E. Wajda, E. Zude, Phys. Rev. Lett. **75** (1995) 1719.

[67] C. Bachelet, G. Audi, C. Gaulard, C. Guénaut, F. Herfurth, D. Lunney, M. De Saint Simon, C. Thibault, Phys. Rev. Lett. **100** (2008) 182501.

[68] H. Simon, M. Meister, T. Aumann, M.J.G. Borge, L.V. Chulkov, U. Datta Pramanik, Th.W. Elze, H. Emling, C. Forssén, H. Geissel, M. Hellström, B. Jonson, J.V. Kratz, R. Kulessa, Y. Leifels, K. Markenroth, G. Münzenberg, F. Nickel, T. Nilsson, G. Nyman, A. Richter, K. Riisager, C. Scheidenberger, G. Schrieder, O. Tengblad, M.V. Zhukov, Nucl. Phys. **A 791** (2007) 267.

[69] H.B. Jeppesen, A.M. Moro, U.C. Bergmann, M.J.G. Borge, J. Cederkäll, L.M. Fraile, H.O.U. Fynbo, J. Gómez-Camacho, H.T. Johansson, B. Jonson, M. Meister, T. Nilsson, G. Nyman, M. Pantea, K. Riisager, A. Richter, G. Schrieder, T. Sieber, O. Tengblad, E. Tengborn, M. Turrión, F. Wenander, Phys. Lett. **B 642** (2006) 449.

[70] H.G. Bohlen, A. Blazevic, B. Gebauer, W. von Oertzen, S. Thummerer, R. Kalpakchieva, S.M. Grimes, T.N. Massey, Prog. Part. Nucl. Phys. **42** (1999) 17.

[71] J.D. Bowman, A.M. Poskanzer, R.G. Korteling, G.W. Butler, Phys. Rev. **C 9** (1974) 836.

[72] G. Audi, A.H. Wapstra, C. Thibault, Nucl. Phys. **A 729** (2003) 337.

[73] Yu. Aksyutina, H.T. Johansson, P. Adrich, F. Aksouh, T. Aumann, K. Boretzky, M.J.G. Borge, A. Chatillon, L.V. Chulkov, D. Cortina-Gil, U. Datta Pramanik, H. Emling, C. Forssén, H.O.U. Fynbo, H. Geissel, M. Hellström, G. Ickert, K.L. Jones, B. Jonson, A. Kliemkiewicz, J.V. Kratz, R. Kulessa, M. Lantz, T. LeBleis, A.O. Lindahl, K. Mahata, M. Matos, M. Meister, G. Münzenberg, T. Nilsson, G. Nyman, R. Palit, M. Pantea, S. Paschalis, W. Prokopowicz, R. Reifarth, A. Richter, K. Riisager, G. Schrieder, H. Simon, K. Sümmerer, O. Tengblad, W. Walus, H. Weick, M.V. Zhukov, Phys. Lett. **B 666** (2008) 430.

[74] N.A.F.M Poppelier, L.D. Wood, P.W.M. Glaudemans, Phys. Lett. **B 157** (1985) 120.

[75] C. Forssén, B. Jonson, M.V. Zhukov, Nucl. Phys. **A 673** (2000) 143.

[76] A.A. Korsheninnikov, K. Yoshida, D.V. Aleksandrov, N. Aoi, Y. Doki, N. Inabe, M. Fujimaki, T. Kobayashi, H. Kumagai, C.-B. Moon, E.Yu. Nikolskii, M.M. Obuti, A.A. Ogloblin, A. Ozawa, S. Shimoura, T. Suzuki, I. Tanihata, Y. Watanabe, M. Yanokura, Phys. Lett. **B 326** (1994) 31.

[77] K. Hagino, N. Takahashi, H. Sagawa, Phys. Rev. **C 77** (2008) 054317.

[78] L.V. Chulkov, G. Schrieder, Z. Phys. **A 359** (1997) 231.

[79] N. Keeley, F. Skaza, V. Lapoux, N. Alamanos, F. Auger, D. Beaumel, E. Becheva, Y. Blumenfeld, F. Delaunay, A. Drounart, A. Gillibert, L. Giot, K.W. Kemper, L. Nalpas, A. Pakou, E.C. Pollacco, R. Raabe, P. Roussel-Chomaz, K. Rusek, J.-A. Scarpaci, J.-L. Sida, S. Stepantsov, R. Wolski, Phys. Lett. **B 646** (2007) 222.

[80] K.K. Seth, Nucl. Phys. **A 434** (1985) 287.

[81] K.K. Seth, M. Artuso, D. Barlow, S. Iversen, M. Kaletka, H. Nann, B. Parker, R. Soundranayagam, Phys. Rev. Lett. **58** (1987) 1930.

[82] A.V. Belozerov, K. Borsha, Z. Dlougy, A.M. Kalinin, Nguyen Hoai Thiau, Yu.E. Penionzhkevich, Izv. Akad. Nauk. SSSR, Ser. Fiz. **52** (1988) 100.

[83] H.G. Bohlen, B. Gebauer, D. Kolbert, W. von Oertzen, E. Stilaris, M. Wilpert, T. Wilpert, Z. Phys. **A 330** (1988) 227.

[84] L. Chen, B. Blank, B.A. Brown, M. Chartier, A. Galonsky, P.G. Hansen, M. Thoennessen, Phys. Lett. **B 505** (2001) 21.

[85] M.S. Golovkov, L.V. Grigorenko, A.S. Fomichev, A.V. Gorshkov, V.A. Gorshkov, S.A. Krupko, Yu.Ts. Oganessian, A.M. Rodin, S.I. Sidorchuk, R.S. Slepnev, S.V. Stepantsov, G.M. Ter-Akopian, R. Wolski, A.A. Korsheninnikov, E.Yu. Nikolskii, V.A. Kuzmin, B.G. Novatskii, D.N. Stepanov, P. Roussel-Chomaz, W. Mittig, Phys. Rev. **C 76** (2007) 021605.

[86] M.H. Al Falou, Thesis, Université de Caen, LPCC T 07-03 (2007).

[87] B. Jonson, Phys. Rep. **389** (2004) 1.

[88] A.M. Poskanzer, S.W. Cosper, E.K. Hyde, J. Cerny, Phys. Rev. Lett. **17** (1966) 1271.

[89] A.N. Ostrowski, H.G. Bohlen, B. Gebauer, S.M. Grimes, R. Kalpakchieva, Th. Kirchner, T.N. Massey, W. von Oerzten, Th. Stolla, M. Wilpert, Th. Wilpert, Phys. Lett. **B 338** (1994) 13.

[90] T. Kobayashi, K. Yoshida, A. Ozawa, I. Tanihata, A. Korsheninnikov, E. Nikolsky, T. Nakamura, Nucl. Phys. **A 616** (1997) 223c.

[91] M.V. Zhukov, Private communication.

[92] S. Aoyama, Phys. Rev. Lett. **89** (2002) 052501.

[93] L.V. Grigorenko, M.V. Zhukov, Phys. Rev. **C 77** (2008) 034611.

[94] M.S. Golovkov, L.V. Grigorenko, G.M. Ter-Akopian, A.S. Fomichev, Yu.Ts. Oganessian, V.A. Gorshkov, S.A. Krupko, A.M. Rodin, S.I. Sidorchuk, R.S. Slepnev, S.V. Stepantsov, R. Wolski, D.Y. Pang, V. Chudoba, A.A. Korsheninnikov, V.A. Kuzmin, E.Yu. Nikolskii, B.G. Novatskii, D.N. Stepanov, P. Roussel-Chomaz, W. Mittig, A. Ninane, F. Hanappe, L. Stuttgé, A.A. Yukhimchuk, V.V. Perevozchikov, Yu.I. Vinogradov, S.K. Grishechkin, S.V. Zlatoustovskiy, Phys. Lett. **B 672** (2009) 22.

[95] N.V. Shulgina, B. Jonson, M.V. Zhukov, Nucl. Phys. **A 825** (2009) 175.

Acknowledgements

At this place I would like to thank all people who have helped me to perform this work in many various ways and who supported me while writing the thesis.

In the first place I would like to thank my supervisor at the Frankfurt university, Joachim Stroth, for giving me the great opportunity to perform this work. A great thanks to Rene Reifarth for his help with administrative procedures at Frankfurt university, for reading the thesis and for valuable comments.

I would like to sincerely thank my supervisor at GSI, Haik Simon, for guiding me through analysis process from the very first steps, always having answers to all questions and a solution of any problem. Furthermore, I would like to thank for numerous physics discussions and his countenance in difficult moments.

I address my heartful gratitude to Leonid Chulkov for his invaluable help with analysis and interpretation of the data. In addition, I would like to admit his readiness to answer any question and numerous discussions during the realization of the thesis. This work could not be performed without his help.

I would like to thank the head of the LAND group Tom Aumann for giving me the great opportunity to be a group member and to perform this work.

I am very grateful to Håkan Johansson for his infinite enthusiasm and work capacity. Without the analysis software provided by him, this work would be much more complicated. Apart from that, his every day help and support were very important for me.

I address my heartful gratitude to Björn Jonson for his belief in me and for his unflagging optimism. Furthermore, I am very grateful for organizing the financial support of my visits to Chalmers university.

I would also like to thank Achim Richter for continuous interest in results of my work.

I am greatful to all the past and present members of LAND group for creating a good atmosphere and for making it a real pleasure to work with them. In particular, I acknowledge Kripamay Mahata, Stephanos Paschalis, Dominic Rossi, Tudi Le Bleis and Adam Klimkiewicz for useful discussions about physics, analysis, programming and many other interesting topics. I am very thankful to Konstanze Boretzky, Audrey Chatillon and Christine Wimmer for their readiness to help and for organizing unforgettable leisure. I want to express my thanks to

all people who was reading this thesis for their important comments.

Also, I would like to thank people from Chalmers university Thomas Nilsson, Mikhail Zhukov, Göran Nyman, Elizabeth Tengborn, Mattias Lantz and Kate Larsson for creating a good working environment during my visits.

Finally, my heartful gratitude to my family. I am very thankful to my parents Volodymyr and Nelli and sister Irina for their support and encouraging me day by day. I really appreciate the understanding and infinite patience of my husband Maksym.

Curriculum Vitæ

Yuliya Aksyutina
Bornstraße 55
64291 Darmstadt

16.03.1983	was born in Kharinovo, Russia
1989 – 1998	Secondary school, Prystin, Kharkiv region, Ukraine
1998 – 2000	Gymnasium Nr. 1, Kupyansk, Kharkiv region, Ukraine
09.2000	beginning of education at the Department of Physics & Technology, V.N. Karazin Kharkiv National University
12.2003 – 06.2004	work in collaboration with Gesellschaft für Schwerionenforschung. Practical experience in the project: "Neutron Detection Scheme for Correlation Experiments with Neutron Halo Nuclei"
06.2004	graduated as Bachelor with a diploma of excellent degree. Specialization of applied physics
05.2005 – 02.2006	work in collaboration with Gesellschaft für Schwerionenforschung. Practical experience in the project: "Experimental studies with energetic beams of ^{14}Be, ^{11}Li and ^{8}He"
02.2006	graduated as Master with a diploma of excellent degree. Specialization of experimental nuclear physics
since 22.05.2006	PhD student at the LAND group and the Institute of Nuclear Physics of Johann Wolfgang Goethe-Universität, Frankfurt